



LUND UNIVERSITY

Highly Dynamic Drives for Electric Hybrid Vehicles

Electric Machine Design and Dynamic Test Method

Loayza Vargas, Yury

2017

Document Version:

Publisher's PDF, also known as Version of record

[Link to publication](#)

Citation for published version (APA):

Loayza Vargas, Y. (2017). *Highly Dynamic Drives for Electric Hybrid Vehicles: Electric Machine Design and Dynamic Test Method* (1 ed.). [Doctoral Thesis (monograph), Division for Industrial Electrical Engineering and Automation]. Division of Industrial Electrical Engineering and Automation, Faculty of Engineering, Lund University.

Total number of authors:

1

General rights

Unless other specific re-use rights are stated the following general rights apply:

Copyright and moral rights for the publications made accessible in the public portal are retained by the authors and/or other copyright owners and it is a condition of accessing publications that users recognise and abide by the legal requirements associated with these rights.

- Users may download and print one copy of any publication from the public portal for the purpose of private study or research.
- You may not further distribute the material or use it for any profit-making activity or commercial gain
- You may freely distribute the URL identifying the publication in the public portal

Read more about Creative commons licenses: <https://creativecommons.org/licenses/>

Take down policy

If you believe that this document breaches copyright please contact us providing details, and we will remove access to the work immediately and investigate your claim.

LUND UNIVERSITY

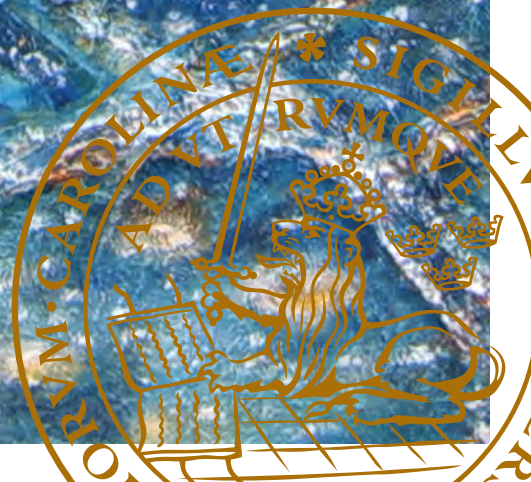
PO Box 117
221 00 Lund
+46 46-222 00 00



Highly Dynamic Drives for Electric Hybrid Vehicles

Electric Machine Design and Dynamic Test Method

YURY ALCIDES LOAYZA VARGAS | FACULTY OF ENGINEERING (LTH) | LUND UNIVERSITY
THESIS FOR THE DEGREE OF DOCTOR OF PHILOSOPHY IN ENGINEERING





Yury Loayza, born in Cusco, Peru, has a degree of Master of Science in Mechanical Engineering from the Faculty of Engineering of Lund University (LTH) in Sweden. He carried out part of his undergraduate studies in Stuttgart, Germany and also in Boulder, Colorado, USA.

Yury Loayza carried out his PhD Studies at the at the Division of Industrial Electrical Engineering and Automation (IEA) at LTH, focusing on Electric Hybrid Vehicles.



Highly Dynamic Drives for Electric Hybrid Vehicles

Highly Dynamic Drives for Electric Hybrid Vehicles

Electric Machine Design and Dynamic Test Method

by Yury Alcides LOAYZA VARGAS



LUND
UNIVERSITY

Thesis for the degree of Doctor of Philosophy in Engineering
Thesis supervisors: Prof. Mats Alaküla, Assoc. Prof. Avo Reinap
Faculty opponent: Dr. Pia Lindh

To be presented, with the permission of the Faculty of Engineering of Lund University, for public criticism in the M:B lecture hall, Mechanical Engineering Building, Ole Römers väg 1, Lund, Sweden, on Friday, the 20th of October 2017 at 10:15 a.m.

| | | | |
|--|--|--|-------|
| Organization LUND UNIVERSITY Department of BME Division of Industrial Electrical Engineering and Automation (IEA) | | Document name DOCTORAL DISSERTATION | |
| | | Date of disputation 2017-10-20 | |
| | | Sponsoring organization Vinnova, Innovatum, The Swedish Energy Agency, Lund University | |
| Author(s) Yury Alcides LOAYZA VARGAS | | | |
| Title and subtitle Highly Dynamic Drives for Electric Hybrid Vehicles Electric Machine Design and Dynamic Test Method | | | |
| Abstract <p><i>Electric Hybrid Vehicles (EHVs)</i> play a crucial role in the development towards a more environmental friendly transportation. An alternative to solve some actual challenges with hybridization of vehicles is studied at the <i>Division of Industrial Electrical Engineering and Automation (IEA)</i> at Lund University in cooperation with the automotive industry. A key component of this drive train is a highly dynamic <i>Electric Machine (EM)</i> which will make possible to hybridize a conventional car at reduced costs while maintaining the performance and comfort of the vehicle.</p> <p>The first part of this thesis work describes the design and optimization process of this multipurpose <i>EM</i> and presents the final prototype.</p> <p>The second part of this thesis presents a convenient, fast and precise method for measuring the mechanical and electromagnetic properties of this <i>EM</i> and similar motors. This <i>Dynamic Test Method</i> is based on state of the art control and measurements system and makes possible to characterize an <i>EM</i> without the need of a <i>Brake Bench</i>.</p> <p>Finally the measured properties of the <i>EM</i> are analyzed and the results show that the <i>EM</i> has the required performace in speed, torque and dynamics for the intended <i>EHV</i> application.</p> <p>The results of the thesis reduce the need of heavy and expensive components for the <i>EHV</i> and for the measurements, by using very fast, dynamic and accurate tools instead.</p> | | | |
| Key words Electric Hybrid Vehicles, Electric Machine Design, Dynamic Testing, Dynamic loading, Synthetic Loading, FPGA, Torque Measurement, Field Weakening, iPMSM, FEMM, LabView | | | |
| Classification system and/or index terms (if any) | | | |
| Supplementary bibliographical information | | Language English | |
| ISSN and key title | | ISBN 978-91-88934-83-3 (print) 978-91-88934-82-6 (pdf) | |
| Recipient's notes | | Number of pages 210 | Price |
| | | Security classification | |

I, the undersigned, being the copyright owner of the abstract of the above-mentioned dissertation, hereby grant to all reference sources the permission to publish and disseminate the abstract of the above-mentioned dissertation.

Signature _____

Date 2017-08-29 _____

Highly Dynamic Drives for Electric Hybrid Vehicles

Electric Machine Design and Dynamic Test Method

by Yury Alcides LOAYZA VARGAS



LUND
UNIVERSITY

Cover illustration front:

Oil painting, by the author's sister Karina Loayza Vargas, of the ancient salt evaporation ponds in Maras, Cusco, Peru.

Cover illustration back:

Author's portrait.

© Yury Alcides LOAYZA VARGAS, 2017

yury.loayza@iea.lth.se

Faculty of Engineering (LTH) at Lund University
Department of BME
Division of Industrial Electrical Engineering and Automation (IEA)

ISBN: 978-91-88934-83-3 (print)

ISBN: 978-91-88934-82-6 (pdf)

CODEN: LUTEDX/(TEIE-1084)/1-210/(2017)

Printed in Sweden by Media-Tryck, Lund University, Lund 2017



I shall be telling this with a sigh
Somewhere ages and ages hence:
Two roads diverged in a wood, and I—
I took the one less traveled by,
And that has made all the difference.

- Robert Frost

Dedicated to my son Vincent

Contents

| | |
|---|--------------|
| Abstract | xiii |
| Acknowledgements | xv |
| Popular science summary | xvii |
| Publications and author's contributions to the papers | xxiii |
| Glossary | xxvii |
| 1 Introduction | 1 |
| 1.1 Motivation for the development of electric drives for vehicles . . . | 1 |
| 1.2 Arrangement of the thesis | 3 |
| 1.3 Contributions | 4 |
| 2 Cost effective topology for an electric hybrid vehicle | 7 |
| 2.1 The cost effective hybrid topology | 7 |
| 2.2 Specifications of the electric drive | 13 |
| 3 Design of the electric machine | 17 |
| 3.1 Specifications of the electric machine | 17 |
| 3.2 Fast optimization of the internal parameters of the electric machine | 22 |
| 3.3 Post processing of the results from the <i>finite element analysis</i> . | 27 |
| 3.4 Strategy to reduce the number of simulations and the whole op- timization time | 38 |
| 3.5 Finite Element Analysis of the final geometry | 40 |
| 3.6 Different rotor configurations to reduce cogging | 49 |
| 3.7 Thermal analysis of the final design | 53 |
| 3.8 Final design and prototype properties | 58 |
| 3.9 The prototype | 60 |
| 4 Description of the <i>Dynamic Test Method</i> | 65 |
| 4.1 Information needed from the measurements | 65 |
| 4.2 Reasons for why measurements are required | 66 |
| 4.3 Challenges | 66 |
| 4.4 Testing Methods | 67 |

| | | |
|----------|---|------------|
| 4.5 | Characteristics of this dynamic test method respect to other acceleration methods | 71 |
| 4.6 | Other methods without brake bench | 71 |
| 4.7 | Background | 72 |
| 4.8 | Implications of the <i>Dynamic Test Method</i> | 74 |
| 5 | Measurements and calculations with the <i>Dynamic Test Method</i> | 75 |
| 5.1 | Methodology and experimental setup | 75 |
| 5.2 | Measurement and calculations | 76 |
| 5.3 | Validation | 104 |
| 6 | Torque and speed control and machine properties | 113 |
| 6.1 | Calculation of the look-up-tables for field weakening | 114 |
| 6.2 | Properties of the electric machine: power, losses, efficiency | 123 |
| 6.3 | Gear shift synchronization | 126 |
| 7 | Conclusions and suggestions for future work | 135 |
| 7.1 | Conclusions | 135 |
| 7.2 | Suggestions for Future Work | 136 |
| A | Experimental setup | 137 |
| 1.1 | The equipment | 137 |
| 1.2 | The hardware | 140 |
| 1.3 | The software | 142 |
| B | Data | 145 |
| 2.1 | Data from finite element analysis | 145 |
| 2.2 | Data from the dynamic test method | 146 |
| 2.3 | Field Weakening look-up-tables | 148 |
| 2.4 | Curve fitting of the oscillations to determine the cogging torque . | 150 |
| C | Drawings of the electric machine | 153 |
| D | Data sheets | 163 |
| 4.1 | Bibliography | 175 |

Abstract

Electric Hybrid Vehicles (EHVs) play a crucial role in the development towards a more environmental friendly transportation. An alternative to solve some actual challenges with hybridization of vehicles is studied at the *Division of Industrial Electrical Engineering and Automation (IEA)* at Lund University in cooperation with the automotive industry. A key component of this drive train is a highly dynamic *Electric Machine (EM)* which will make possible to hybridize a conventional car at reduced costs while maintaining the performance and comfort of the vehicle.

The first part of this thesis work describes the design and optimization process of this multipurpose *EM* and presents the final prototype.

The second part of this thesis presents a convenient, fast and precise method for measuring the mechanical and electromagnetic properties of this *EM* and similar motors. This *Dynamic Test Method* is based on state of the art control and measurements system and makes possible to characterize an *EM* without the need of a *Brake Bench*.

Finally the measured properties of the *EM* are analyzed and the results show that the *EM* has the required performance in speed, torque and dynamics for the intended *EHV* application.

The results of the thesis reduce the need of heavy and expensive components for the *EHV* and for the measurements, by using very fast, dynamic and accurate tools instead.

Acknowledgements

I would like to express my thanks and appreciation:

to my advisor Mats Alaküla and my co-advisor Avo Reinap, for their support, all the knowledge I learned from them and for their wise advice,

to all my colleges at the *Division of Industrial Electrical Engineering and Automation (IEA)* at Lund University: Anita Borné, Carina Lindström, Eva Everitt, Henriette Weibull, Ulrika Westerdahl, Ulf Jeppsson, Mats Alaküla, Avo Reinap, Getachew Darge, Bengt Simonsson, Gunnar Lindstedt, Olof Samuelsson, Jörgen Svensson, Carlos Martins, and all the other friends whose time at *IEA* as Lic., PhD students, or other research activities overlapped with mine: for the good cooperation, help, support, interesting conversations, funny activities outside work, exciting trips, and for the friendly, optimistic, positive, and flexible atmosphere at the division. Exactly the kind of atmosphere that is optimal in research and innovation for allowing new innovative ideas to grow,

to Ulf Jeppsson at the head of *IEA* making possible that this project developed in a good way,

to my colleges Getachew Darge, Bengt Simonsson, Gunnar Lindstedt, Johan Björnstedt, Pelle Steen, who directly contributed to this research project with their knowledge, experience and cooperation,

to my family, home in Perú, who always welcome me and my son with their warmth every time we come home, to my dad Alcides, my second mom Luz, my sister Karina, my brothers Alfredo and Neto, who always inspire me with the passion they put on their work and the way they see life,

to *Innovatum, Vinnova, The Swedish Energy Agency, Saab Automobile, Vacuumschmelze, Bevi, Binar, Research Institutes of Sweden (RISE), Volvo Trucks, The European Spallation Source (ESS), LU Innovation, LU Holding*, for their financial and material support and their cooperation,

Yury

Lund and Malmö, 2017

Popular science summary

In the recent years, there has been huge investment in the automotive industry in the field of electric transportation, to reduce the consumption of fossil fuels. The *Division of Industrial Electrical Engineering and Automation (IEA)* at Lund University is a very important actor in Sweden in this process. *IEA* carries on many research projects in the field of electric transportation in cooperation with the industry.

By doing my research work for my PhD at *IEA*, I have been able to take part in the technological events happening in these times where many people around the world are working towards cleaner and more environmentally friendly transportation.

In this aim, the main contributions of the thesis are:

- A very customized electric motor, designed for cost effective hybridization of cars
- The *Dynamic Test Method*: A convenient, fast and precise method to measure the internal properties of electric motors, that reduce the need of expensive equipment and saves time during the development of electric drives for cars.

These results are useful, for example:

- for car companies, to make a low cost hybrid in the proposed way
- for researchers and developers of new electric machines who can make use of the presented methods and results
- to provide information about newly developed electric motors in a convenient, easier and faster way using *Dynamic Test Method*. This will facilitate and improve the development of new electric motors and the use of them in cars.

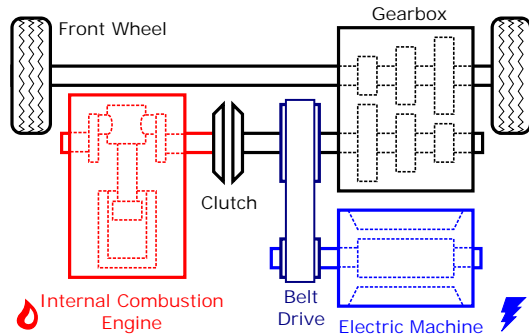
Together with other developments towards electro mobility, the results of this research will help in the process of reducing the need and the use of fossil fuels, which will have a positive effect on the environment and health.

Brief description of my work:

When I started my research work at *IEA*, my main task was to design a special electric motor for a cost effective hybrid car topology. The philosophy behind, is that, in order to make a more significant impact on the environment, it is important to hybridize the most common car models instead on focusing on exclusive cars which are sold in fewer numbers.

This topology reuses the conventional drive train, especially the manual gearbox which is more compact, has lower price, and is more efficient than other types of gearboxes used in hybrids.

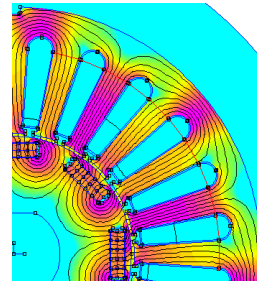
Figure 1: Topology of the hybrid drive train



The electric motor here should not only be powerful enough for vehicle traction but it should also synchronize the shafts in the gear box during gearshift. Accordingly, it should be able to change from one certain speed to another in a fraction of a second, so that the gearshift is unnoticed by the driver.

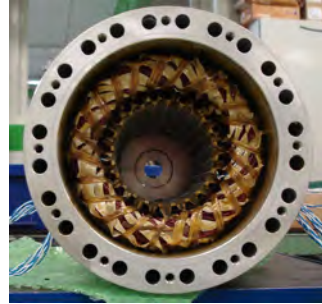
I designed and optimized the electric motor using the tools developed at *IEA*, the optimization was made basically by using *Finite Element Analysis (FEA)* and focused on low rotor inertia while retaining the requirements for power, torque and speed for vehicle traction.

Figure 2: Numerical simulation for the electric motor design



After the design process was ready, a prototype was manufactured by a motor factory.

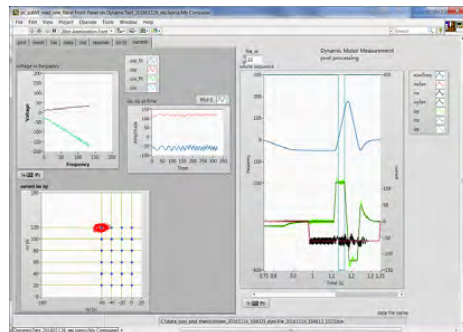
Figure 3: Manufacturing of the electric motor



Then the prototype needed to be tested to ensure that it has the expected properties and performance. Testing this new motor implied some challenges, considering that the motor was quite extreme in terms of speed and accelerations.

For this reason, we upgraded the control system to a new one based on *Field Programmable Gate Array (FPGA)* technology. *FPGA* is a programmable integrated circuit that is incredibly fast at performing several pre defined calculations simultaneously. Thus it is ideal for controlling the magnetic field in this dynamic motor, for example. My next task was to develop the software for the *FPGA* for motor control. Programming a *FPGA* is more complicated and time consuming than programming a microprocessor. But once the *FPGA* is programmed, it works very fast and with high accuracy and reliability.

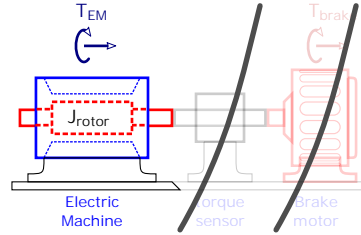
Figure 4: A state of the art control and measurement system is developed for this dynamic electric motor



Another challenge for testing the new motor was to install it on the braking test bench, it was very difficult and time consuming to align and calibrate all the other components, and any limitation on torque or speed in one of them would set a limit to the whole test.

Instead of installing the motor on the test bench, I decided to further develop the control system so that the motor could be tested without the need of an external load.

Figure 5: The Dynamic Test Method reduces the need of expensive equipment and make the measurement more precise



Pulses of current were applied to the motor and it would accelerate freely. Considering the high torque levels used in a car applications and the low inertia of this motor, it took only fractions of a second to reach maximum permissible speed. This is where the advantages of the *FPGA* are put to good use. It could handle these extremely high accelerations. Large amounts of data were collected with high time resolution during the acceleration, and streamed to the computer for later analysis. Different methods were developed to extract the required motor information. In this way the electric machine could be tested with high accuracy, without disturbance of other external components, with low temperature rise due to the short test time, etc. This test method, named as the *Dynamic Test Method* is described in detail in this thesis with its advantages and properties.

Figure 6: The required information from the electric motor is obtained. For example, the torque map is displayed as a function of the direction and intensity of the magnetic fields created inside the motor

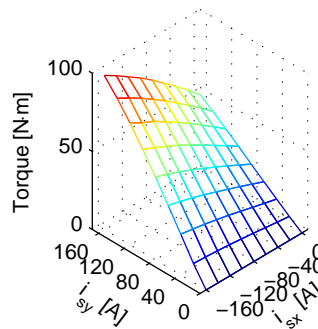


Figure 7: Other example of required data is the torque ripple, which is calculated by decomposing the oscillations during rotation.

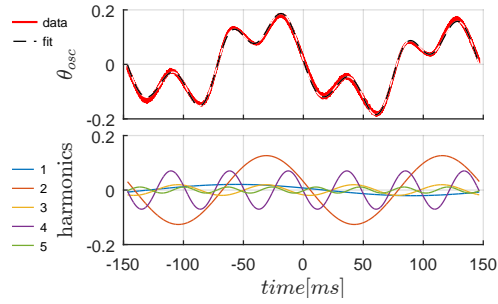
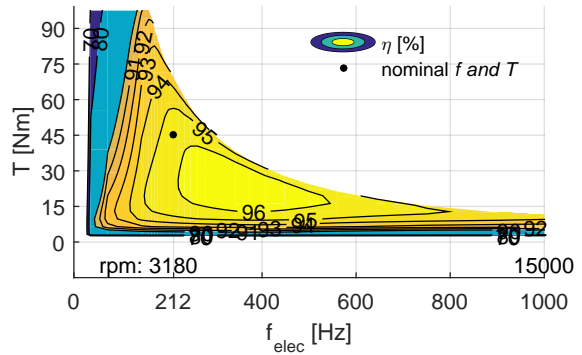


Figure 8: The efficiency map of the motor, standard information required in the industry for optimal use and integration of the motor, is also calculated from the measurements



Finally, with the data obtained from the electric motor, it is shown that

- The *Dynamic Test Method* is a useful and convenient method for characterizing an electric motor

and that this motor complies with the specifications for the hybrid car application, which are mainly:

- vehicle traction in electric mode when possible, for example in city traffic
- helping to improve fuel efficiency by helping the gasoline engine to work under optimal loading
- and due to its high dynamics, allows continued use of a compact, low price and efficient manual gearbox

Publications and author's contributions to the papers

This thesis is written as a monograph and as such all the ideas are expressed in the main chapters of this book independently of other publications by the author of this thesis *Yury Loayza* (*YL*). A list is included of the articles published during this research project where *YL* is either the main author or a contributing author. The first two papers listed here are strong related to the contents of this thesis, about motor design and the *Dynamic Test Method*, the other three are about subjects, such as *Direct Current Control (DCC)* and thermal measurements that are outside the scope of thesis.

- Avo Reinap , Dan Hagstedt , Francisco Marquez , Yury Loayza , Mats Alaküla. ***Development of a radial flux machine design environment***. In Electrical Machines, 2008. ICEM 2008. 18th International Conference on, pages 1-4, Sept 2008, Villamoura, Portugal. doi: 10.1109/ICELMACH.2008.4800195. [1]

YL uses and tests the software *RF-Design* for motor design making necessary adaptations the to the specific requirements of his motor. *YL* tests different semi automated optimization methods and makes his own post processing calculations.

- Yury Loayza , Avo Reinap and Mats Alaküla. **Performance and efficiency evaluation of fpga controlled ipmsm under dynamic loading**. In 8th IEEE Symposium on Diagnostics for Electrical Machines, Power Electronics Drives, pages 550-555, Sept 2011. doi: 10.1109/DEMPED.2011.6063677 [2]

YL comes up with the idea and develops the *Dynamic Test Method* which is described in this paper. *YL* writes the paper as main author with the support of his advisors who are the two other authors. *YL* presents the method at the conference in Bologna.

- Sebastian Hall and Yury Loayza. **An evaluation of two direct current control methods implemented with labview on an fpga.** In the 2013 International Conference on Electrical Machines and Systems (ICEMS), pages 1455-1460, Oct 2013. doi: 10.1109/ ICEMS.2013.6713122. [3]

With the experience of supervising a previous study on *DCC* [4], *YL* suggests potential advantages of implementing the *DCC* in stator coordinate system instead of rotor coordinate system. Using the rotor coordinate system is the standard method described in the text book [5]. *YL*'s previous implementation of motor control using *PI-control* is used as a starting point for this implementation. *SH* implements the method, makes the experimental tests, writes the paper and presents it at the conference.

- Sebastian Hall, Yury Loayza, Avo Reinap, and Mats Alaküla. **Consistency analysis of torque measurements performed on a pmsm using dynamic testing.** In 2014 International Conference on Electrical Machines (ICEM), pages 1529-1535, Sept 2014. doi: 10.1109/ ICELMACH.2014.6960385. [6]

YL contributes with the *Dynamic Test Method*, an example of the code for motor control, the control unit and support. *SH* develops his own control and makes extensive tests to evaluate the consistency of the *Dynamic Test Method*. *SH* writes the paper and presents it at the conference in Berlin. The work is done with the supervision and support of the other 2 authors.

- Zhe Huang , F. J. Márquez-Fernández , Yury Loayza , Avo Reinap and Mats Alaküla. **Dynamic thermal modelling and application of electrical machine in hybrid drives.** In the 2014 International Conference on Electrical Machines (ICEM), pages 2158-2164, Sept 2014. doi: 10.1109/ICELMACH.2014.6960483. [7]

The main part of the work is done by *ZH*, the other authors help her with their expertise in different areas, *YL* helps *ZH* to make the experimental measurements. *YL* provides the hardware and software for motor control

and measurements. *YL* suggest methods for heating up the motor for thermal measurements without the need of a brake motor. The methods mainly consist of:

- using demagnetization current at constant low speed to generate resistive heat in the copper windings
- running the motor at high speed in idling mode to generate heat in the iron core

Glossary

- P_{nom} Nominal power of the EM. In this thesis 15[kW]. 9, 14, 20, 36, 44, 59, 60, 123, 129
- T_{nom} Nominal torque of the EM. In this thesis 45[Nm]. The torque that the EM can deliver continuously without overheating. 20, 28, 29, 36, 39, 43, 44, 52, 54, 59, 114, 119, 123, 166, 167, 169
- Δt_{sync} Synchronization time during gear shift. 14, 129–132
- ω_{mech} Mechanical angular speed [rad/s]. 129, 130
- θ_{elec} theta: Electric angular position of the rotor. 25, 63, 90
- \vec{i}_{demag} Demagnetization current: working point where the magnetic field produced by the magnets is neutralized by the field created by the stator. This point is the center of the voltage limit ellipses and has the lowest flux linkage equal zero. The current vector is deviated towards this point in order to reduce the induced voltage when high speeds are desired. 35
- k_{belt} belt ratio: transmission ratio between the EM and the input shaft. 11, 13, 17, 19, 20
- AMT** Automated Manual Transmission: A manual gearbox that is actuated by a robot arm and the decision to change gears is taken by a computer instead of the driver. 9–12
- AR** Dr. Avo Reinap. Assoc. Prof. at IEA. Lund University. co-advisor of this thesis. 22
- Brake Bench** Test equipment used to measure the internal properties of *EMs* using a brake motor, torque sensor and possibly other parts such as gearbox. Tests on a brake bench are mainly static where the current, voltage, torque and speed can be kept constant during a long time.. iv, xiii, 3, 5, 67–69, 71, 72, 74, 110, 135, 136, 167

CPSR Constant Power Speed Range. 128

DCC Direct current control: Hysteresis band based current control. xxiii, xxiv

Dynamic Test Method Convenient method presented in this thesis, to measure the properties of a iPMSM without the need of a brake Bench. iv, xiii, xvii, xx, xxi, xxiii, xxiv, 3–5, 65, 70, 72, 74, 75, 110, 135, 136, 139, 141, 143

EHV Hybrid Electric Vehicle. iv, xiii, 2–4, 7–9

EM Electric Machine: Electric motor that can also work as a generator. iv, xiii, 2–5, 7–9, 11–15, 17–20, 23, 24, 29, 30, 38, 56, 62, 63, 65–67, 69, 71, 90, 126–128, 130, 132, 133, 135, 136, 138, 165

FEA Finite Element Analysis. xviii, 4, 22, 24, 27, 37–42, 50, 56, 57, 130

FEMM Free Software developed by , Ph.D.David Meeker. FEMM is a suite of programs for carrying out low frequency electromagnetic calculations on two-dimensional planar and axis-symmetric domains. The program currently addresses linear/nonlinear magnetostatic problems, linear/nonlinear time harmonic magnetic problems, linear electrostatic problems, and steady-state heat flow problems.
<http://www.femm.info>. 4, 22–24, 27, 42, 135

FPGA Field Programmable Gate Array: Programmable integrated circuit capable of running several parallel processes truly in parallel, contrasted with microprocessors that alternate between tasks. FPGAs are very reliable, deterministic and fast once the compilation is done. On the other hand they are slightly more difficult to program and the compilation takes several minutes. In this projects it is used for accurate motor control.. xix, xx, 71, 90, 120, 136, 140

ICE Internal Combustion Engine: Here, the motor that runs on fuel, such as gasoline, diesel, etc. in a hybrid or in a conventional car. 2, 8, 11, 13, 14, 18, 19, 30, 127, 128, 131, 132, 135

IEA Industriell Elektroteknik och Automation: Division of Industrial Electrical Engineering and Automation at Lund University. Division where this PhD thesis work has been realized. www.iea.lth.se. iv, xiii, xv, xvii, xviii, 3, 7, 18, 22, 72, 73, 136, 137

LUT Look Up table: table containing appropriate current vectors for a required torque at a certain speed or flux. Used for optimal motor control and to reach high speeds. 4, 5, 120, 122, 170

PEC Power Electronics Converter: Component of the control unit that is connected on one side to the DC-link voltage and to the 3 phases of the electric machine on the other side. The *PEC* uses IGBTs and freewheeling diodes to regulate the amount of time each phase is connected to the dc-link-voltage. This creates a seemingly variable phase voltage, which is used to regulate the current. 21, 49, 66, 71, 93, 133, 141, 142, 170

RF-Design Radial Flux Design: semi-automated, iterative, rapid CAD, CAE design tool of radially magnetized electrical machines, developed by *Avo Reimap* at the division of *IEA*. It uses Matlab and *FEA* toolbox *FEMM*. xxiii, 3, 4, 22, 23, 135

SCMG Single Clutch Manual Gearbox. 10, 11

SPM Surface Mounted Permanent Magnet Machine: *EM* where the magnetic field is provided only by permanent magnets. In difference to *iPMSM* the inductance is equal in all the angular directions perpendicular to the rotor axis and therefore it can not produce reluctance torque. 20

YL Yury Loayza. The author of this doctoral thesis. He carried out his Ph.D. studies at the div. of *IEA* at Lund University. xxiii–xxv, 3, 65

complex hybrid Electric hybrid topology used for example in the Toyota Prius which uses a planetary gearbox. 9

iPMSM inserted Permanent Magnet Synchronous Machine: *EM* where part of the magnetic field is provided by permanent magnets which give them high torque density. The inserted permanent magnets create a difference in the rotor inductance at different directions which can be used to produce increased reluctance torque. 3–5, 17, 18, 20, 22, 27, 31, 32, 35, 40, 45, 46, 49–51, 65, 69, 71–75, 79, 85, 125–128, 130–133, 135–139, 141, 153, 166, 168, 170, 174

iso-torque line on the current vector plane that joins the points that produce the same torque (iso=same). 44

Parallel Drive Bench Bench used in this thesis to simulate the dynamics of a car during gear shift. The most characteristic components are: Large Flywheels that resemble the inertia of the vehicle, a sequential manual gearbox, robot arm for gear selection and belt transmissions. 13, 165

Chapter 1

Introduction

1.1 Motivation for the development of electric drives for vehicles

The motivation of this thesis is to contribute to the development of electric hybrid drive trains for vehicles, which is meant to have a positive impact on the environment and on the health of people.

1.1.a Background and importance of Electric Hybrid Vehicles

Some of the first vehicles developed in the late 19th century were powered by electricity. But during the 20th century the use of fossil fuels increased drastically. The use of fossil fuels has many known disadvantages for the environment and people's health as well as the low efficiency of combustion engines, and the availability of fossil oil and gas is limited. Nowadays, the transport sector accounts for approximately 30% of the energy consumption in Europe [8] and USA [9] for example. And most of the energy used by cars comes from fossil fuels.

The advantages of using electric power instead of fossil fuels is clearly seen for example in the fact that electric machines were used instead of combustion engines as soon as it was possible. For example, for motors in factories, elevators, trams or trains. There the motors could be continuously supplied with electricity from the grid.

But mobile machines as cars, ships, and airplanes continue to rely on fossil fuels where large amounts of energy could be stored quite simply in the fuel tank. Storing equivalent amounts of energy in the form of electricity requires large and expensive batteries with limited service life length.

Higher fossil fuel prices, increased environment and health awareness as well as technical developments in electric drive technology, have contributed in recent years to an increased development and production of *Electric Hybrid Vehicles (EHVs)* and pure electric vehicles.

Due to higher fuel efficiency of *EHVs*, the emissions of CO_2 for a given traveled distance can significantly be reduced. Even more if it is possible supply the vehicle with electricity from the electric grid as in the case of *Plug-In- or Slide-in-EHVs*. As is well known, CO_2 is one of the gases most responsible for the *Green House Effect* on earth.

EHVs that can run on pure electricity in city traffic, for example, have also the advantage of reducing the local pollution by not releasing NO_x , CO and particles.

1.1.b Importance of cost effective hybrid vehicle topologies

The benefits of electric hybridization will have a larger global impact on the environment and on people's health, if many regular price cars use it, than if a small number of expensive vehicles are hybrid or purely electric, i.e. if hybridization focuses on low price, large volume car models. For this reason, this project is based on a cost efficient hybrid topology which could be installed in the most common car models in a relatively easy manner.

The hybridization process of vehicles often requires the development of new customized *Electric Machines (EMs)* for optimal integration with the *Internal Combustion Engine (ICE)* and the transmission. The use of *EMs* for powering vehicles, entails new requirements for power, torque, speed range, size, weight, dynamics on the *EMs*, that all need to be satisfied together.

This thesis work goes through the design and prototyping of an *EM* customized for this cost-effective hybrid topology. This *EM* is designed not only for powering the vehicle but also for speeding up the gearshift process, which will reduce the cost of the transmission and will maintain driving comfort and vehicle performance.

1.1.c Improved techniques that facilitate the development of electric drives

Nowadays large amounts of new different types of *EMs* for powering vehicles have been designed and developed in universities and in industry. New tools and techniques that facilitate the processes of designing, manufacturing, evaluation and controlling *EMs* are also of crucial importance.

In this thesis, a design tool developed at the *Division of Industrial Electrical Engineering and Automation (IEA), RF-Design*, is used and evaluated for the design of the *EM*.

Another important step in the development process is the test and evaluation of prototypes or commercial *EMs*. This process normally requires a *Brake Bench* which is a large, advanced, expensive piece of equipment and the process is time consuming. This traditional test method changes the properties of the machine during testing because of heat generation.

During the development of a new control system that the new *EM* required, the author of this thesis, *Yury Loayza (YL)* came up with the idea and developed a new method for measuring the internal properties of these types of *EMs*, namely *inserted Permanent Magnet Synchronous Machines (iPMSMs)*. This new method is called here the *Dynamic Test Method* [2].

In this thesis, the *Dynamic Test Method* is further described in detail. This method simplifies the evaluation process by eliminating the need for a *Brake Bench*. This method is fast, requires less equipment, and has increased precision compared to the traditional test method.

The results of this thesis. i.e. the description of the design process of the *EM*, the study of the properties of the final prototype and the *Dynamic Test Method* are intended to become part of the useful resources that can help researchers and developers in the process of developing a cleaner and more environmental friendly transportation.

1.2 Arrangement of the thesis

Chapter 1 contains the introduction, placing the project in a larger context, and describing the thesis structure and contributions of the project.

Chapter 2 describes the actual *EHV* topology on which this thesis is based and

establishes the specifications for the new *EM*.

Chapter 3 describes the design and optimization process of the customized dynamic *iPMSM*, presents the expected machine characteristics obtained from *Finite Element Analysis (FEA)*, as well as the prototype.

Chapter 4 introduces the *Dynamic Test Method* with its importance, benefits, and characteristics.

Chapter 5 describes the *Dynamic Test Method* for characterizing *iPMSMs* with corresponding theory, methods, equations and measured data. Machine properties obtained using the method are also presented here as for example torque and flux maps as a function of current vectors, etc.

Chapter 6 describes the creation of *Field Weakening Look Up tables (LUTs)* for machine control using speed and torque as input parameter, which allows it to reach speeds many times above the nominal speed. This chapter also presents machine properties as losses and efficiency as a function of speed and torque. And finally it evaluates the expected dynamic performance of the *iPMSM* in its *EHV* application.

The *appendix* contains a general description of the experimental set up, tables with detailed *EM* data obtained from the measurements and calculations, *CAD* drawings of the *EM*, data sheets and other detailed data used for the calculations.

1.3 Contributions

1.3.a Description of the design process of an electric machine

In *Chapter 3* the author describes in detail the design and optimization process of a high dynamic *iPMSM* for powering a parallel hybrid car where the *EM* is connected to the gearbox.

The information presented in this work is intended to serve as an example for readers interested in developing electric machines or understanding how the process is done. Of special interest is that the whole process from concept to final optimized design can be done with software that is either free or can easily be accessed by many students, such as *Matlab*, *RF-Design* and *FEMM*.

1.3.b The final design of a highly dynamic electric machine

This thesis also presents the geometry and the electromagnetic properties and other data of the final prototype of this highly dynamic *iPMSM*. This data can be useful:

- as example of *EM* for a parallel hybrid vehicle
- as input for simulations of hybrid topologies
- as a start point for other designs
- for comparison with other designs of *EMs*, as a tested parameter configuration among the large amount of possible configurations
- The prototype is used for further testing of the hybrid drive train and as test object for development of measurements and control methods for *EMs*

1.3.c The *Dynamic Test Method*

Another important contribution, is the conception, development and *proof of concept* of the *Dynamic Test Method* for its innovative value, benefits and practical implications.

Specially, torque and flux maps, that are the finger print of *iPMSMs*, were previously obtained from numerical simulations or static tests in a *Brake Bench*, at least in the near research community known by the author. The *Dynamic Test Method* is a more convenient, economic, time saving and precise alternative method of measuring the properties of an *iPMSM*.

1.3.d Field weakening control for speeds beyond nominal speed

Vector control for reaching speeds up to approximately 5 times the nominal speed of the *iPMSM* is implemented and tested. *LUTs* for field weakening are created for this purpose and measurements of the acceleration up to 15000 [rpm] are displayed.

Chapter 2

Cost effective topology for an electric hybrid vehicle

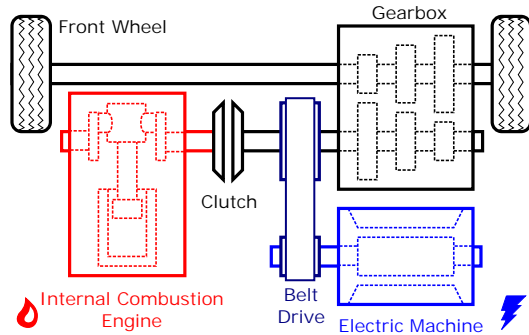
At the *Division of Industrial Electrical Engineering and Automation (IEA)* different *Electric Hybrid Vehicle (EHV)* topologies are studied, in cooperation with the automotive industry, intended to facilitate the hybridization of existing vehicle models, among others:

- Parallel hybrid for a light vehicle where the *Electric Machine (EM)* is coupled via the gearbox to the front wheels, which is studied in this thesis work
- Rear wheel drive for a light vehicle with the *EM* coupled to the wheels [10] [11]
- Heavy vehicle, parallel hybrid with the *EM* coupled via the gearbox [12] [13].

2.1 The cost effective hybrid topology

The parallel hybrid topology for a light vehicle where the *EM* is coupled via the gearbox to the front wheels consists of maintaining the common front wheel drive on a vehicle almost unchanged, removing the electric start motor and adding a compact, medium power *EM* placed on the side of the gearbox and connected to the input shaft as shown in *figure 2.1*.

Figure 2.1: Topology of the hybrid drive train



Placing the *EM* at this position gives great flexibility for the power flow, at this position the *EM* can be used:

- to start the *Internal Combustion Engine (ICE)*
- as a generator
- to contribute to the power demanded from the *ICE*, by letting the *ICE* run at more efficient working points
- to improve the vehicle dynamics due to fast response of the *EM*
- to run the vehicle in pure electric mode in city traffic
- to increase the total power to the supplied to the wheels in so called *boosting mode*
- for regenerative braking
- for quick start of the vehicle using high torque at low speeds from the *EM*
- for speeding up the synchronization of the shafts in the gearbox during gearshift

While the first ones are general advantages for parallel *EHVs* [14], the last one, of speeding up the synchronization of the shafts in the gearbox during gear shift is a key point in this topology compared to other parallel *EHV* topologies and is studied deeper in the following sections.

This topology has been previously studied with numerical simulations and experimental tests:

- [15] studies the transmission and the gear shifting process, focusing on the time needed for shaft synchronization, using numerical simulations and concludes that using one single external *EM* is the most suitable setup for

an *EM* assisted *Automated Manual Transmission (AMT)* and that the synchronization time specifications can be achieved

- [16] studies different alternatives for hybridizing an *Opel Astra* from *General Motors* which is considered a large volume, low price private car model. It compares, parallel hybrid, series hybrid, complex hybrid with different electric power levels and recommend an *EM* with an nominal power of $P_{nom} = 15[kW]$ rather than a $P_{nom} = 40[kW]$
- [17] and [18] present the results of experimental tests on shaft synchronization during gear shift using a non customized *EM* and highlight the need of a customized *EM* and more gears in the gearbox
- and this doctoral thesis goes forward with the development of a customized *EM* optimized for this topology

This topology is meant to be easy to implement in the most common models of private cars, due to the few changes in the conventional drive train and allows the price of the transmission to be kept down as explained in the following sections.

2.1.a Importance of low cost, large volume systems

The philosophy behind this low cost system is that, to make a greater positive impact on the environment it is important that a large number of vehicles reduce their emissions. Therefore, this idea focuses on the hybridization of common, regular price cars with reduced hybridization cost.

Accordingly, it is important to keep the price of the components down and make it easy for the car manufacturers to adapt their production lines to produce *EHVs*.

This hybrid topology is relatively easy to implement in existing car models, keeping down the price of the components, as for example the transmission, without sacrificing either the performance or the comfort of the vehicle.

Other topologies such as the *serial hybrid* or *complex hybrid* topologies would require larger changes in the vehicles and more expensive components.

2.1.b Automated single clutch manual gearbox to reduce costs

Driver controlled manual gear box is no longer appropriate in hybrid systems where the power flow is so complex that an automated system is needed to handle both, motor torque control split between the combustion engine and the electric drives as well as the gear shifting, instead of the driver.

Driving comfort is to a part dependent on a minimum of torque interruptions during e.g. an acceleration. Commonly this is accomplished by using a dual clutch or an automatic transmission, but these transmission have some disadvantages compared to the *Single Clutch Manual Gearbox (SCMG)*.

The *SCMG* compared to the *Automatic Gearbox* has lower price, higher efficiency, less weight and size. *Dual clutch gearboxes* have good efficiency and performance but are heavier, larger and more expensive than the *SCMG* [19].

Therefore, components costs for the hybridization can be reduced, without sacrificing either the comfort or the performance, by reusing the *SCMG* and implementing a fast *AMT*.

2.1.c Fast electric machine assisted automated manual transmission for maintained comfort and performance

During gear shifting the *output shaft*, which is connected to the wheels, keeps its speed in principle constant during this short gear shifting time because of the large inertia of the vehicle, see *figure 2.2*. The *input shaft* on the other hand has to change its speed to the one corresponding to the new gear ratio *figure 2.3*.

Figure 2.2: The speed of the *output shaft* remains unchanged under gearshift. The *input shaft* needs to adapt to the speed corresponding to the new gear ratio.

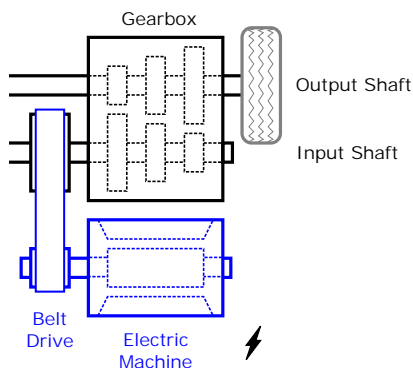
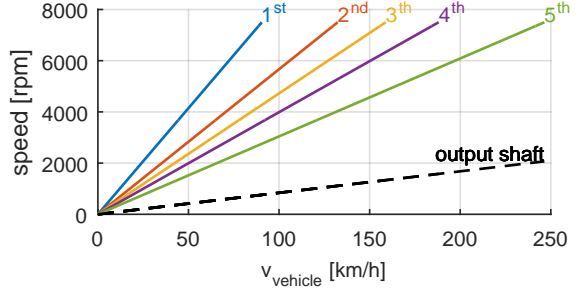


Figure 2.3: Speed of the input shaft for different gears, and speed of the output shaft, vs. the vehicle speed



When using a *SCMG*, the input shaft needs to be disconnected from the output shaft during a short time during gear shift for speed re-synchronization. During this synchronization time, no torque can be transmitted from the *ICE* to the wheels.

In cars with manual gearbox and no *AMT*, the driver decides when to shift gears and this torque interruption time is less of a concern. But when using an *AMT*, this torque interruption time can come suddenly, especially when the driver is trying to accelerate.

If this interruption time is too long, more than half of a second for example, it can be uncomfortable and even affect the driving process negatively. Therefore the maximum allowed time for gearshift, according to [15], is set to:

$$\Delta t_{gearshift,max} = 100 [ms] \quad (2.1)$$

2.1.d Long and slender rotor for high dynamics

In this *EM* assisted *AMT* the *EM* is used to synchronize the input shaft. To speed up this process, i.e. reach high angular acceleration of the rotor, it is important to keep down the inertia of the rotor of the *EM* and of the reflected inertia of the input shaft as well as of the other linked components, such as the belt transmission. At the same time, the torque and power delivered by the *EM* need to be high (eq. 2.2).

$$\frac{d\omega_{mech}}{dt} = \frac{T}{J_{rotor} + \frac{J_{input_shaft}}{k_{belt}^2}} \quad (2.2)$$

In (eq. 2.2) the inertia of the belt transmission is not considered for simplicity.

This thesis focuses on keeping down the inertia of the rotor J_{rotor} and the inertia of the other components is not further optimized.

In general the torque produced by a the radial flux EM is proportional to the mantel surface of the rotor [20], which imply that for a given axial length, the Torque is roughly proportional to the square of the radius.

$$T = k \cdot l \cdot r^2 \quad (2.3)$$

And the inertia J_{rot} of the rotor is proportional to the 4:th power its radius.

$$J_{rot} = \frac{1}{2} m r^2 = \frac{1}{2} \rho_{dens} l r^4 \quad (2.4)$$

This implies that the acceleration that the rotor could achieve, disregarding external components, which is

$$\left(\frac{d\omega_{mech}}{dt} \right)_{rotor} = \frac{T}{J_{rotor}} \quad (2.5)$$

is inversely related to the square of the radius.

$$\left(\frac{d\omega_{mech}}{dt} \right)_{rotor} = \frac{2k}{\rho_{dens} l} \frac{l r^2}{r^4} = \frac{k_2}{r^2} \quad (2.6)$$

By placing the EM parallel to the gearbox, see *figure 2.1*, it is possible to design an EM with a long and slender rotor with low inertia which will increase the dynamics and reduce the time for gear shifting.

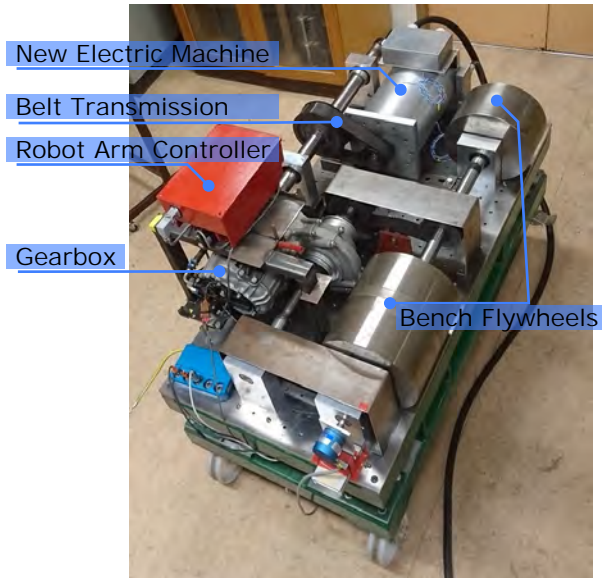
The synchronization time is further studied in detail in *section 6.3* with measured data of the customized EM .

Other topologies of AMT place the EM concentric to the input shaft. Because of the limited space in the axial direction, the EM is forced to have short axial length and large diameter for a given torque. The large rotor diameter increases the inertia J_{rotor} , and then the synchronization time.

Automatic and dual clutch transmissions have not torque interruption time. To compete with them, the single clutch AMT should be able to change gears very fast.

As mentioned before, this parallel hybrid topology has been studied in previous projects at the division of *IEA* [17] and [18], using the *Parallel Drive Bench* shown in *figure 2.4*. There *large bench flywheels*, that represent the mass of a car, are accelerated from standstill to a top speed through different gear ratios. In these projects a previously existing, commercial, not customized *EM* is used as the mechanical power source and for shaft synchronization in the gearbox during gear shifting. The *EMs* used for these tests had limitations of torque, speed and dynamics. The need for a new customized *EMs* is clear.

Figure 2.4: The *Parallel Drive Bench* with the new customized *EM*



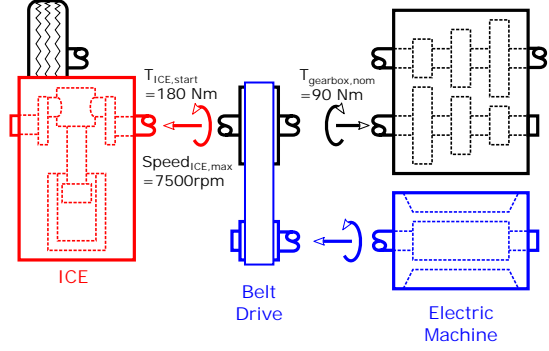
2.2 Specifications of the electric drive

The outcome from gear shifting sequences such as time and acceleration requirements, together with torque, speed and power needed for vehicle traction and integration with the *ICE*, is used as an input to the machine design in this thesis with the specifications listed below.

The transmission ratio k_{belt} between the *EM* and the input shaft is determined in section 3.1.b. Here the specifications are given at the input shaft, see *figure 2.5*.

The following bullet list defines values obtained in cooperation with the automotive industry, *Tommy Lindholm* previously working at *Saab Automobile*, and from previous studies.

Figure 2.5: Transmission between the *EM* and the *ICE* and the gearbox via a belt drive



- Nominal power of the *EM* to power the vehicle in city traffic and for gear shift synchronization [16]

$$P_{nom} = 15 [kW] \quad (2.7)$$

- Nominal continuous torque supplied by the *EM* at gearbox input shaft for being able to power the vehicle in city traffic, see *figure 2.5*

$$T_{gearbox,input,nom} = 90 [Nm] \quad (2.8)$$

- Peak torque at the *ICE* shaft for starting it at $-40^\circ C$

$$T_{ICE,start} = 180 [Nm]$$

- Maximal speed at the *ICE* shaft to be able to be connected to the *ICE* shaft at any time

$$speed_{ICE,max} = 7500 [rpm] \quad (2.9)$$

- Time available to synchronize the shaft in the gearbox during Automated Gear Shifting (from eq. 2.1).

$$\Delta t_{sync} = 100 [ms] \quad (2.10)$$

- Maximum length and diameter of the electromagnetic active components of electrical machine i.e. rotor and stator (housing not included)

$$L_{EM,stator} = 200 [mm]$$

$$\varnothing_{EM,stator} = 180 [mm]$$

- Battery voltage

$$U_{dc,batt} = 300 [V] \quad (2.11)$$

The main focus of the *EM* design is on the optimization of the thermal and electromagnetic properties of the active part of the *EM*, i.e. the rotor and the stator. This project on the other hand, does not go deeply into the optimization of the housing, where only a basic geometry is used.

Chapter 3

Design of the electric machine

3.1 Specifications of the electric machine

With the specifications of the electric drive at the input shaft in *section 2.2* the next step is to determine the belt transmission ratio k_{belt} between the *Electric Machine (EM)* and the input shaft as well as the type of *EM* and other characteristics to determine the specifications for the *EM*.

3.1.a Speed requirements

Considering the specification of high torque density, low rotor inertia and limited space inside the vehicle an *inserted Permanent Magnet Synchronous Machine (iPMSM)* is chosen as the appropriate type of *EM* for this application.

In order to maximize the available power, $P = \omega \cdot T$, of an *iPMSM* that needs to fit in a limited volume, it is appropriate to consider that the size of the *EM* is directly related to the torque [20] and [21].

The torque is proportional to the size of the magnets, the mantel area of the rotor and to the applied current. Higher current will require a larger quantity of copper in the windings and a larger quantity of iron to avoid magnetic saturation. This results in a larger machine for higher torque.

Higher speed may also require a slightly larger iron core in order to keep down the so called iron losses P_{Fe} . At the same time high speed will also require better insulation due to higher voltage, but this will not affect the size of the

windings in the same way as the need for higher current.

According to the definition of mechanical power, $P = T \cdot \omega$, high power density can then be achieved by keeping down the torque and increasing the speed as long as it practical, efficient and mechanically achievable.

But other factors limit the rational top speed of the EM, such as:

- Centrifugal forces of the magnets inside the rotor
- Resonance speed of the rotor shaft
- Centrifugal forces in the belt
- More accurate and advanced measurement and control system to run the EM
- Limited switching frequency of the *IGBTs*, app. $10 [kHz]$
- Maximum permissible speed for the resolver, here $30000 [rpm]$, see *figure D.2*

In this project, the speed limit is chosen to:

$$speed_{EM,max} := 15000 [rpm] \quad (3.1)$$

This value is chosen based on the experience of previously constructed *iPMSMs* at the division of *Division of Industrial Electrical Engineering and Automation (IEA)*, *iPMSMs* used in previous projects for this hybrid topology, and considering for example the top speed of rotating components of the transmission of a conventional vehicle $7500 [rpm]$.

This speed would make it possible to construct the *EM* with conventional materials, components and technology, which is desirable for cost-effective topology. Since this speed is twice the speed of the *Internal Combustion Engine (ICE)*, the capabilities of the *iPMSM* of being able to run faster than the *ICE* is utilized well.

3.1.b The belt transmission ratio

In previous studies a *belt transmission* between the *EM* and the input shaft has been proposed [18]. This implies the following relations for the speeds and torque

$$k_{belt} = \frac{\omega_{EM}}{\omega_{gearbox}} \quad (3.2)$$

neglecting the losses: $T_{EM} = \frac{T_{gearbox}}{k_{belt}}$

The belt transmission ratio is determined by the top speed of the *ICE* and the one of the *EM*:

$$k_{belt} = \frac{speed_{EM,top}}{speed_{ICE,top}} = \frac{15000}{7500} := 2 \quad (3.3)$$

In *figure 3.1* we can see the required *EM* torque for different belt transmission ratios. We see that for $k_{belt} > 2$ the torque curve has already flattened. Increasing the belt ratio beyond 2, and in this way increasing speed of the *EM*, would not save much space, and higher speeds would bring other complications.

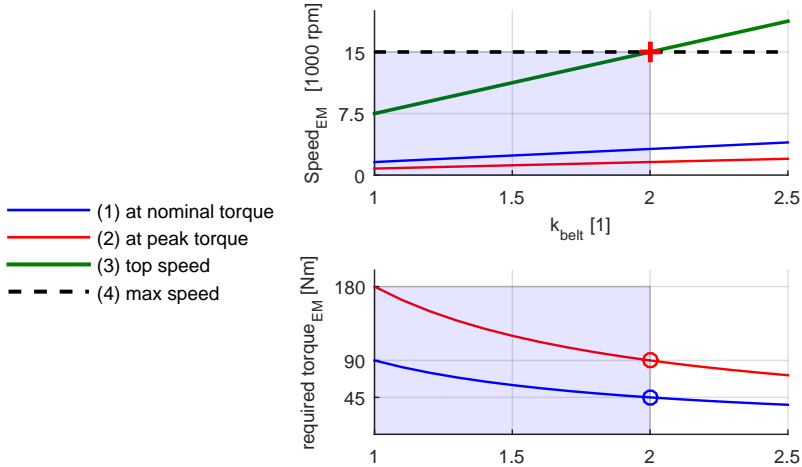


Figure 3.1: The belt speed ratio. The required torque decreases with k_{belt} but the maximal allowed speed limits k_{belt} to 2

3.1.c Nominal torque, speed and constant power speed range

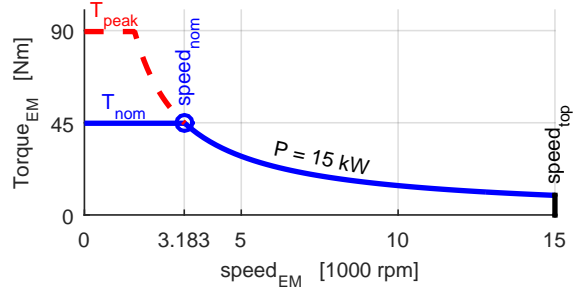
Besides the nominal values, the *EM* is required to have a large *constant power speed range*, torque overload capabilities with peak torque twice the nominal

torque, and peak power during a short time. Because of that, an *iPMSM* is selected as the most appropriate *EM* type instead of a *Surface Mounted Permanent Magnet Machine (SPM)* for example [22].

The paper [23] list other practical advantages of *iPMSM* and propose an interesting method for reducing the flux leakage characteristic of this *EM* configuration.

With the *belt transmission ratio* $k_{belt} = 2$, the specifications for the *EM*, see *figure 3.2*, are:

Figure 3.2: Power, torque and speed specifications for the electric machine



$$T_{EM,nominal} = \frac{T_{gearbox}}{k_{belt}} = \frac{90 \text{ Nm}}{2} = 45 \text{ [Nm]}$$

$$T_{EM,peak} = \frac{T_{ICE,start}}{k_{belt}} = \frac{180 \text{ Nm}}{2} = 90 \text{ [Nm]}$$

$$\omega_{0,EM,mech} = \frac{P_{EM}}{T_{EM,nominal}} = \frac{15000 \text{ W}}{45 \text{ Nm}} = 333.3 \text{ [rad/s]}$$

Table 3.1: Speed and torque specifications of the *EM*

| machine type | radial flux <i>iPMSM</i> | | |
|----------------|--------------------------|-----------------------------|---------------------|
| nominal power | P_{nom} | := | 15 kW (eq. 2.7) |
| nominal torque | T_{nom} | := | 45 Nm |
| peak torque | T_{peak} | := | 90 Nm |
| nominal speed | $\omega_{nom,mech}$ | $= \frac{P_{nom}}{T_{nom}}$ | = 333.33 rad/s |
| | $speed_{nom}$ | = | 3183 rpm |
| top speed | $speed_{top}$ | := | 15000 rpm (eq. 3.1) |

3.1.d Number of pole pairs

Numerical simulations show that the torque increases with the number of pole pairs when comparing $n_{pole\ pairs} : 2, 3, 4, 5$. The increment is larger for low $n_{pole\ pairs}$, then the torque begins to flatten.

The highest number of pair of poles is limited by the maximum recommended switching frequency of the *IGBTs*. The *Power Electronics Converter (PEC)* used for this project has a max. recommended switching frequency of:

$$f_{sw} = 10 [kHz]$$

In order to give the current in the phases a fairly sinusoidal shape, it is necessary to switch at least 10 times per electric period, i.e. the highest allowed electric frequency is

$$f_{el,max} = 1 [kHz]$$

The top electric frequency for different number of pole pairs is presented in table 3.2. $n_{pole\ pairs} = 4$ is good but for $n_{pole\ pairs} = 5$ the top electric frequency becomes too high considering the switching frequency.

Table 3.2: Electric frequency for different number of pole pairs, at 15000 [rpm]

| $n_{pole\ pairs}$ | f_{el} | |
|-------------------|-----------|----------|
| 3 | 750 [Hz] | |
| 4 | 1000 [Hz] | ok |
| 5 | 1250 [Hz] | too high |

The selected number of pole pairs and the corresponding electric nominal speed

$$\omega_{0,elec} = n_{pole\ pairs} \cdot \omega_{0,mech}$$

are presented in (table 3.3)

Table 3.3: Selected number of pole pairs

| | | | | |
|----------------------------|-------------------|----|---------|-------------------|
| | $n_{pole\ pairs}$ | := | 4 | |
| mech. nominal speed | $\omega_{0,mech}$ | = | 333.33 | rad/s (table 3.1) |
| electric nominal speed | $\omega_{0,elec}$ | = | 1333.33 | rad/s |
| electric nominal frequency | $f_{0,elec}$ | = | 212.207 | Hz |

3.2 Fast optimization of the internal parameters of the electric machine

The design and optimization of the *iPMSM* is done using *Matlab*, *RF-Design* toolbox and *FEMM* software.

FEMM is a 2D *Finite Element Analysis (FEA)* software and *RF-Design* is a rapid *CAD/CAE* design tool for radially magnetized electrical machines developed by *Avo Reinap (AR)* at *IEA*. *RF-Design* is also used in other projects for designing electric machines for other applications or topologies such as [24] [11] [13].

The design process is described in more detail in [1], here in *figure 3.3* and on the following sections:

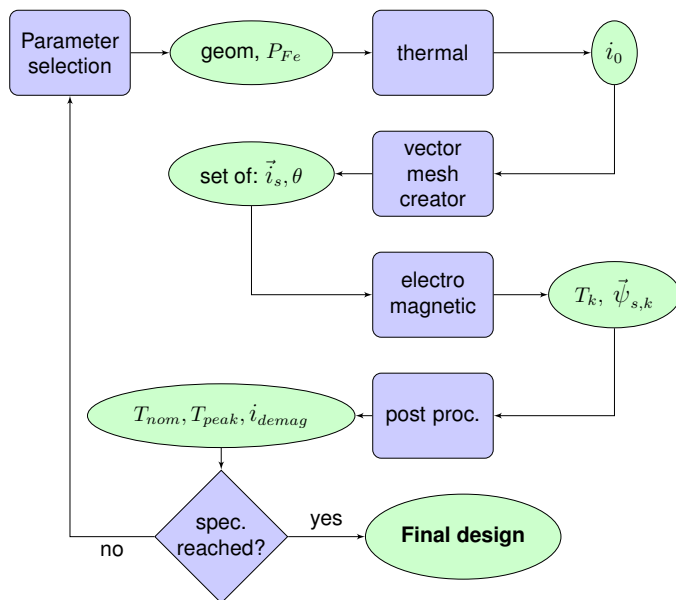


Figure 3.3: Flowchart of the optimization process

3.2.a Parameter selection

A large set of parameters as:

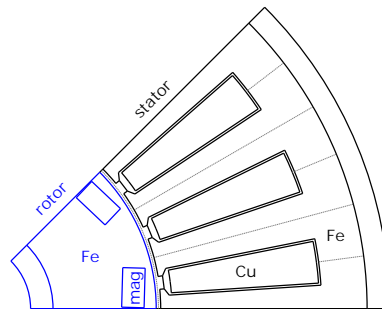
- geometric dimensions and proportions: radii, number of pole pairs, etc
- material properties
- boundary conditions and loads

are chosen for the first iteration based on previous experience or arbitrarily. For the following iterations the parameters are updated depending of the results either manually or using some semi automated standard optimization method. Because of the complex geometry of the *EM* fully automated parameter selection has not been possible in this study.

3.2.b Geometry of the electric machine

RF-Design draws a 2d-geometry of one pole of the *EM* on *FEMM* using *LUA* script (see figure 3.4). RF-design assigns material parameters, boundary conditions, loads, etc to the different regions of the 2D geometry.

Figure 3.4: Model of the *EM* in *FEMM*



3.2.c Thermal finite element analysis

A steady state thermal analysis is performed by *FEMM*. An amount of current is selected, which is translated to heat generation P_{Cu} in the copper windings due to resistive losses

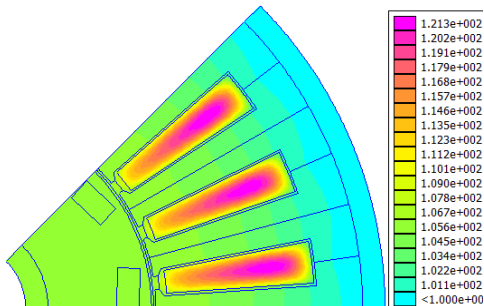
Heat generation P_{Fe} caused by the changes in the magnetic field at the nominal frequency f_0 in the iron is applied to the regions that consist of iron according

to the iron plate data sheet. This data sheet is a 2D table that has frequency and mean magnetic flow density B_0 as parameters.

To simulate the effect of water cooling a boundary condition of constant temperature $\vartheta_{s,out} = 100^\circ\text{C}$ is set at the outer mantle of the stator

FEMM solves the steady state thermal calculations and outputs a temperature distribution over the EM, and in particular, the highest temperature found on the *EM*, see *figure 3.5*.

Figure 3.5: Temperature distribution over the *EM* [$^\circ\text{C}$]



The current density J_0 is varied and the thermal calculation is repeated until the highest current density is found in which the maximum temperature on the EM does not exceed the predefined thermal margin.

In this case the temperature limit is set to $\vartheta_{max} = 120^\circ\text{C}$. Too high temperatures can damage the insulation of the copper wires and permanently decrease the magnetic strength of the magnets.

3.2.d The nominal current i_0

The result of the thermal *FEA* is the nominal current density J_0 which is the highest current density that can be applied to the slots of the EM continuously, under nominal conditions, without trespassing any thermal limit inside the EM.

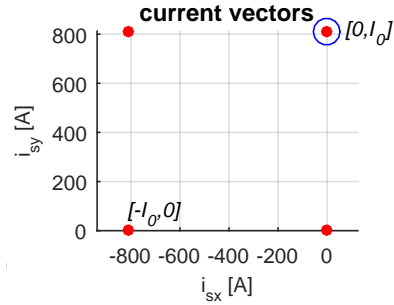
The magnitude of the nominal current vector i_0 is calculated from J_0 and the copper area A_{cu} in the slots using the *power invariant park transformation*

3.2.e Mesh of current points

A mesh of current points \vec{i}_s to be analyzed is generated. Commonly the selected current points are multiples of the nominal current i_0 in the rotor coordinate

system i_{sx} - i_{sy} -plane (see figure 3.6)

Figure 3.6: Mesh of current points in the rotor coordinate system



3.2.f Phase currents values as a function rotor angular position

θ_{elec}

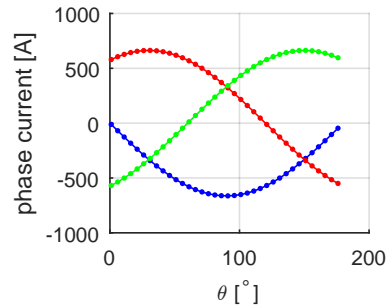
For each current vector of the set, *RF-Design* calculates the corresponding current values in the phases $[i_a, i_b, i_c]$ using the *power invariant park transformation* [5].

The phase currents $[i_a, i_b, i_c]$ not only depend on the current vector $[i_{sx}, i_{sy}]$ but also on the angular position θ of the rotor. In this project the rotor is rotated over one *pole* i.e. $180^\circ_{electric}$, which corresponds to 45°_{mech} for $n_{pole\ pairs} := 4$. The rotor is rotated in steps of $\Delta\theta_{elec} = 5^\circ_{electric}$.

$$\theta_{elec} = n_{pole\ pairs} \cdot \theta_{mech}$$

The phase currents, for each current point, during rotor rotation form 3 sinusoidal waves which are phase shifted with $120^\circ_{electric}$ (see figure 3.7)

Figure 3.7: Phase currents, corresponding to one current point, during rotation



3.2.g Electromagnetic finite element analysis

RF-Design feeds this current values together with the other necessary parameters to the *FEMM* model. In this case where 4 current vectors are analyzed at 36 rotor positions. *FEMM* performs 144 *FE* calculations (see figure 3.8).

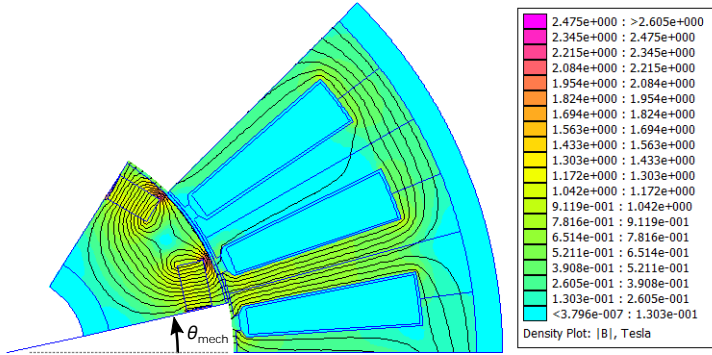


Figure 3.8: Electromagnetic Finite Element Analysis to determine the Torque T and the flux-linkage $\vec{\psi}$

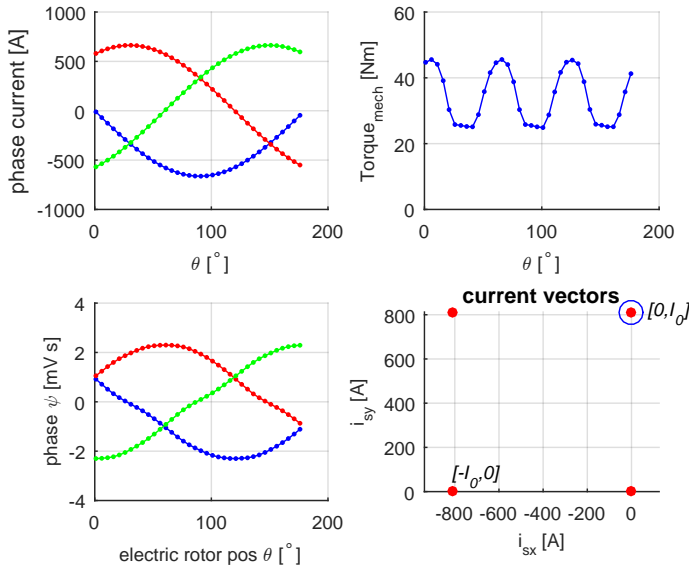


Figure 3.9: FEMM output: phase current $[i_a, i_b, i_c]$, torque T and phase flux-linkage $[\psi_a, \psi_b, \psi_c]$ for one of the current vectors (blue ring)

This is one of the most computational time-demanding steps of the optimizations process. At the time of running this optimization in year 2015 these 144 *FE* calculations, 4 current vectors by 36 angular positions, take 20 minutes using an up-to-date personal computer.

For every *FEA* calculation, *FEMM* outputs the 3 phase currents $[i_a, i_b, i_c]$, one torque value T and 3 phase flux values $[\psi_a, \psi_b, \psi_c]$. (see figure 3.9)

From the flux values for each phase $[\psi_a, \psi_b, \psi_c]$ shown in (figure 3.9) the corresponding flux values as vector $[\psi_{sx}, \psi_{sy}]$ are calculated according the *Park Power Invariant Transformation* (see figure 3.10) and considering the number of pole pairs of the machine.

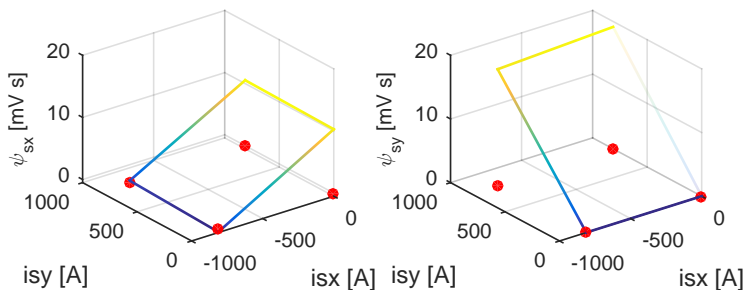


Figure 3.10: The flux linkage as vector $[\psi_{sx}, \psi_{sy}]$ is calculated for the 4 selected current vectors. Note that ψ_{sx} depends mainly on i_{sx} and ψ_{sy} on i_{sy}

Note: The phase flux calculated by *FEMM* is the flux over each slot. This value is multiplied by the number of poles of the *iPMSM* because all slots that correspond to a phase are connected in series, one *plus* and one *minus* per pole pair.

3.3 Post processing of the results from the *finite element analysis*

3.3.a Interpolation of the flux

Based on the flux values for this four edges of the rectangle, the flux values for points inside the rectangle are interpolated (see figure 3.11). This is a fast estimation to find the optimal current point the inside this region. Of course the larger the saturation the less accurate this linear interpolation is. But in

the fast optimization process, this is an efficient method to compare different motor designs when optimizing the geometry.

This 2D linear interpolation for the fluxes are more accurate than 2D interpolation of the torque surface. The torque surface is twisted while the flux surface are mainly dependent only on one current at the time. ψ_{sx} depends mainly on i_{sx} and ψ_{sy} on i_{sy} (see figure 3.11).

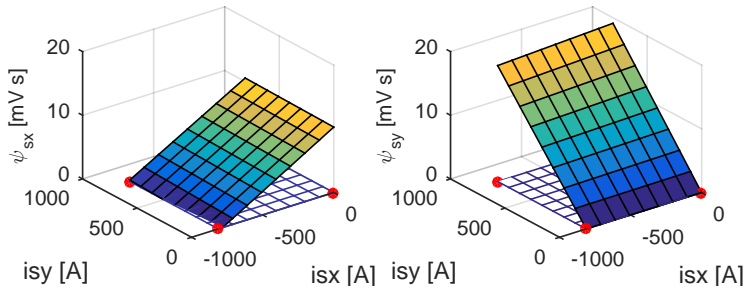


Figure 3.11: Linear interpolation of the flux linkage $[\psi_{sx}, \psi_{sy}]$ for the interior points

3.3.b The nominal torque

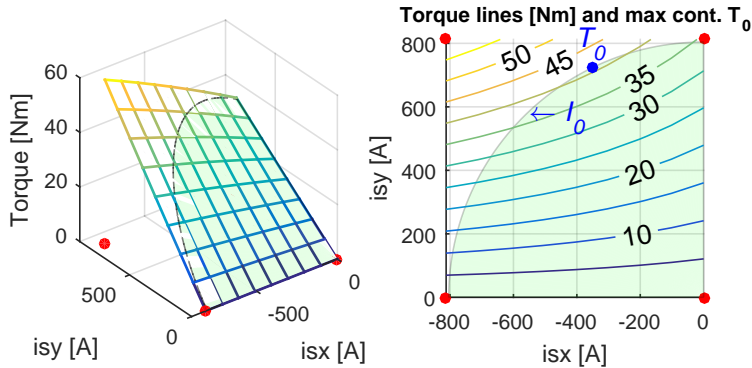


Figure 3.12: The Torque $T = n_{pp} \cdot \vec{\psi} \times \vec{i}$ calculated for the interior points. The nominal torque T_{nom} is found along the circle with radius I_0

The Torque for the interior points is calculated as the cross product of the *flux-linkage* and the current: (eq. 3.4) and (figure 3.12, left)

$$T = n_{pole\ pairs} \cdot \begin{bmatrix} \psi_{sx} \\ \psi_{sy} \end{bmatrix} \times \begin{bmatrix} i_{sx} \\ i_{sy} \end{bmatrix} \quad (3.4)$$

The nominal torque T_{nom} is given by the point on the circle with radius I_0 that has highest torque (see figure 3.12, right) and (table 3.4).

Table 3.4: Nominal current vector

| | | | | | |
|------------------------------------|------------------|---|----------------------------------|-------|------|
| nominal current vector | \vec{i}_0 | = | [-355.4 | 730] | [A] |
| | $ \vec{i}_0 $ | = | | 812 | [A] |
| amplitude of ph. curr. (pow. inv.) | \hat{i}_a | = | $\sqrt{\frac{2}{3}} \vec{i}_0 $ | = 663 | [A] |
| phase curr. rms | $i_{a,rms}$ | = | $\frac{\hat{i}_a}{\sqrt{2}}$ | = 469 | [A] |
| preliminary nominal torque | $T_{nom,prelim}$ | = | | 40.41 | [Nm] |

According to the thermal analysis, the nominal current I_0 is the amount of current that can be applied to the *EM* during unlimited time without reaching temperatures that can harm it. With unlimited time it is meant that a steady state thermal equilibrium has been reached.

3.3.b.1 The nominal flux

The nominal flux $\vec{\psi}_0$, i.e. the flux at the nominal current point $\vec{\psi}(\vec{i}_0)$ is needed to find out the induced voltage and the required *dc-link-voltage* when running at nominal conditions, i.e. at nominal speed ω_0 and applying the nominal current to obtain the nominal torque.

The nominal flux is obtained by interpolating the flux maps ψ_{sx} and ψ_{sy} at the location of the nominal current point, see *table 3.5* and *figure 3.13*.

Table 3.5: Nominal flux vector

| | | | | | |
|---------------------|-------------------------|---|--------|---------|--------|
| flux at \vec{i}_0 | $\vec{\psi}(\vec{i}_0)$ | = | [5.987 | 16.838] | [mV s] |
| nominal flux | $\vec{\psi}_0$ | = | [6.026 | 16.682] | [mV s] |
| | $ \vec{\psi}_0 $ | = | | 17.871 | [mV s] |

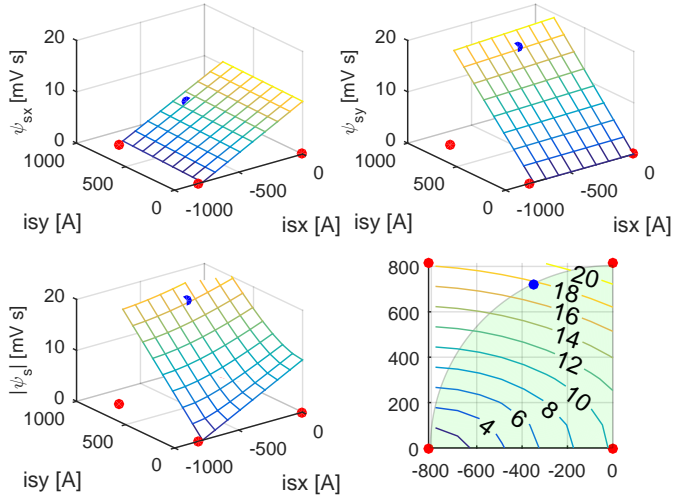


Figure 3.13: The flux linkage $\vec{\psi}_0$ for the nominal current \vec{i}_0

3.3.c The peak torque and peak current

The peak torque T_{peak} is the maximal torque that the *EM* needs to deliver for at least during a short amount of time of a few seconds. For this hybrid topology, for example, the peak torque is mostly needed to start the *ICE* or to synchronize shaft in the gearbox. Therefore it is mostly needed during a few seconds or less each time it is needed.

The relationship between the torque and the applied current is non linear. The torque increases strongly with the current when the iron core is not saturated but for high current values saturation will slow down the gain in torque per extra applied current, see *figure 3.28*.

To avoid magnetic saturation in the iron core of the *EM* it is important to avoid narrow paths in the *teeth* and *yoke* of the stator.

To find out the amount of current that is needed to achieve the peak torque a new set of larger 4 current vectors are analyzed using *RF-Design* and *FEMM*. During the fast optimization process, when it is desired to keep down the number of simulations, this new analysis is done applying twice the nominal current, $I_{peak} \approx 2 \cdot I_0$, considering that the desired peak torque here is twice the nominal torque.

The calculation of the torque for internal points within these 4 current vectors is done using the flux values in the same way as for the nominal torque, see left side on *figure 3.14*. Due to saturation, the values for internal points are not accurate in this preliminary fast optimization.

The peak current I_{peak} is calculated for the $T_{peak} = 90Nm$ which is given in the specifications. The peak current I_{peak} is found by tracing the currents along the constant torque line $T = T_{peak}$ and finding the one that lies closest to the origin, see right side on *figure 3.14*.

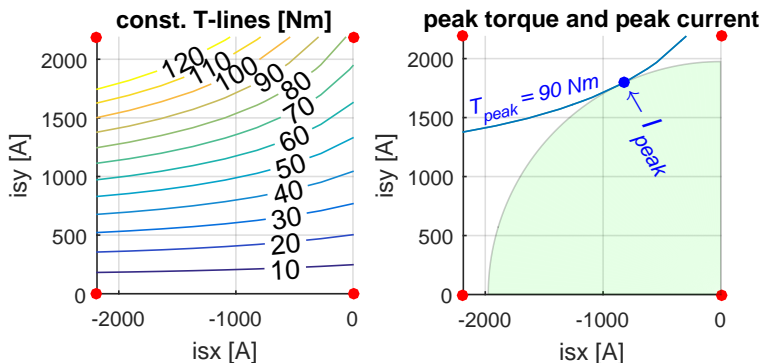


Figure 3.14: The peak current I_{peak} is found by tracing the currents along the constant torque line $T = T_{peak}$ and finding the one that lies closest to the origin

3.3.d The number of winding turns

The number of winding turns is determined considering the available dc-link-voltage or battery voltage, the required nominal speed and the flux linkage at the nominal current, and it is explained in the following lines.

In *figure 3.15* and (eq. 3.5) we can see a basic electric representation of the *iPMSM*. The *iPMSM* is controlled by regulating the voltage applied to the motor $[u_{sx}, u_{sy}]$.

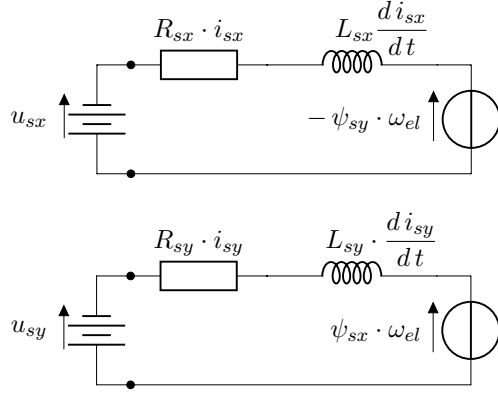


Figure 3.15: Electric representation of the *iPMSM*

$$\begin{aligned}
 u_{sx} &= R \cdot i_{sx} + L_{sx} \frac{di_{sx}}{dt} - \psi_{sy} \cdot \omega_{el} \\
 u_{sy} &= R \cdot i_{sy} + L_{sy} \frac{di_{sy}}{dt} + \psi_{sx} \cdot \omega_{el}
 \end{aligned}
 \tag{3.5}$$

3.3.e Relationship between the dc-link-voltage and the magnitude of the voltage vector $\vec{u}_{s,xy}$

When the *EM* is running at steady state conditions, i.e. constant torque and constant speed, then the voltage and current vectors will appear as stationary points in the rotor *xy*-coordinate system.

In the stator ($\alpha\beta$)-coordinate system, the voltage and current vectors will form circles with radius equal to the magnitude of the vectors in (*xy*)-coordinate system, i.e. no scaling from *xy* to $\alpha\beta$.

$$|\mathbf{u}_\alpha \quad \mathbf{u}_\beta| = |\mathbf{u}_{sx} \quad \mathbf{u}_{sy}| = \sqrt{u_{sx}^2 + u_{sy}^2}$$

In the 3-phase (*abc*)-system the vectors look like 3 sinus waves in a amplitude vs. θ graph, with 120° displacement in the θ direction.

There are two common methods of coordinate transformation between ($\alpha\beta$) to phase (*abc*)-system. The *Power Invariant Transformation* and the *Amplitude Invariant Transformation*. In this thesis only the *Power Invariant Transformation* is used, where there is a scaling factor between the amplitude of the sinusoidal wave representing the phase values over time, for example for the

voltage \hat{u}_a and the magnitude of the vectors in the stator or coordinate system $|\vec{u}_s|$.

$$\hat{u}_a = \sqrt{\frac{2}{3}} \cdot \begin{vmatrix} u_{sx} \\ u_{sy} \end{vmatrix} \quad (\text{Power Invariant Transformation}) \quad (3.6)$$

Depending on the PWM-modulation, eventually a *zero-sequence* may be added to the 3-phase voltages, i.e. the all 3 waves are increased or decreased by the same value v_0 maintaining the voltage difference u between phases but changing their voltage potentials v :

$$v_a = u_a + v_0$$

$$v_b = u_b + v_0$$

$$v_c = u_c + v_0$$

The required dc-link voltage depends on the type of PWM-modulation: *sinusoidal*, *symmetric*, *bus clamped* ([5] eq. 2.29 yellow book).

$$\begin{aligned} \text{sinusoidal modulation:} \quad u_{dc,min,(sin)} &= 2 \hat{u}_a \\ \text{symmetric:} \quad u_{dc,min,(sym)} &= \sqrt{3} \hat{u}_a \\ \text{bus clamped modulation:} \quad u_{dc,min,(busc)} &= \sqrt{3} \hat{u}_a \end{aligned} \quad (3.7)$$

Using the *Symmetric PWM-Modulation* and with the Power Invariant Factor in (eq. 3.6) and for the moment no safety marginal considered, we have:

$$u_{dc,min} = \sqrt{3} \sqrt{\frac{2}{3}} \begin{vmatrix} u_{sx} \\ u_{sy} \end{vmatrix} = \sqrt{2} \begin{vmatrix} u_{sx} \\ u_{sy} \end{vmatrix} \quad (3.8)$$

3.3.f The induced voltage \vec{e} and required dc-link voltage u_{dc}

Considering the circuit in (fig. 3.15) and (eq. 3.5), we can see that the last term, the induced voltage \vec{e} .

$$\vec{e} = \omega_{el} \begin{bmatrix} 0 & -1 \\ 1 & 0 \end{bmatrix} \vec{\psi} = \omega_{el} \begin{bmatrix} -\psi_{sy} \\ \psi_{sx} \end{bmatrix}$$

is the one that most depends on the speed and its magnitude $|\vec{e}_0|$ at the *nominal current vector* \vec{i}_0 and at the nominal electric speed $\omega_{0,elec}$

$$|\vec{e}_0| = \omega_{0,elec} \cdot |\vec{\psi}_0| \quad (3.9)$$

is presented in (table 3.6).

The necessary dc-link voltage to be able to handle at least the induced voltage is similar to (eq. 3.8)

$$U_{dc,min} = \sqrt{2} |\vec{e}_0| \quad (3.10)$$

And an extra margin is added to handle the resistive and inductive voltage drop.

The values of $|\vec{e}_0|$ and $U_{dc,min}$ for one winding turn, using the Power Invariant Transformation and Sinusoidal PWM modulation are presented in (table 3.6)

Table 3.6: The nominal induced voltage per turn

| | | | | |
|-------------------|---|---------|---------|------------------|
| $ \vec{\psi}_0 $ | = | 17.871 | [mV s] | (table 3.5) |
| $\omega_{0,elec}$ | = | 1333.33 | [rad/s] | (table 3.3) |
| $ \vec{e}_0 $ | = | 23.828 | [V] | per winding turn |
| $U_{dc,min}$ | = | 33.698 | [V] | per winding turn |

3.3.g Number of winding turns n_{wind}

In the Finite Element Model the slot is considered as if it is composed of a single conductor. In the real EM there are many conductors which can be arranged in parallel or in series. The series arrangement in a certain number of winding turns makes possible to reduce the amount of required current supplied to the phases at the expense of increasing the required voltage.

Considering that the available battery voltage

$$U_{dc,batt} = 300[V]$$

is many times the required dc-link voltage for one turn (table 3.6)

$$U_{dc,min} = 33.7[V] \text{ per winding turn}$$

the number of $n_{wind} = 8$ winding turns for the conductors in the stator is considered appropriate:

This will reduce the current values by a factor of 8 and increase the voltage values by the same factor 8, see (table 3.7)

Table 3.7: Number of winding turns

| | | | | |
|-----------------|-------------------------|----|-----------|-------------|
| | $U_{dc,batt}$ | = | 300 [V] | (eq. 2.11) |
| | $U_{dc,min,(1\ turn)}$ | = | 33.7 [V] | (table 3.6) |
| \implies | n_{wind} | := | 8 | |
| | $U_{dc,min,(8\ turns)}$ | = | 269.6 [V] | |
| phase curr. rms | $i_{a,rms,1\ turn}$ | = | 469 [A] | |
| | $i_{a,rms,8\ turns}$ | = | 59 [A] | |

The new dc-link voltage needed for the induced voltage

$$U_{dc,min(8\ turns)} = n_{wind} \cdot U_{dc,min(1\ turn)} = 269.6 [V]$$

leaves a good margin for the resistive and inductive voltage drops.

3.3.h Top speed and field weakening

In order to be able to run the *iPMSM* over the nominal angular speed $\omega > \omega_0$ without increasing the required dc-link voltage the magnitude of the flux linkage $|\vec{\psi}|$ need to be reduced

$$U_{dc} \approx |\vec{e}| = \underset{\uparrow}{\omega} \cdot \underset{\downarrow}{|\vec{\psi}|} = constant \quad (3.11)$$

The magnitude of the flux linkage $|\vec{\psi}|$ can be reduced by electrically creating a magnetic field opposite to the field of the magnets to partially or totally neutralize them. This process is called **field weakening** [25] [26] and [5]. As we can see on (figure 3.16) the flux linkage $|\vec{\psi}|$ is reduced to 0 when \vec{i}_{demag} is applied. This should not be confused with demagnetization of the permanent magnets.

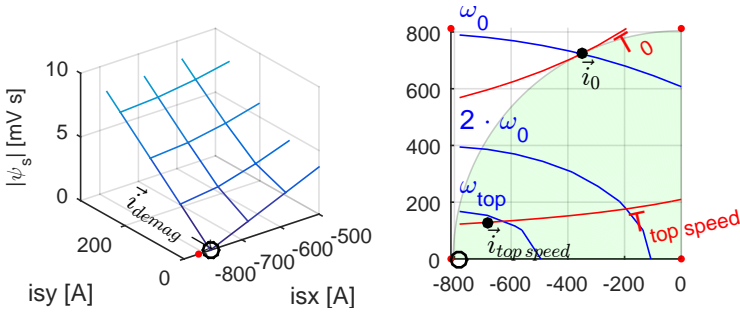


Figure 3.16: The demagnetization point \vec{i}_{demag} where $|\vec{\psi}_{demag}| = 0$. The current is moved towards this point to be able to run the EM above nominal speed

Reducing the flux linkage reduces the torque but the *EM* can run faster. *Field weakening* can be considered as a kind of "electromagnetic gear box"

The relation between the top speed ω_{top} and the nominal speed ω_0 is called the field weakening ratio

$$k_{field\ weakening} = \frac{\omega_{top}}{\omega_0} = \frac{speed_{top}}{speed_0}$$

For this EM the field weakening ratio according to the speed specifications in (table 3.1) is

$$k_{field\ weakening}^* = \frac{15000 [rpm]}{3183 [rpm]} = 4.71$$

The current $\vec{i}_{top\ speed}$ used to reach the required top speed should:

- lie within the circle with radius I_0 to avoid overheating.

$$|\vec{i}_{top\ speed}| < |\vec{i}_0|$$

- lie close enough to the demagnetization point so that the flux linkage is reduced proportionally to the field-weakening ratio:

$$|\vec{\psi}_{top\ speed}| < \frac{\omega_0}{\omega_{top}} \cdot |\vec{\psi}_0|$$

- create a enough torque that the nominal power is maintained over the whole speed range.

$$|T_{top\ speed}| \cdot \omega_{top} > |T_{nom}| \cdot \omega_0 = P_{nom}$$

The position of the *demagnetization point* \vec{i}_{demag} plays a crucial roll in the capability of the EM to reach top speed and also affects the torque.

This position will depend on the balance between the capabilities of the rotor vs. the ones of the stator. An EM with strong magnets, large rotor diameter, which implicate little remaining space in the stator for the copper windings will create an strong EM which is difficult to demagnetize. The *demagnetization point* will move to the left on the negative x-axis, i.e. large current will be needed to demagnetize, i.e. a quite strong EM but with low top speed.

On the other hand if the EM has less powerful magnets and the stator is predominant compared to the rotor the EM will produce in general less torque for the same current than the previous alternative. On the other hand, the weaker the magnets the easy to demagnetize them by the large stator, that creates a weak EM but with high top speed. The *demagnetization point* will move to the right on the negative x-axis, i.e. towards the origin, i.e. $\vec{i} = [0, 0]$

The over-speed capabilities of a certain EM design depend on the position of \vec{i}_{demag} in relation to the continuous current I_0 .

The optimal location for the demagnetization point is a bit to the left of the point $[-I_0, 0]$ so that $\vec{i}_{top\ speed}$ will land exactly on the continuous current circle.

In this project, considering that the field weakening ratio is quite large, about 5 times, which will mean that $\vec{i}_{top\ speed}$ will be very close to \vec{i}_{demag} :

$$|\vec{i}_{top\ speed} - \vec{i}_{demag}| \approx \frac{1}{5} |\vec{i}_0 - \vec{i}_{demag}|$$

a simplification is done in the fast optimization stage : The *demagnetization current vector* \vec{i}_{demag} is 'forced' to move towards $[-I_0, 0]$.

$$\vec{i}_{demag} \rightarrow [-I_0, 0]$$

By knowing the appropriate location of the demagnetization point \vec{i}_{demag} , computation time can be saved in the post processing. In this way a torque-speed-diagrams are not necessary after every *FEA* to see if the field weakening ratio is reached.

3.4 Strategy to reduce the number of simulations and the whole optimization time

Specially the electromagnetic *FEA*, where a set of currents points and different angular positions need to be tested, is very time consuming, it can take days if not weeks for the design of an *EM*.

The time it takes can vary a lot depending of many factors as the number of mesh points, the complexity of the geometry, desired precision, etc. But, as an example, the time needed to perform electromagnetic *FEAs* for the geometries in this thesis, using an up to date personal computer by the time of writing the thesis, around year 2015, is as follows:

To run an electromagnetic *FEA*, on only one pole sector of the *EM* (figure 3.8), for a single static operation point, takes ca 8 seconds.

To run the same *FEA* for the whole *EM* (figure 3.18) takes ca. 60 seconds. The second geometry is also more detailed around the magnets.

For every geometry, a set of current vectors are analyzed to find out the torque and flux-linkage maps on the i_{sx}, i_{sy} - *plane*, a set of 4×6 current vectors are for ex. analyzed. But in the preliminary fats optimization only 2×2 current points are analyzed.

For every current a set of different angular positions θ of the rotor are analyzed to find out the average torque and the ripple. Here a total of 36 positions were analyzed, 180°_{elec} in steps of 5°_{elec} but they could be reduced to a third, because the ripple pattern is repeated for every slot.

To obtain the data to characterize a certain design, for.ex. the data in (figure 3.21) takes at least:

- 1 minute for one single static operation point
- $24 = 4 \times 6$ current points \vec{i}_s
- 36 angular positions θ

$$t_{FEA} = 1 \times 24 \times 36 = 864 [minutes]$$

And every geometry depends on a set of ca 20 variables. Finding appropriate simplifications and applying better optimization methods can help to save a huge amount of computational time.

Therefore for example in the preliminary optimization only a pole and only 4 current points are calculated for every parameter configuration (figure 3.10). other strategies to reduce the number of *FEAs* are described in the follow lines.

3.4.a Optimization criteria for the next iteration

From the thermal *FEA* the nominal current \mathbf{I}_0 at the predefined cooling conditions is obtained.

And from the electromagnetic *FEA* the nominal torque T_{nom} , peak torque T_{peak} and the position of the demagnetization point $-\vec{i}_{demag}$ are obtained. This values should be analyzed according to the following criteria:

- **The nominal torque:** The torque T_{nom} along the circle with radius \mathbf{I}_0 on the $i_{s,xy}$ -plane should be maximized in the following iterations until $T_{EM,nominal}$ is reached.
- **The peak torque:**

As it will be explained more in detail later (subsection 3.5.c), at low currents the components of the flux linkage increase linearly with the respective current components (equation 3.13). But for high current values the iron core becomes saturated and the components of the flux linkage begin to flatten as consequently the torque does not longer increase with current as it would do with unsaturated iron.

A basic way to ensure that the magnetic saturation is avoided is to compare the values of $\vec{\psi}_{sx}(\vec{i}_{peak})$ with its hypothetic unsaturated values, i.e. using (equation 3.13).

Considering the limited available simulated data at this optimization stage, the inductances and ψ_m , can be approximated to:

$$\begin{aligned}
 L_{sx} &\approx \frac{\Delta\psi_{sx}}{\Delta i_{sx}} = \frac{\psi_{sx}(0, 0) - \psi_{sx}(-i_0, 0)}{0 - (-i_0)} \\
 L_{sy} &\approx \frac{\Delta\psi_{sy}}{\Delta i_{sy}} = \frac{\psi_{sy}(0, i_0) - 0}{i_0 - 0} \\
 \psi_m &= \psi_{sx} \left(\begin{bmatrix} 0 \\ 0 \end{bmatrix} \right)
 \end{aligned} \tag{3.12}$$

- **Top speed capabilities:** the demagnetization point on the $i_{s,xy}$ -plane should lie close enough to the circle with nominal current I_0 on the negative x-axis. I.e. close enough to the point $[-I_0, 0]$ so that the *iPMSM* can be go on field weakening with nominal current reaching the specified top speed, for.ex. here $speed_{EM,top} = 15000 [rpm]$.

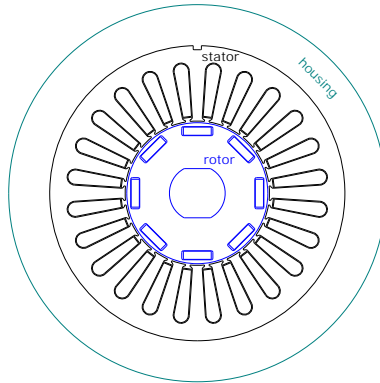
Based on the last and previous results a new parameter sets are chosen (section 3.2.a) and a new thermal and electromagnetic *FEAs* are performed with the new geometry.

3.5 Finite Element Analysis of the final geometry

Based on the results of the optimization process the final geometry of the *iPMSM* for manufacturing the prototype is created using the *CAD* software *Pro-Engineer*.

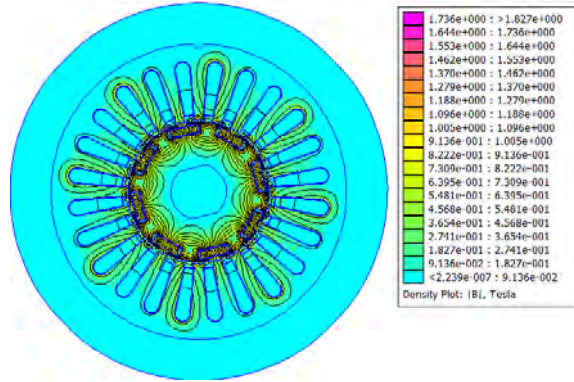
In the *CAD* drawings, the geometry is adapted for the manufacturing process of the prototype and for mechanical loads and stresses in the materials. Specially sharp corners are rounded and mounting and manufactured tolerances are included as for ex. *air pockets* around the magnets. (see figure 3.17)

Figure 3.17: Final geometry of the EM



The geometry created in the *CAD* software is exported in *DXF* format and imported to *FEMM*. The corresponding material properties are set to the different regions and a new *FEA* are performed on the final geometry of the *EM*. (see fig 3.18)

Figure 3.18: Electromagnetic FEA of the final geometry



3.5.a Torque and flux maps on the current i_{sx}, i_{sy} -plane

A set of $30\theta \times 4i_{isx} \times 6i_{isy} = 720$ FEA simulations are performed. As mentioned before, it takes about 12 hours computation time for this more complex and realistic geometry.

In total 4 different geometries are investigated, simulated and manufactured for cogging torque reduction. The stator is the same but with 4 rotor configurations, more about that in sections 3.6.a and 3.6.b.

For each of the 4×6 current vectors $[i_{sx}, i_{sy}]$ at each angular position, the corresponding phase currents i_a, i_b, i_c are calculated, see figure 3.19.

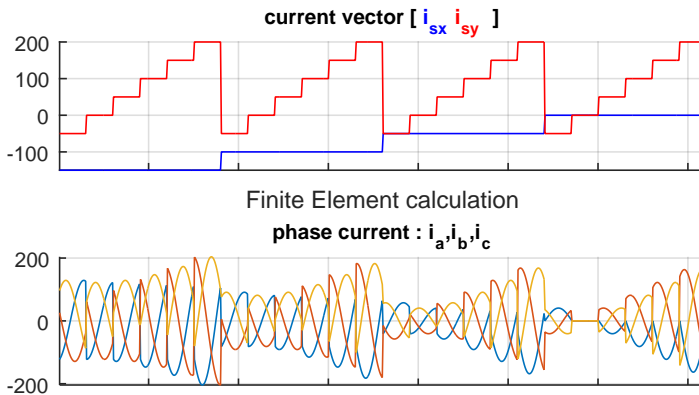


Figure 3.19: The current vectors at which the flux will be calculated are transformed to phase current values for the FEA in total $30\theta \times 4i_{isx} \times 6i_{isy} = 720$ simulations

These values are assigned using *lua*-script to the corresponding coils in the *FEA*-model in *FEMM* after having been multiplied by the number of winding turns $n_{wind} = 8$.

The output of the FEA is a text file containing the rotor angle θ , the 3 phase currents i_a, i_b, i_c , 3 phase fluxes ψ_a, ψ_b, ψ_c , 3 resistive voltages drop v_a, v_b, v_c (not used in this project) and 1 torque value $T_{FEMM,em}$.

From the 3 phase fluxes ψ_a, ψ_b, ψ_c the corresponding flux vectors $[\psi_{sx} \ \psi_{sy}]$ are calculated in Matlab, (see fig 3.20)

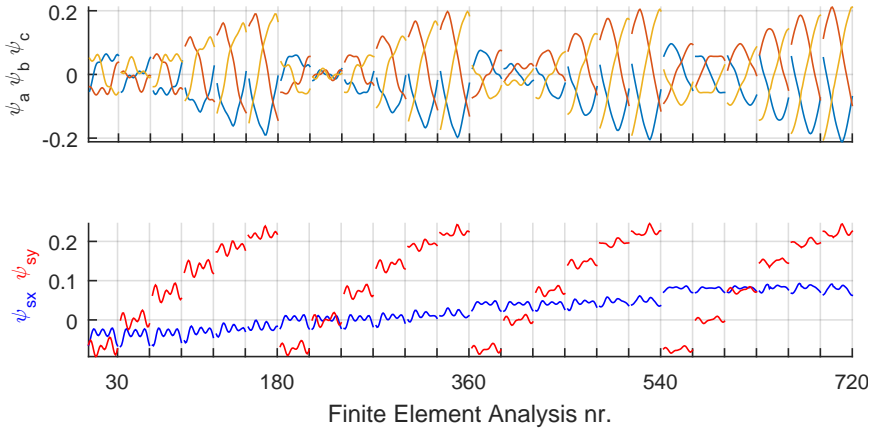


Figure 3.20: Computation of the flux $\vec{\psi}$ at $30 \theta \times 4 i_{isx} \times 6 i_{isy} = 720$ simulations, ca. 12 hours, for one rotor

These 30 vector fields, one for every θ , of $[\psi_{sx} \ \psi_{sy}] = f([i_{sx} \ i_{isy}])$ rearranged in matrix form on the $[i_{sx} \ i_{isy}]$ plane are shown in (figure 3.21)

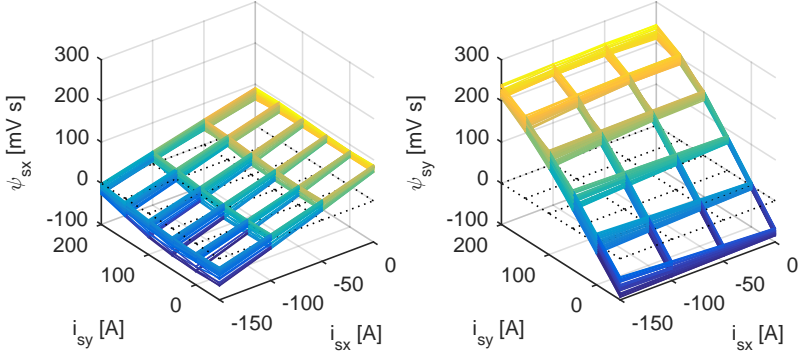


Figure 3.21: Mesh with the flux vector $[\psi_{sx}, \psi_{sy}]$ at 4 i_{sx} , 6 i_{sy} and 30 θ

In (figure 3.22) we can see the average over θ of the flux $\vec{\psi}$.

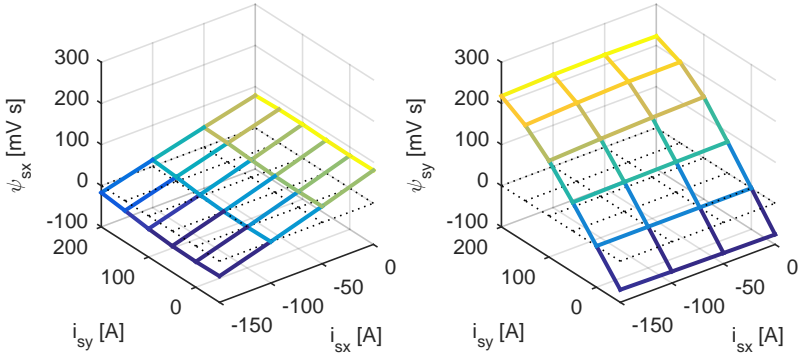


Figure 3.22: Mesh with the flux vector $[\psi_{sx}, \psi_{sy}]$ at 4 i_{sx} , 6 i_{sy} and average over θ

3.5.b The torque-speed diagram

From this new simplified mesh the contour lines for different torque values are calculated. Specially the contour line for $T_{nom} = 45[Nm]$ and the point \vec{i}_0 , as the point along this contour line that lies closest to the origin i.e. lowest amount of current. (see the black torque lines in fig 3.23)

In a similar way the contour lines for different magnitudes of the flux $|\vec{\psi}|$ are calculated. According to (eq. 3.11) each contour line for a given magnitude of the flux $|\vec{\psi}|$ corresponds to certain speed.

At the point \vec{i}_0 it is desired to be able to run at the nominal speed ω_0 which

corresponds to $speed = 3180[rpm]$ (table 3.1) and to the electric angular speed $\omega_{0,elec}$ (table 3.3).

For a given dc-link voltage, every constant flux ellipse corresponds to a certain speed, where the nominal flux $|\vec{\psi}_{nom}|$ corresponds to the nominal speed ω_{nom} . The nominal flux is the flux at the nominal current point $|\vec{\psi}_0|$. The flux is inverse proportional to the speed for constant induced voltage e :

$$e = |\vec{\psi}| \cdot \omega_{elec}$$

Field weakening operation is applied for speeds above the nominal one. The corresponding speeds are assigned to each flux value (orange lines in figure 3.23).

In (figure 3.23), on each *iso-torque* line four points are identified. The flux values and the corresponding speeds for these 4 points are calculated:

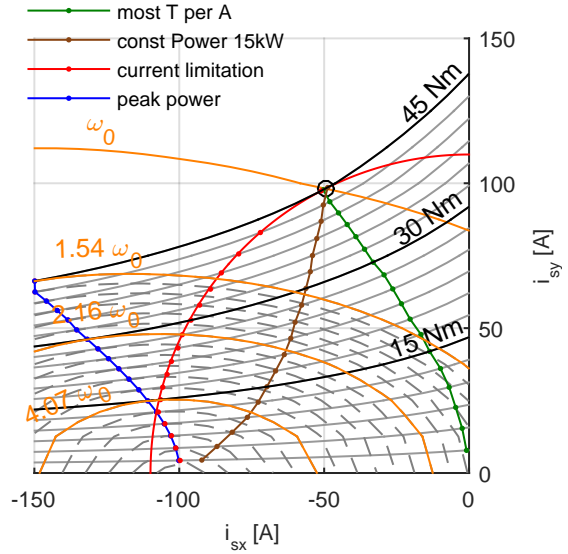
1. **Max Torque Per Amp:** Point on a given *iso-torque* line that lies closest to the origin, i.e produces the torque with lowest current i.e. lowest *Cu-losses* [27].

2. **Nominal power:**

$$P_{nom} = T_{nom} \cdot \omega_0 = 15 [kW]$$

3. **Nominal Current limitation:** Maximal magnitude of the current under continuous operation to avoid overheating. Assuming that the cooling system will be dimensioned to be able to handle the nominal current $|\vec{i}_0|$
4. **Peak power** Highest possible speed at the given torque level. This point is found by looking after the point with lowest flux on the studied torque line.

Figure 3.23: Torque and speed contour lines in the $[i_{sx} \ i_{sy}]$ -plane. The maximal reachable speeds under 4 different conditions.

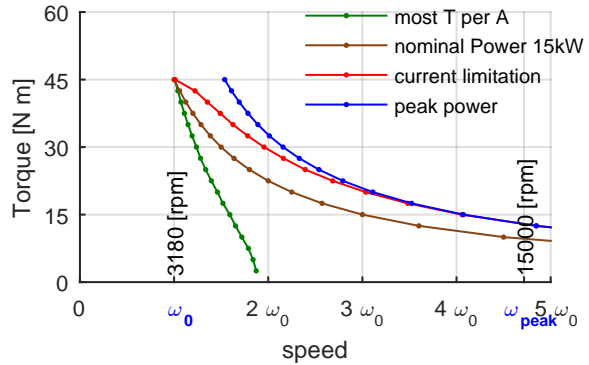


Each point on the $[i_{sx} \ i_{sy}]$ -plane shown in (figure 3.23) where torque lines are curves crossing speed or flux ellipses have a corresponding point in the *torque-speed diagram* or $T - \omega$ -*diagram* where each torque line is represented as horizontal line and every speed line as a vertical line in a *Cartesian coordinate system* (figure 3.24).

On (figure 3.24) we can see that the speeds required for sustained *constant power* (black line) are lower than the speeds that can be reached within the *current limitation* (red line). This means that the *iPMSM* can not only maintain the specified power of $P = 15\text{kW}$ over the entire speed range without being overheated, but even deliver higher power.

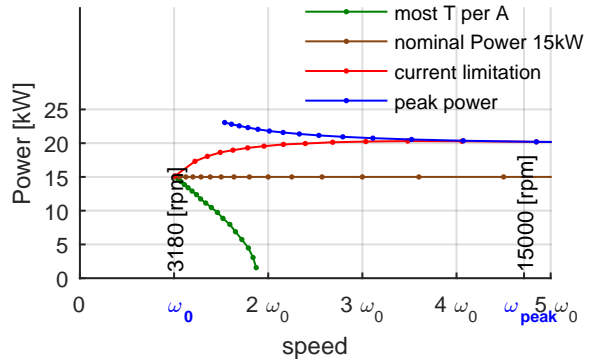
A more detailed description of the creation of the *Speed-Torque diagrams*, with further information about the *iPMSM*, is presented in (chapter 6) with the actual measured data from the prototype.

Figure 3.24: Maximal possible speed as a function of torque under 4 different conditions



From the speed torque relations under the 4 different conditions the maximal power is calculated, (see figure 3.25). The *iPMSM* designed to deliver nominal power at nominal torque can deliver more power at higher speeds than the nominal speed ω_{nom} .

Figure 3.25: Maximal power as a function of speed under the 4 different conditions



The performance of the *iPMSM* is further studied in (section 6.2) using measured data, specially the peak power needed for fast synchronization of the shafts in the gearbox.

3.5.c Extended Torque capabilities and saturation

For an ideal iron core, i.e. an iron core that does not become saturated, the maximal torque for a certain current magnitude would increase in a quasi quadratic way, specially for large current values.

$$T_{max}(|\vec{i}_s|) \approx k \cdot |\vec{i}_s|^2$$

This ideal iron core would have constant inductances \mathbf{L}_{sx} and \mathbf{L}_{sy} , that would remain unchanged even for high applied current and at high flux density, and the flux-linkage would be a first degree function of the current (equation 3.13) [5] :

$$\begin{aligned} \text{with: } \psi_{sx} &= \psi_m + L_{sx} \cdot i_{sx} \\ \psi_{sy} &= L_{sy} \cdot i_{sy} \end{aligned} \quad (3.13)$$

The current point $[i_{sx}^*, i_{sy}^*]$ among all current points forming a circle with radius $|\vec{i}_s|$ that produces the highest torque, considering constant inductances, can be calculated according to (equations 3.14) [28, p. 80] :

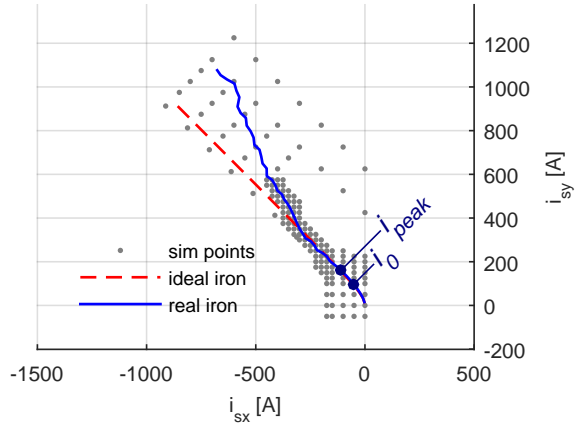
$$\begin{aligned} i_{sx}^* &= \frac{-\psi_m + \sqrt{\psi_m^2 + 8(L_{sx} - L_{sy})^2 |\vec{i}_s|^2}}{4(L_{sx} - L_{sy})} \\ i_{sy}^* &= \sqrt{|\vec{i}_s|^2 - i_{sx}^{*2}} \end{aligned} \quad (3.14)$$

The torque T (see equation 3.15) would be, in this ideal case, a second degree function of the current.

$$T = n_{pole\ pairs} \cdot \vec{\psi}_s \times \vec{i}_s \quad (3.15)$$

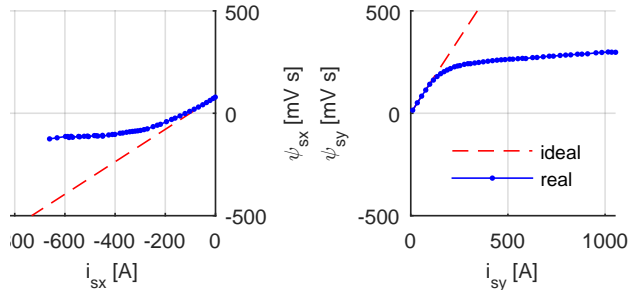
In (figure 3.26) we can see the path for max torque for given current amplitude for the ideal iron and the realistic iron for current values up to ca 10 times the peak current.

Figure 3.26: Optimal current for Torque beyond T_{peak}



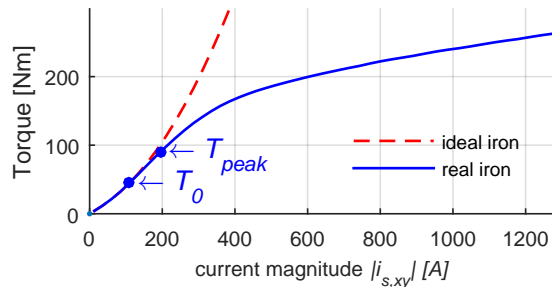
For the real iron core, i.e. one that becomes saturated at high flux densities, the components of the flux-linkage ψ_{sx} and ψ_{sy} increase almost linearly with the current for low current values but then they flatten for large currents (figure 3.27).

Figure 3.27: Flux linkage for high current values



The torque then no longer increases quadratically with the current for high current values. (see figure 3.28)

Figure 3.28: Torque for high current values



3.6 Different rotor configurations to reduce cogging

Cogging is a ripple in the electromagnetic properties of the *iPMSM* during the rotation of the rotor which repeats periodically depending on the number of permanent magnet poles along the circumference of the rotor and the number of teeth on the stator.

The magnetic flux-linkage and the reluctance are different when the magnet is in front of an iron tooth than when the magnet is in front of a copper slot. The magnets tend to get stuck to the iron teeth, then a large current or external torque is needed to overcome this cogging torque to start the *iPMSM*. This cogging torque is most noticeable at start and at low speeds, but even at high speeds this cogging produces oscillations in the current, voltage and torque.

There are different strategies to reduce cogging the two following ones are studied in this project:

- Asymmetric placement of the magnets in the tangential direction so that not all of them approach or leave the stator iron teeth at the same time.
- Utilization of the non symmetry in the magnetization of the magnets, the so called *hot- and cold-side effect*

Other strategies to reduce the cogging are, skewing the stator, rearranging the winding configuration and placing the magnets in v-shaped position [29] [30].

note: Cogging, or ripples in the torque, flux, current and voltage can also be produced by the non ideal properties of the *PEC* as the effect of *blanking time* which produces an irregularity in the actual applied voltage every 60 electric degrees. This effect is not further studied in this thesis but should be mentioned because its effects are very similar than the ripples caused by the geometry of the *iPMSM*.

note 2: The *cogging current ripple* here is different than the *switching current ripple* caused by the *PWM* in the *PEC*. The *cogging current ripple* is related to the geometry and has a frequency of a multiple of the electric frequency at which the *iPMSM* is running, while the frequency of the *switching current ripple* is a multiple of switching frequency f_{sw} which is much higher for ex. ca 10 [kHz].

3.6.a Symmetric and asymmetric placing of the magnets to reduce cogging

In this *iPMSM* there is 24 slots in the stator, i.e. there is an iron tooth every 15°_{mech} and the *iPMSM* has 4 pairs of permanent magnet poles along the circumference of the rotor. In the rotational symmetric magnet placement the magnets are evenly placed every 45°_{mech} . In the asymmetric one the magnets are displaced from this neutral position to different multiples of $\frac{15^\circ_{mech}}{4}$ (see figure 3.29 and 3.30):

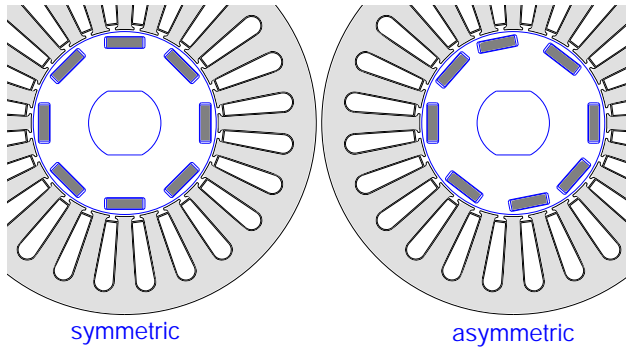


Figure 3.29: Rotational symmetric and asymmetric placement of the magnets. The second one produces a smoother rotation by preventing that the magnets come close to the iron teeth at the same time



Figure 3.30: In the asymmetric rotor the magnets are displaced 0,2,3 and 1 time the angle between 2 iron tooth divided by 4, i.e. $15^\circ_{mech}/4$.

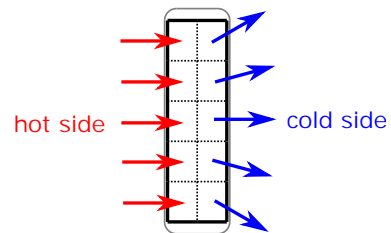
FEAs of the *iPMSM* with *symmetric* and *asymmetric* rotor configurations show a substantial reduction of the torque ripple for the *asymmetric* geometry. At

the same time the average torque per current unit is also reduced, i.e. more current need to be applied to produce the same torque. (see figure 3.32)

3.6.b The '*hot side, cold side*' effect caused by non symmetric magnetic field in the magnets

According to the manufacturer of the permanent magnets *Vacuumschmelze GmbH*, on one side of the magnets the magnetic flux is parallel to the main magnetization direction and on the other side it either spreads out or is collected depending on the flow direction (see figure 3.31). The side where the flow is parallel is called the '*hot-side*' and the other is called the '*cold-side*'.

Figure 3.31: Sketch of the hot-cold-side property of the magnets



This effect has its origin in the manufacturing and magnetization process of the magnet. The magnetic field created for the magnetization is not fully parallel, in the most internal part the flow is more parallel than on the external side, and this pattern remains in the magnets.

This property of the magnets can be used to affect the properties of the *iPMSM*, specially placing the cold side out can reduce cogging. This effect is studied as well in this project.

3.6.c Comparison between four different rotors designs

To analyze the effects of symmetry vs asymmetry and the effects of placing the hot-side resp. the cold-side of the magnet towards the outside of the rotor, in radial direction, a set of four rotors are designed, simulated and manufactured:

- one symmetric rotor with the hot-side out
- one symmetric rotor with the cold-side out
- one asymmetric rotor with the hot-side out
- one asymmetric rotor with the cold-side out

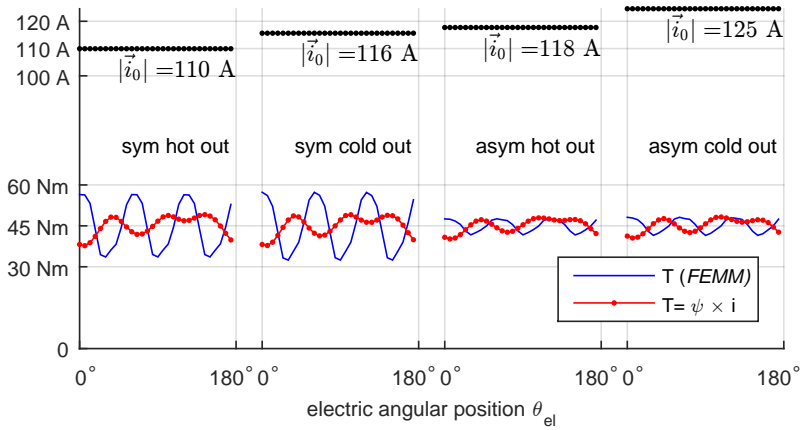


Figure 3.32: comparison between the four rotors at the nominal torque $T_{nom} = 45 \text{ Nm}$. Different amounts of current are required to produce T_{nom} . The figure also shows the variation of the torque depending on the rotor angular position i.e. *cogging*.

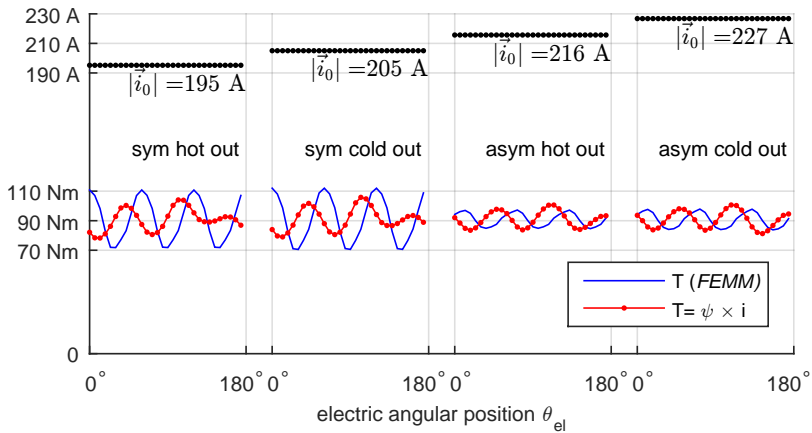
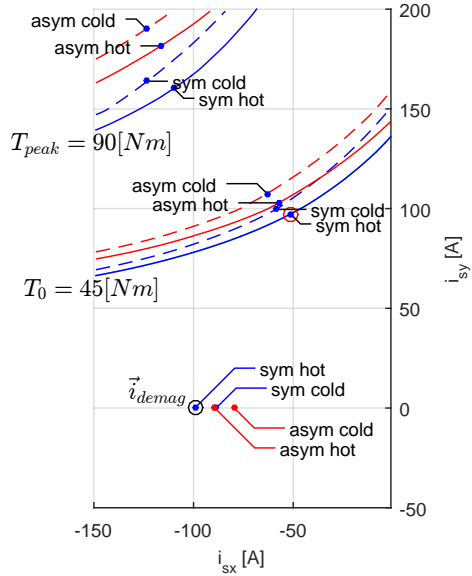


Figure 3.33: Comparison between the four rotors at the peak torque $T_{peak} = 90 \text{ Nm}$ showing the needed amount of current and the torque ripple.

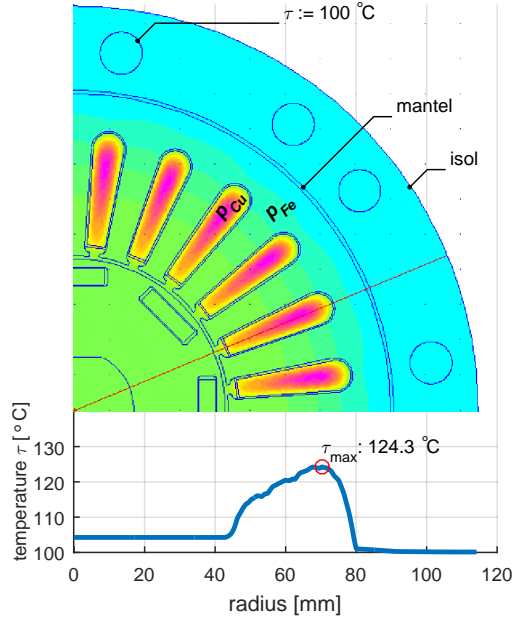
Figure 3.34: Location of the current vectors for nominal Torque, peak Torque and demagnetization on the i_{sx}, i_{sy} plane for the four rotor types



3.7 Thermal analysis of the final design

A finite element steady state thermal analysis is performed on the final geometry of the EM mainly in order to ensure that the recommended temperature limitations for different components of the EM are not exceeded.

Figure 3.35: Temperature distribution along a radial line. load: T_{nom}, ω_0



The heat transfer problem for the EM is modeled (see figure 3.35) assuming:

- resistive heat generation in the slots P_{Cu}
- magnetic hysteresis heat generation in the stator core P_{Fe}
- constant temperature in the cooling channels $\tau_{set} = 100^\circ C$
- thin air layer in the mantel between the stator core and the aluminum housing
- isolation on the outer side of the housing

3.7.a The resistive heat generation P_{Cu}

The resistive heat generation P_{Cu} at $120^\circ C$, for the nominal current $|\vec{i}_0|$ is calculated according (equations 3.16 and 3.17) (similar to eq 3.16 in [31]), and is fed as volume specific heat generation $[W/m^3]$, into the slots to the *FEMM* thermal model. The values used in the calculations are displayed in (tables 3.8, 3.11 and 3.9)

$$P_{Cu} = R \cdot I_{rms}^2 = \frac{len}{A_{Cu}} \rho \cdot I_{rms}^2 \quad (3.16)$$

The geometric values for the first factor $\frac{len}{A_{Cu}}$ are presented in (table 3.8)

Table 3.8: Geometric data for the slots

| | | | | | |
|---------------------|------------------------------------|---|-----|-----------------|-----------|
| insulated slot area | A_{slot} | = | 226 | mm ² | FEMM |
| fill factor | k_f | = | 0.5 | 1 | estimated |
| area of Cu in slot | $A_{Cu,slot} = k_f \cdot A_{slot}$ | = | 113 | mm ² | |
| active length of EM | len | = | 200 | mm | CAD |

The resistivity at the critical temperature $\tau_{critic} = 120^\circ C$ is presented in (table 3.9)

$$\rho(\tau) = \rho_{20^\circ C} \cdot (1 + k_\rho(\tau - 20^\circ C)) \quad (3.17)$$

Table 3.9: Resistivity

| | | | | |
|----------------------|----------------------|---|-----------------------|------------------|
| critical temperature | τ_{critic} | = | 120 | °C |
| resistivity | $\rho_{20^\circ C}$ | = | 16.8 | nΩ m |
| temperature coef. | k_ρ | = | $3.862 \cdot 10^{-3}$ | °C ⁻¹ |
| | $\rho_{120^\circ C}$ | = | 23.3 | nΩ m |

The slot resistance

$$R_{slot,120^\circ C} = \frac{len}{A_{Cu,slot}} \rho_{120^\circ C}$$

and the total phase resistance

$$R_{EM,120^\circ C} = n_{pole\ pairs} \cdot n_{wind}^2 \cdot R_{slot,120^\circ C}$$

are presented in (table 3.10)

Table 3.10: Resistance values, excluding end turns and connection cables

| | | | | |
|-------------------------|------------------------|---|---------------|----|
| equivalent slot res. | $R_{slot,120^\circ C}$ | = | 41.239 | μΩ |
| total phase R at 120° C | $R_{EM,120^\circ C}$ | = | 21.114 | mΩ |
| total phase R at 20° C | $R_{EM,20^\circ C}$ | = | 15.224 | mΩ |

The continuous nominal current through the slot is presented in (table 3.11)

Table 3.11: Values for the applied current

| | | | | |
|-----------------------------|---|---|-------|-------|
| magnitude of current vector | $ \vec{i}_{s,xy} $ | = | 109.9 | A |
| phase current amplitude | $\hat{i}_a = \sqrt{2/3} \vec{i}_{s,xy} $ | = | 89.7 | A |
| rms of phase current | $I_{ph,rms} = \hat{i}_a / \sqrt{2}$ | = | 63.4 | A |
| nr. turns per phase cable | n_{wind} | = | 8 | turns |
| rms curr. per slot | $I_{slot} = n_{wind} \cdot I_{ph,rms}$ | = | 507.4 | A |

The resistive heat generation in a slot

$$P_{Cu,slot} = R_{slot,120^\circ C} \cdot I_{slot}^2$$

and the *volume specific resistive heat generation*

$$p_{Cu} = \frac{P_{Cu,slot}}{A_{slot} \cdot len}$$

that is assigned to the every slots area in the thermal Finite Element Analysis are presented in (table 3.12)

Table 3.12: Resistive heat generation

| | | | | |
|----------------------------|---------------|---|------------|----------|
| res. heat gen. in slot | $P_{Cu,slot}$ | = | 10.59 | W |
| volume spec. res. heat gen | p_{Cu} | = | 234 | kW/m^3 |
| number of slots | n_{slots} | = | 24 | slots |
| total res. heat gen | $P_{Cu,EM}$ | = | 254 | W |

The resistive heat generation in the end turns is not considered in the calculations. This in order to keep the simplicity of the 2D *FEA*. The heat generated in the end turns is assumed to dissipate to the surrounding air, and do not affect the heat transfer in the active length of the *EM*. This is just a simply assumption, certainly there is some heat flow in the axial direction, but this is not supported by the used 2D model.

3.7.b Magnetic hysteresis heat generation on the iron core

Oscillations on the magnetic field on the iron core of the stator and the rotor generate heat due to *eddy currents*. This heat, often called *iron losses*, *Fe-losses* or P_{Fe} , depends on the electric frequency and the magnitude of the flux. To reduce *eddy currents* thin *electromagnetic steel sheets* are used. The prototype

in this thesis is built using (*M250-35A*) sheets and its properties are specified by the manufacturer as the volume specific heat generation as a function of the flux density B and the electric frequency f_{elec} , [32] (see appendix D).

$$\frac{P_{Fe}}{mass} : table_{sura} (B_{rms} , f_{elec}) \quad (3.18)$$

In this section of the thesis only the magnetic heat generation in the stator is calculated where the magnetization changes direction with 180° . The generated heat in the rotor is neglected considering that the magnetization directions are more constant in the rotor even if the flux is large.

The amplitude of the oscillation of the flux density in the stator is obtained from the results of the *electromagnetic FEA*, (see fig 3.36 and 3.37).

In this way the *volume specific heat generation* p_{Fe} for any torque and any speed, can be calculated and be used as input value in the thermal *FEA* which outputs the steady state temperature distribution on the EM. (see figure 3.35 bottom).

Figure 3.36: Flux density B on the EM, when I_0 is applied

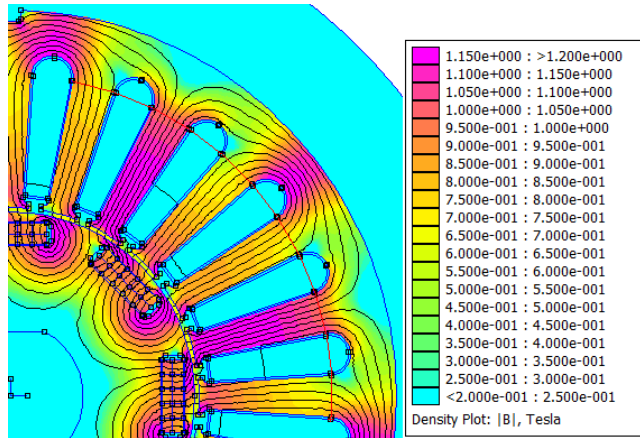


Figure 3.37: Flux density along red line in (figure 3.36) (pos0 : point down right)

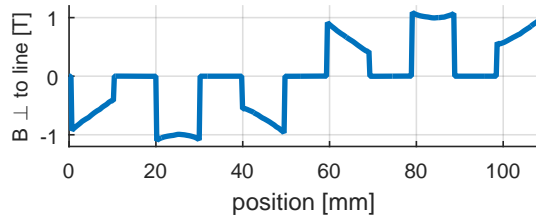


Table 3.13: Values used for the calculation of the heat generation on the iron core of the stator. (material: Sura M250-35A)

| | | | | |
|--------------------------------|-----------------|---|----------------------|----------|
| max flux density | \hat{B} | = | 1.1 | T |
| rms of the flux density | B_{rms} | = | 0.78 | T |
| nominal electric frequency | $f_{el,0}$ | = | 212 | Hz |
| mass spec. heat gen. | $P_{fe}/mass$ | = | 4.12 | W/Kg |
| material density | $mass/volume$ | = | $7.65 \cdot 10^3$ | kg/m^3 |
| volume spec. heat gen. | p_{Fe} | = | 31.515 | kW/m^3 |
| volume of the stator iron core | $volume_{s,Fe}$ | = | $2.54 \cdot 10^{-3}$ | m^3 |
| iron core heat generation | $P_{Fe,stator}$ | = | 80.12 | W |

3.8 Final design and prototype properties

In this section a complete specification list the designed machine is presented.

3.8.a Geometric data

Table 3.14: Geometric data

| | | | | |
|-----------------------|---------------------|---|-----|---------|
| active length | len | = | 200 | mm |
| stator outer diameter | $\varnothing_{s,o}$ | = | 180 | mm |
| stator inner diameter | $\varnothing_{s,i}$ | = | 88 | mm |
| rotor diameter | \varnothing_r | = | 86 | mm |
| nr of pole pairs | $n_{pole\ pairs}$ | = | 4 | |
| nr of slots | | = | 24 | $slots$ |
| nr winding turns | n_{wind} | = | 8 | $turns$ |

See (appendix C) for detailed *CAD* drawings. The values presented in (table 3.15) are calculated considering a simplified geometry based on the *FEMM* model and an active length of 200 [mm].

Table 3.15: Mass and inertia data

| | | | | |
|-----------------------|-------------------|---|-------------------|-----------------|
| steel sheet density | $\rho_{M250-35A}$ | = | $7.65 \cdot 10^3$ | $[kg/m^3]$ |
| rotor mass | m_{rotor} | = | 8.888 | $[kg]$ |
| rotor inertia | J_{rotor} | = | 8.216 | $[g \cdot m^2]$ |
| stator <i>Fe</i> mass | $m_{stator,Fe}$ | = | 19.4 | $[kg]$ |
| stator <i>Cu</i> mass | $m_{stator,Cu}$ | = | 4.2 | $[kg]$ |

3.8.b Mechanical data

Numeric calculations and posterior measurements confirm that the specified mechanic performance values are achieved.

The required mechanical values are presented in (table 3.16).

Table 3.16: Mechanic data

| | | | | |
|----------------|---------------|---|-------|-------|
| nominal power | P_{nom} | = | 15 | kW |
| nominal torque | T_{nom} | = | 45 | Nm |
| peak torque | T_{peak} | = | 90 | Nm |
| nominal speed | $speed_0$ | = | 3183 | rpm |
| top speed | $speed_{top}$ | = | 15000 | rpm |

Measurements described in the following chapters confirm that the top values are reached (table 3.17). The nominal values depend on the cooling system. Numeric simulations confirm that the nominal values are reachable. To determine the required cooling experimentally, thermal measurements would be necessary, but they are not performed in this project. More about thermal measurements is explained in (section 7.2)

Table 3.17: Top measured mechanic values

| | | | | | |
|-------------|---------------|---|-------|-------|---------------|
| peak torque | T_{peak} | = | 99.1 | Nm | (table B.7) |
| top speed | $speed_{top}$ | = | 15690 | rpm | (figure 6.8) |
| top power | P_{top} | = | 22 | kW | (figure 6.10) |

3.8.c Electric data

Here are presented the electric data for the *symmetric hot-side-out* rotor using the *power invariant Park* transformation. Detailed data of the flux-linkage is

found on the (appendix 2.1).

Table 3.18: Electric data, performance and requirements

| | | | | | |
|--|----------------------|---|------|----------|----------------|
| nominal power | P_{nom} | = | 15 | [kW] | |
| magnitude of nominal current | $ \vec{i}_0 $ | = | 110 | [A] | (fig 3.32) |
| rms of phase nominal current | $I_{0,ph,rms}$ | = | 63 | [A] | |
| magnitude of peak current | $ \vec{i}_{peak} $ | = | 194 | [A] | |
| flux for nominal current | $ \psi_s(i_0) $ | = | 147 | [mV · s] | |
| nominal frequency | f_0 | = | 212 | [Hz] | |
| top frequency | f_{top} | = | 1000 | [Hz] | |
| nominal induced voltage | $ \vec{e}_0 $ | = | 196 | [V] | (see eq. 3.9) |
| req. DC-link voltage for $ \vec{e}_0 $ | $U_{dc,min,\vec{e}}$ | = | 277 | [V] | (see eq. 3.10) |
| req. DC-link voltage | $U_{dc,min}$ | = | 300 | [V] | |

Table 3.19: Electric data, passive properties

| | | | | | |
|---------------------------|-----------------|---|-------|----------|----------------|
| phase resistance at 120°C | $R_{phase,120}$ | = | 21 | [mΩ] | |
| inductance in x | L_{sx} | = | 0.813 | [mH] | (see eq. 3.12) |
| inductance in y | L_{sy} | = | 1.516 | [mH] | |
| magnet flux | ψ_m | = | 79.2 | [mV · s] | |

3.8.d Thermal requirements

The design values used in (section 3.7) for the thermal analysis are presented in (table 3.20):

Table 3.20: Thermal requirements

| | |
|-----------------------------------|---------------|
| type of cooling: | water cooling |
| max. allowed coolant temperature: | 100°C |
| max. allowed winding temperature: | 120°C |

3.9 The prototype

The prototype is manufactured by the company *BEVI* located at Blomstermåla in Sweden.

3.9.a The housing and the cooling system

The rotor and the stator are mounted inside a basic housing structure composed mainly of a mantle and 2 quadratic bafflers as shown on (figure 3.38). In the housing there are 24 tunnels in the axial direction forming 4 independent parallel cooling channels. The Housing has not been deeply optimized. The detailed CAD drawings of the Mantle and Baffles are presented in the (appendix C).

Table 3.21: Dimensions of the housing

| | | | |
|--------|---|-----|------|
| length | = | 375 | [mm] |
| width | = | 240 | [mm] |
| height | = | 240 | [mm] |

Figure 3.38: The housing, seen from behind

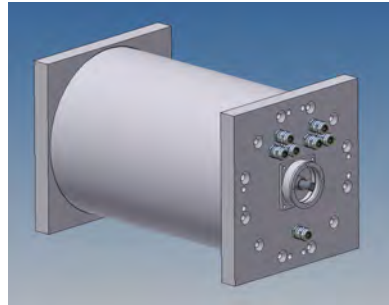


Figure 3.39: The EM from the shaft side. On the sides of the mantle we can see the cables for temperature measurement.

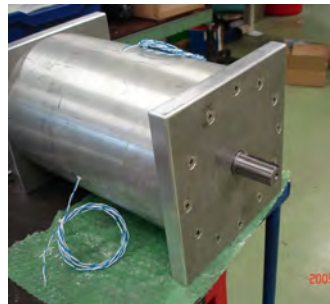


Figure 3.40: The EM with the power cables and water cooling connection. The resolver had not yet been mounted when the picture was taken.



3.9.b The connection for the power cables, the resolver and the temperature sensors.

On the rear baffle 6 holes are drilled for the power cables, forming two equidistant triangles to better cancel the magnetic field created by the phase currents. Here is its possible to access both ends of all phase with the possibility of switching between 'Y' and ' Δ ' connection of the 3-phases system. However the *EM* is designed to use the 'Y' coupling.

On the back side of the shaft a 4 pole pair resolver of type Singlsyn (s-21) is mounted as angular position sensor. (see D.2).

12 temperature sensors of type PT-100 are mounted at different points inside the stator for thermal measurements.

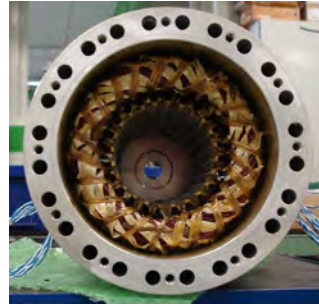
3.9.c The stator and the rotor

The stator and the rotor are composed of electromagnetic steel sheets stacked and welded together that were shaped using laser cutting. The stator pack is sanded and then it is inserted in the pre-heated mantle.

Figure 3.41: The stator inside the housing



Figure 3.42: The Stator with the winding inside the housing.



One stator stack is manufactured and in total 4 rotors (see section 3.6.a and 3.6.b).

Figure 3.43: The rotor being mounted.

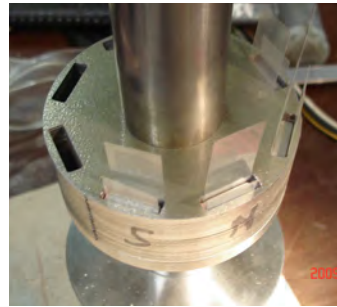


Figure 3.44: One rotor with its shaft and one stator plate compared to the size of a pen.



3.9.d The resolver

A 4-pole-pairs resolver of the the type *Singlsyn* (figure D.2) is mounted on the back side of the *EM* (figure 3.45, 3.46). The resolver has in total 6 cables, 2 for excitation of the resolver, and the other four are, two for sinus, and two for cosinus of the angular electric position θ_{elec} . The sinus and cosinus signals are demodulated in the *FPGA* in the control system.

Figure 3.45: The resolver on the back side of the *EM*.

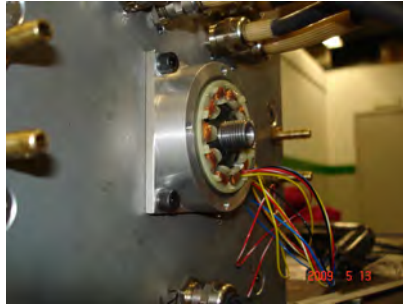
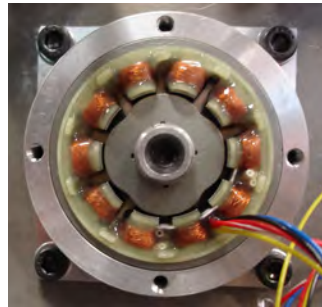


Figure 3.46: The 4 pole pair resolver.



Chapter 4

Description of the *Dynamic Test Method*

Measuring the thermal and electromechanical properties of *Electric Machines (EMs)* is a crucial step in the development of electric drives.

The *Dynamic Test Method* is a very convenient machine characterization method developed by the author of this thesis *Yury Loayza (YL)* during the development of an updated control system for the new *EM*.

Here in *chapter 4*, the main ideas behind this concept are presented. In *chapter 5* the methods used to measure and calculate the different properties of the *inserted Permanent Magnet Synchronous Machine (iPMSM)* are described in detail.

4.1 Information needed from the measurements

Machine measurements are required to obtain thermal and electromagnetic data of the *EM* as a function of applied current, angular speed and temperature. The information needed is for ex.:

- heat generation inside the *EM* as a consequence of applied current and speed
- temperature distribution inside the *EM* depending on the cooling conditions

- torque maps, torque as a function of applied current
- flux maps, magnetic flux as a function of applied current, needed to calculate the among others f.ex. the required battery voltage
- losses and efficiency at different working conditions
- cogging torque, current and voltage ripple
- electric values of the *EM* as resistance and inductance

4.2 Reasons for why measurements are required

Measurements data of the *EM* is needed to:

- verify machine properties obtained from the manufacturer or from numerical simulations
- be used as input data for numerical models of hybrid drives that use the *EM*
- create optimal control systems for the *EM* [33][34]
- updating parameters of the *EM* in the control system after prolonged use for optimal performance
- diagnose the *EM* to prevent failure
- limiting the working parameters to avoid damage.
- dimensioning the electric power components as the battery and *Power Electronics Converter (PEC)*
- dimensioning the cooling system

4.3 Challenges in testing electric machines for vehicle applications

Testing real *EMs*, specially with the requirements for powering vehicles, is a very time consuming and expensive part of the development and often it requires specialized equipment and installations. These measurements need to be done with high accuracy and precision. The test need to be done very carefully to avoid personal damage, damage to the measurement equipment and to the very prototype. Manufacturing a prototype can cost for ex. for the one in this thesis a couple of tens of thousands Euro.

The difficulty increases with higher dynamics of the *EM*, i.e. higher accelerations and higher levels of the testing parameters as max torque, speed, current, voltage that are continuously increasing in the latest years, the more electric power cars are using. Even if any of these parameters alone is not extreme for *EMs* for vehicle applications, cars require quite high levels of them combined. For example large generators handle much more power but run at a more constant speed or with much more smoother speed transitions. Small motors for robots in low power mechatronics for example can have higher dynamics but require less torque.

The test equipment needs to be more robust to handle the increased electric and mechanical levels and the test system need to be more advanced.

4.4 Testing methods

4.4.a The traditional static method

The common way to test *EMs* is in a *Brake Bench*, where another machine called the brake motor counter acts the torque produced by the machine tested. This torque balance allows keeping the rotational speed constant during an arbitrary amount of time, For ex. 1 to 10 seconds. An sketch of the *Brake Bench* is displayed in (figure 4.1) and a picture of it in (figure 4.2)

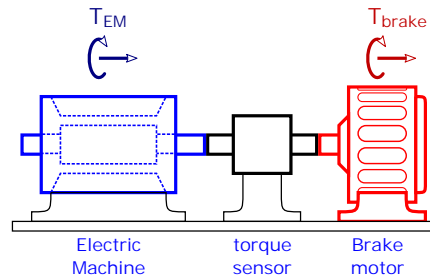


Figure 4.1: Sketch of the *Brake Bench*

Figure 4.2: Picture of a *Brake Bench* with the brake motor (grey). Here neither the tested motor nor the torque sensor are shown. Courtesy of *RISE*, previously *SP*.



On the *Brake Bench* the measurements are static, i.e. the system is moving at constant speed during measurements. Stand still is a special case where the speed is constantly zero.

$$\begin{aligned} \sum T &= J \cdot \frac{d\omega_{mech}}{dt} = 0 && \implies \omega_{mech} = constant \\ \text{where} &&& \\ \sum T &= T_{EM} + T_{brake} + T_{fric} = 0 && \end{aligned} \quad (4.1)$$

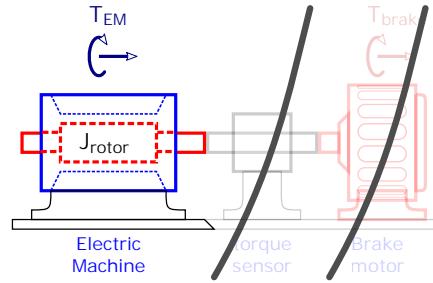
At this static conditions, the average, or respectively the *RMS* values of the most magnitudes as speed, torque, current, voltage are constant and can be measured with standard instruments, as torque sensors, voltmeters, currents meters, that display the average or *RMS* values in real time. The person making the test have enough time to write down the values, or the values can be logged to a computer without high speed of memory requirements. For ex. 10 or 1 sample per second could be enough.

This static method in the break bench is widely used but has some limitations that will be listed in following sections. [35] describes further the test in a *Brake Bench* considering the elasticity and inertia of the components.

4.4.b The *Dynamic Test Method*

In the *Dynamic Test Method* neither brake machine nor torque sensor are needed, see (figure 4.3).

Figure 4.3: Set up of the Dynamic Measurement.



Here a constant current is applied to the *EM* which creates a torque. By the lack of any brake torque, the rotor accelerates according to Newtons second law. This acceleration depends on the magnitude of the created torque and the inertia of the rotor (equation 4.2).

$$\begin{aligned} \sum T &= J \cdot \frac{d\omega}{dt} \neq 0 \implies \text{acceleration} \\ \text{where} & \\ \sum T &= T_{EM} + T_{fric} \neq 0 \end{aligned} \tag{4.2}$$

Because of the non zero torque and the acceleration, this method is called in this thesis as the *Dynamic Test Method*, but methods where the inertia is used as a load are also called Synthetic Loading Techniques in the literature.

Because of the high torque and low inertia expected in specially *iPMSMs* designed for hybrid vehicle applications, it takes very short time to reach a top speed, typically only a fraction of a second. It is no longer actual to calculate average or *rms* values to display for the person making the measurement, instead a series of instantaneous measurements and other variables used by the control system are collected at a high samplig rate, approx 10000 samples/second, and streamed to a computer that calculates the different magnitudes as torque, flux, etc, from the streamed raw data.

The Dynamic Test Method is as we can see more software intensive and requires less equipment than the static method with the *Brake Bench*.

The details of how the different magnitudes are calculated when using the *Dynamic Test Method* are explained in (chapter 5).

4.4.b.1 Benefits of using the *Dynamic Test Method*

The benefits of the dynamic test are in general faster measurement and reduced need of equipment. A comparison between the dynamic and the static method is presented in (table 4.1).

Table 4.1: Comparison between the dynamic and the static method

| <i>Dynamic Test Method</i> | Static Test in brake bench |
|--|---|
| <ul style="list-style-type: none"> • requires less equipment • no need to align components • does not require advanced installations • fast mapping, mapping requires typically some minutes, many speeds are swept in a fraction of a second • Low temperature increase in the tested machine during mapping due short current pulses • more portable • in situ measurements are possible • cleaner, more consistent, high precision measurements data due to less components involved • easier to reach high speeds because fewer and well balanced parts are involved, and that the top speed does not need to be maintained during long time. • only one control unit is required. • high torque measurements are possible by increasing the inertia. | <ul style="list-style-type: none"> • requires more equipment: torque sensor, brake machine, gear box • time consuming alignment of the equipment. Each 2 components in line need to be aligned in 4 degrees of freedom to avoid vibrations at high speeds. • Eventual long waiting time for an available brake bench installation, which can have high rent costs. • time consuming mapping, mapping requires typically some hours, need to stay at certain speed levels for seconds • Large temperature increase • bounded to the bench • in situ measurements are not possible • a lot of measurement noise and vibrations • speed limited by the slowest component and alignment • control unit for the brake motor is also needed • high torque measurements are possible using more robust components |

4.4.b.2 Advantages of the brake bench:

The static method has still its benefits mainly because of its simplicity and that it can be run in a more manual way:

- Strait forward standardized method. The Dynamic Test has a more complex theory behind.

- The static method does not need as an advanced control units as the dynamic test, which requires higher sampling and computation speed, more memory and stable communication to the computer.
- Easier to put in rotation a new uncalibrated machine to be tested
- The Dynamic Test need a fast safety system to avoid over speed
- Easier to select and keep working points for thermal measurements
- higher torque measurements are possible with robust equipment

4.5 Characteristics of this dynamic test method respect to other acceleration methods

There are different convenient methods to measure different internal properties of *EMs* without the need of a *Brake Bench*. What characterized the method presented in this thesis is:

- The operating points, i.e, current vectors, are keep constant independent of the speed, allowing to reach peak power.
- deliver complete torque and flux maps
- It is developed for testing *EMs* designed to power vehicles.
- It can handle high accelerations
- It has been tested on *iPMSMs*.
- It takes advantage of the speed and digital multiprocessing of a *Field Programmable Gate Array (FPGA)* based control system
- Developed using a *CompactRIO* with stable communication to a PC
- Control and measurement developed in Labview and postprocessing in Labview and Matlab.
- neither torque sensor nor load cell are needed.
- no external transmission components other than the very rotor shaft.

4.6 Other methods without brake bench

- **no-load-** or *Zero-current-measurement*. The *iPMSM* is disconnected from the *PEC*. Then the rotor is rotated manually and the induced voltages are

logged using for ex. an oscilloscope. In this way the properties of the *iPMSM* at no current can be obtained, as for example the strength of the magnets, the position of the resolver, cogging, etc.

- Measurement of the **reaction torque** of the stator either quasi static, if the acceleration can be kept constant during long time or dynamic using fast response torque sensors or load cells on the stator. This method can have practical limitations to obtain clean high precision measurements. It can be difficult to mount the stator on a frictionless rotational structure, and the connection and measurements cables will act as springs taking some of the reactions torque.
- Synthetic loading technique for *iPMSMs* applying **oscillating torque** to determine losses [36], where the applied current is not kept constant during the acceleration, but it follows a sinusoidal waveform. Neither torque nor flux maps are obtained.
- Acceleration methods for **Induction Machines** have been developed, for. ex. [37] and are standardized [38].
- Dynamic Test Method for ***DC-motors*** [39] [40] and for different applications[41]
- A method for estimating flux maps for a *iPMSM* is described in [42] where a *dynamometer* is used to rotate the *iPMSM* **at constant speed**. Current measurements and reference voltage are logged and the data is later fitted into a model. The torque is calculated from the flux maps.

4.7 Background

The *Dynamic Test Method* came as unexpected result of the work of the author on updating the control and measurement system used at the *Division of Industrial Electrical Engineering and Automation (IEA)* and the need of mapping the prototype which was originally thought to be done in the *Brake Bench*. It came to awareness a series of difficulties inherent to the use of the *Brake Bench* as mounting and aligning the *EM* and other components, mechanical limitations of the torque sensor, gearbox and brake motor, calibrating and configuring the torque sensor. Further difficulties were expected for speeds above 7500 [rpm].

Calculations of the torque from the acceleration were previously considered to give an estimation with low precision, since the rotor inertia could not yet be measured, nor the friction, nor the flux, and all other component mounted in the

parallel drive bench to connect with the *large bench flywheels* were contributing with new unknowns, friction, vibrations, etc. Previous acceleration methods were intended to calculate single torque values with low precision, not a full torque map and not a flux map.

Accelerating the *large 'vehicle' flywheels* via flexible belt transmission, the gear-box and other components on the parallel drive bench gave a very rough measurement data with a lot of disturbances, noise, vibrations and large friction.

At the same time the new developed control system using *CompactRIO* was revealing improved capabilities in speed, precisions, and measurement data management.

The breakthrough was possible by removing all external loads and running the *iPMSM* with only its rotor as single moving part. The acceleration time here became very short, only a fraction of a second and no values could longer be read and recorded manually but the new developed control system could sample enough data to statistically calculate stable averages.

Still it remained some unknowns, as the value of the friction, the inertia of the rotor, resistive voltage drop, average value of the pulsed voltage, that needed to be solved to be able to calculate the torque and flux maps. The author proposed and tested a set of methods to calculate each of them which are presented in (chapter 5)

In the spring 2010 the first results were shared to colleges at *IEA*, in spring 2011 was presented publicly at the symposium *CEMEC 2011*, in September 2011 this method was presented at the conference in Bologna, Italy [2]. In 2013 a prototype was built and delivered to the industry *SP*. In the latest years the author has done further developments to the control system among others to adapt it to:

- interface the *power grid*
- measurement of the cogging torque (section 5.2.h)
- validation of the method (section 5.3)
- field weakening control (chapter 6)

4.8 Implications of the *Dynamic Test Method*

The *Dynamic Test Method* has already during the development time shown its capabilities in very fast mapping of machines for other theses, masters theses, paper publications and other research projects.

Since the development of the *Dynamic Test Method* a set of new produced *iPMSMs* at de division of *IEA* have been tested using this method.

As a consequence of the positive results of the *Dynamic Test Method*, a set of projects and cooperations were started based on this method. Master Thesis [43] runs the the *Dynamic Test Method* on an *iPMSM* that previously was measured on a *Brake Bench*, and the results of both methods are compared. The master thesis [4] implements a *Direct Current Control* as an alternative to the *PI-control* used previously to run the *iPMSM*. Lic. thesis [44] makes deeper studies on this method, among other to investigate its consistency and standard deviations in the measurements using both *DCC* and *PI-current control* .

Chapter 5

Measurements and calculations with the *Dynamic Test Method*

This chapter explains in detail the different methods used to perform the *Dynamic Test Method* which have been previously presented in (chapter 4).

5.1 Methodology and experimental setup

The strength of the *Dynamic Test Method* consist of an accurate control system and the capability of obtaining large amounts of precision measurement data. This data is fitted to appropriate mathematical models in order to extract the required information needed from the *inserted Permanent Magnet Synchronous Machine (iPMSM)*.

In this chapter, the different methods are presented with real measured data for a better understanding of the challenges and possibilities.

A sketch of the experimental setup is displayed in (figure 5.1) and more details about it are found in (appendix A).

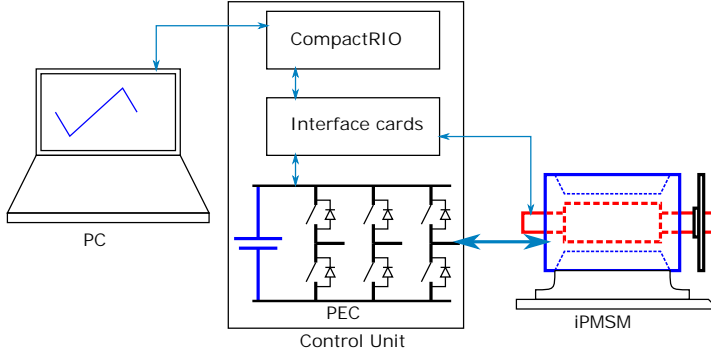


Figure 5.1: Sketch of the experimental setup

5.2 Measurement and calculations

5.2.a Calculation of the torque

A current vector \vec{i}_s is applied, then the rotor accelerates with constant acceleration from $0[\text{Hz}]$ until a certain top speed is reached (see figure 5.2). The oscillations of the current around the mean value as well as the cogging create a torque ripple but in the long term these oscillations cancel out each other.

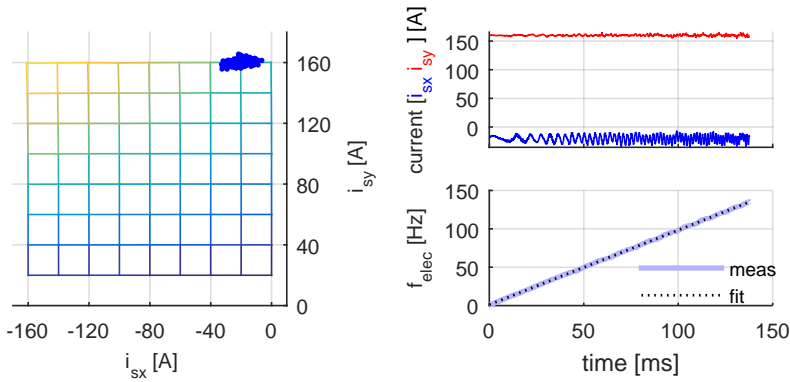


Figure 5.2: Constant acceleration when a constant current is applied

The mean value of the measured current during the acceleration is calculated:

$$\vec{i}_s^{mean} = \text{mean}(\vec{i}_s^{measured}) \quad (5.1)$$

A first degree Taylor approximation of the frequency over time is made:

$$f_{el}^{fit} = p_0 + p_1 \cdot t \quad (5.2)$$

The average electric acceleration is then the slope of the curve f_{el}^{fit} vs *time*.

$$\left(\frac{d f_{elec}}{dt} \right)_{fit} := p_1$$

and the average mechanical acceleration:

$$\frac{d \omega_{mech}^{fit}}{dt} = \frac{2\pi}{n_{polePairs}} \left(\frac{d f_{el}}{dt} \right)_{fit} \quad (5.3)$$

The average torque T for this specific current vector \vec{i}_s is calculated according to (equation 5.4)

$$\sum T(\vec{i}_s^{mean}) = T_{em} \pm T_{loss} = J \cdot \left(\frac{d \omega_{mech}}{dt} \right)_{fit} \quad (5.4)$$

The sum of all applied torques $\sum T$ is composed mainly of the electromechanical torque produced by the *EM*: T_{em} and a set of *loss* torques related to friction, lubricant viscosity, air resistance, etc.

The friction torque and other loss torques are handled in (subsection 5.2.e). These loss torques are very small compared to for example the nominal torque of the studied *EM*, which should be the case for high efficiency, performance and torque *Electric Machines* designed to power vehicles.

The values used for the torque calculation corresponding to the current vector shown in (figure 5.2), are presented in (table 5.1):

Table 5.1: Example of values used for the calculation of the torque corresponding to one of the current vectors

| | | | |
|---------------------------|---|------------------|-----------------------|
| $\vec{i}_{s,set}$ | = | [-20; 160] | [A] |
| \vec{i}_s^{mean} | = | [-20.33; 160.03] | [A] |
| $(d f_{el}/dt)_{fit}$ | = | 972.04 | [Hz/s] |
| $J = J_{rotor} + J_{ext}$ | = | 8.8 + 28.9 | [g · m ²] |
| $\Rightarrow \sum T$ | = | 57.58 | [Nm] |

In this way the torque is calculated for all current points in a mesh, (see figure 5.3) and the values are presented in (table B.7).

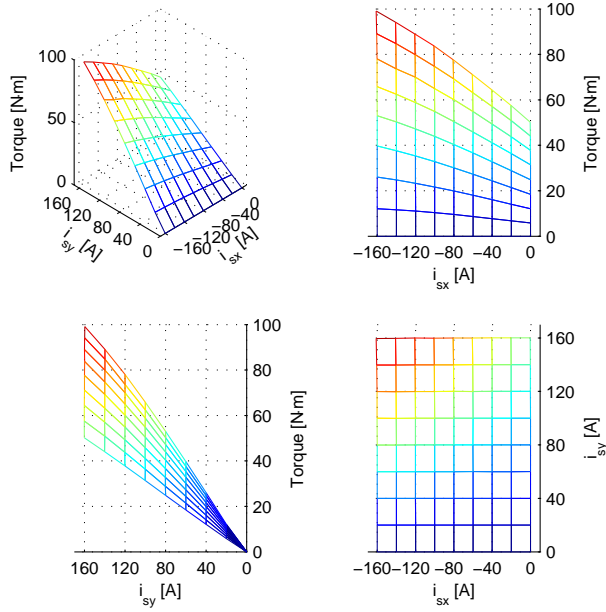


Figure 5.3: Mesh of the torque T as a function of applied current vectors $[i_{sx}, i_{sy}]$

5.2.b Calculation of the flux linkage $\vec{\psi}_s$

In (figure 5.4) we can observe the behavior of the voltage \vec{u}_s during an acceleration with constant current. The current oscillates around its mean value, while the voltage and the frequency increase mainly linearly with time, with oscillations as well. The oscillations are treated in the (subsection 5.2.h), but from the main linear trend the flux linkage is calculated in a similar way as the torque.

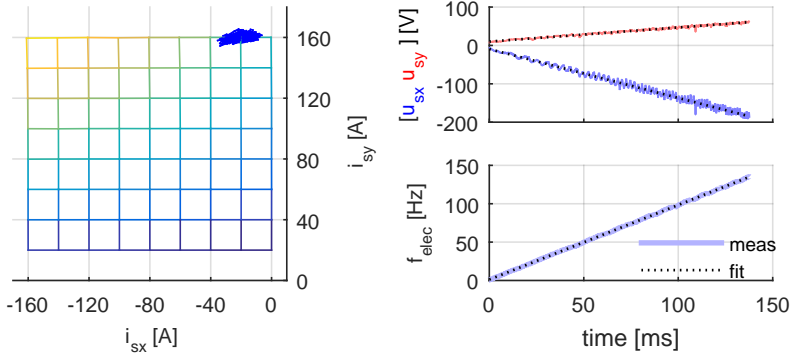


Figure 5.4: Voltage under acceleration

According to Kirchhoff's voltage law applied to the circuit shown previously in (figure 3.15) and in (figure 5.5) and (equations 3.5 or 5.5) representing the *iPMSM*, the only voltage term that is related to the general increase of speed is the *emf*.

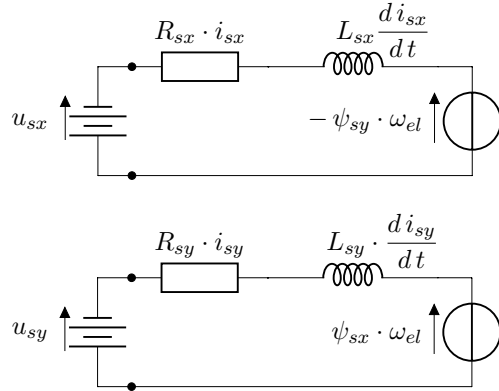


Figure 5.5: Electric representation of the *iPMSM*

$$\begin{aligned}
 u_{sx} &= R \cdot i_{sx} + L_{sx} \frac{di_{sx}}{dt} - \psi_{sy} \cdot \omega_{el} \\
 u_{sy} &= R \cdot i_{sy} + L_{sy} \frac{di_{sy}}{dt} + \psi_{sx} \cdot \omega_{el}
 \end{aligned}
 \tag{5.5}$$

Derivating 5.5 with respect to the time:

$$\left(\frac{d u_{sx}}{dt}\right)_{fit} = \frac{d(R \cdot i_{sx}^{mean})}{dt} + \frac{d(L_{sx} \frac{d i_{sx}^{mean}}{dt})}{dt} - \frac{d(\psi_{sy} \cdot \omega_{el}^{fit})}{dt} \quad (5.6)$$

$$\left(\frac{d u_{sy}}{dt}\right)_{fit} = \frac{d(R \cdot i_{sy}^{mean})}{dt} + \frac{d(L_{sy} \frac{d i_{sy}^{mean}}{dt})}{dt} + \frac{d(\psi_{sx} \cdot \omega_{el}^{fit})}{dt}$$

The resistance R , the inductance L and the flux linkage ψ_m are considered to stay constant during the short amount of time of the acceleration. They are machine properties that depend on the geometry of the EM, the amount of Cu, Fe, magnets in the EM which remain constant during the acceleration with constant current. They also depend on the temperature, but considering that the acceleration takes only a fraction of a second, the increase of the temperature and the effects of it are considered to be neglectable. With the mean current constant we have:

$$\frac{d(R \cdot \vec{i}_s^{mean})}{dt} = 0; \quad \frac{d(L_{sx} \frac{d \vec{i}_s^{mean}}{dt})}{dt} = 0; \quad \frac{d\vec{\psi}_s}{dt} = 0 \quad (5.7)$$

with (eq. 5.7) in (eq 5.6) the value of the flux linkage $\vec{\psi}_s$ for the a certain current point is:

$$\psi_{sx}(\vec{i}) = \frac{\left(\frac{d u_{sy}}{dt}\right)_{fit}}{2\pi \left(\frac{d f_{elec}}{dt}\right)_{fit}} ; \quad \psi_{sy}(\vec{i}) = -\frac{\left(\frac{d u_{sx}}{dt}\right)_{fit}}{2\pi \left(\frac{d f_{elec}}{dt}\right)_{fit}} \quad (5.8)$$

The values used for the calculation of $\vec{\psi}(\vec{i})$ for the current point shown in (figure 5.4) are displayed in (table 5.2).

The values of $\vec{\psi}$ for all measured current points are displayed in (figure 5.6 and 5.7) and listed in (appendix table B.8 and B.9)

Table 5.2: Example of values used for the calculation of $\vec{\psi}$ for one of the current vectors

| | | | |
|--------------------------|---|-----------------|----------|
| $\vec{i}_{s, set}$ | = | [-20 160] | [A] |
| \vec{i}_s^{mean} | = | [-20.33 160.03] | [A] |
| df_{elec}/dt | = | 972 | [Hz/s] |
| du_{sx}/dt | = | -1273 | [V/s] |
| du_{sy}/dt | = | 368 | [V/s] |
| $\Rightarrow \vec{\psi}$ | = | [60 208] | [mV · s] |

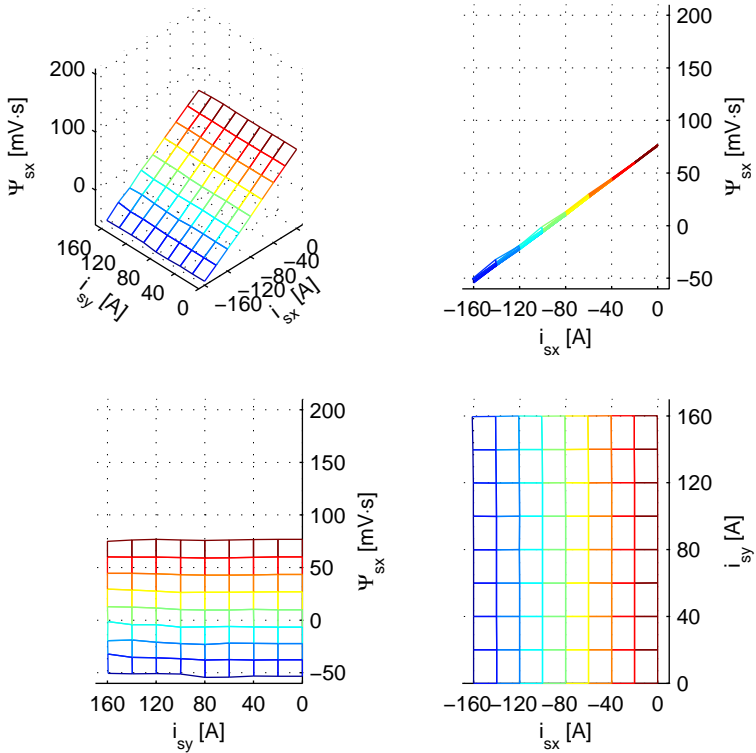


Figure 5.6: ψ_{sx} , the x-component of the Flux linkage, as a function of applied current $[i_{sx}, i_{sy}]$. ψ_{sx} is mainly dependent of i_{sx} and is zero at the demagnetization point $[i_{sx, demag}, 0]$

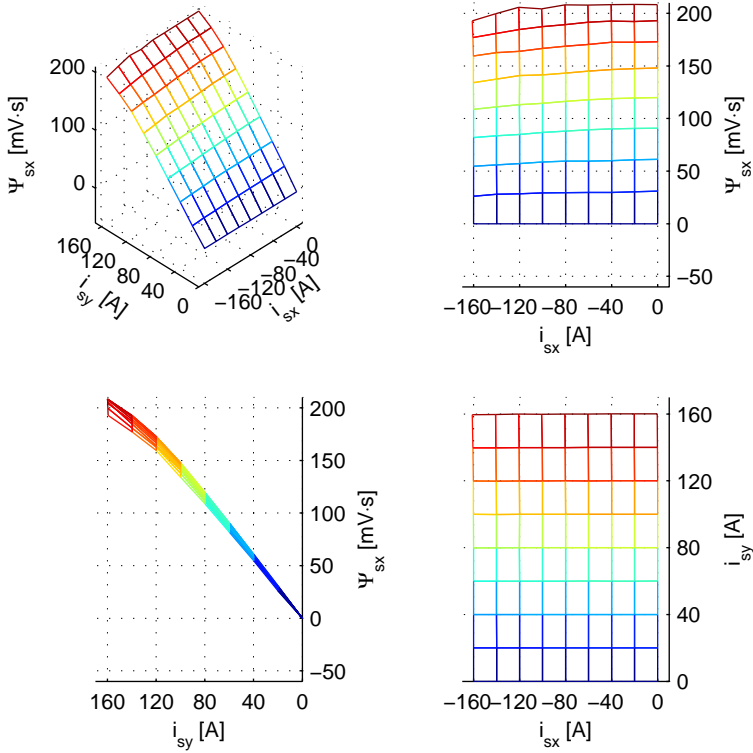


Figure 5.7: ψ_{sy} , the y-component of the Flux linkage, as a function of applied current $[i_{sx}, i_{sy}]$. ψ_{sy} is mainly dependent of i_{sy}

5.2.c The resistance

In (fig. 5.8) we can see a close up of (fig. 5.4) that shows the voltage under an acceleration with constant current. The linear fit of the voltage versus the frequency has an offset $u_{sx,offset}$ and $u_{sy,offset}$ at $f = 0 \text{ Hz}$. According to (eq. 5.5) at $f = 0 \text{ Hz}$ and with constant $di/dt = 0$ only the resistive voltage consumes the applied voltage.

$$u_{sx} = R \cdot i_{sx} + \underbrace{L_{sx} \frac{di_{sx}}{dt}}_{=0} - \underbrace{\psi_{sy} \cdot \omega_{el}}_{=0} \quad (5.9)$$

$$u_{sy} = R \cdot i_{sy} + \underbrace{L_{sy} \frac{di_{sy}}{dt}}_{=0} + \underbrace{\psi_{sx} \cdot \omega_{el}}_{=0} \quad (5.10)$$

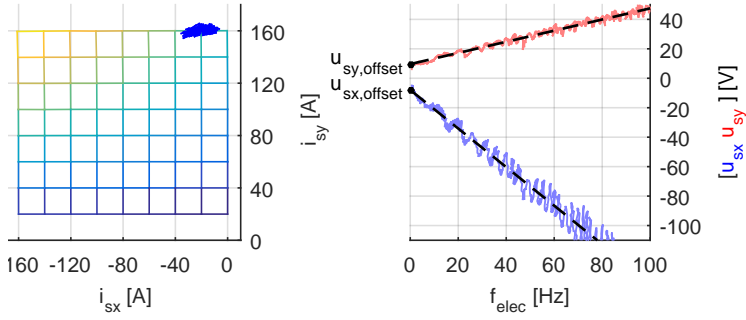


Figure 5.8: Voltage at 0 Hz, to calculate the resistance

In (fig. 5.9) we can see the value of $u_{sy,offset}$ for different values of i_{sy} .

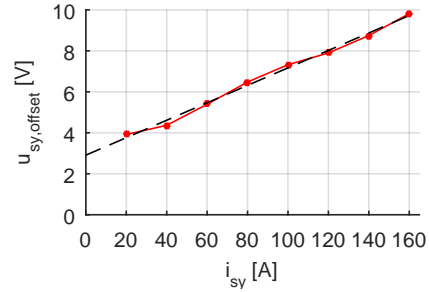


Figure 5.9: Voltage u_{sy} , at 0 Hz vs. current i_{sy} for $i_{sx} = 0$

The resistance R_{sy} is calculated as the general slope of $u_{sy,offset}$ vs i_{sy} . In a similar way, the voltage at 0 Hz, $u_{sx,offset}$ vs. i_{sx} is plotted in (fig. 5.10)

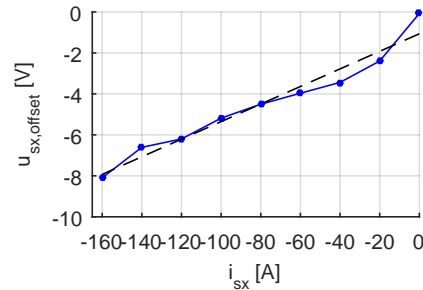


Figure 5.10: Voltage u_{sx} at 0 Hz vs. current i_{sx} for $i_{sy} = 20$ [A]

The resistance values are presented in (table 5.3). The resistance here are measured at room temperature $\tau \approx 20^\circ C$ and include ca 2 m long connection cables from the frequency converter to the EM. The resistance for the copper windings along the active length of the EM has been calculated from the FEA model and material properties previously (see table 3.10).

Table 5.3: Measured resistance using the *PEC*

| | slope [mV/A] | intercept [V] | $R_s + R_{cable} + R_{PEC}$ [mΩ] |
|------------|-----------------|------------------|-------------------------------------|
| <i>x</i> : | 42.9 | -1.064 | 42.9 |
| <i>y</i> : | 42.6 | 2.910 | 42.6 |

Table 5.4: Measured resistance, *4 wire method*

$$\underline{R_{phase} + R_{cable} = 34 \text{ [mΩ]}}$$

5.2.d Calculation of the inertia of the rotor J_{rotor}

To be able to calculate the mechanical torque T from the acceleration according (eq. 5.4), the inertia of the rotor needs to be known or calculated. Often the inertia of the rotor is unknown and difficult to determine directly.

The method proposed and used by the author of this thesis during the development of the *Dynamic Measurement Method* to calculate the inertia, consist in adding external flywheels with different known inertias $J_{ext,k}$ and run accelerations with the same current vector, i.e. the same torque. The value of the rotor inertia J_{rotor} is then calculated by comparing the accelerations $(d\omega/dt)_k$ or $(df/dt)_k$ and an extrapolation.

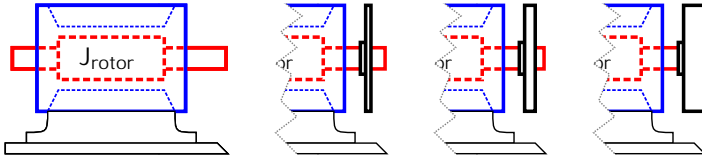


Figure 5.11: Sketch of the EM without and with different external flywheels to determine the inertia of the rotor

Figure 5.12: photo of 3 different external flywheels

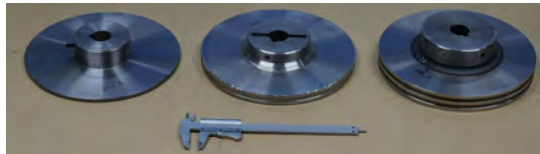
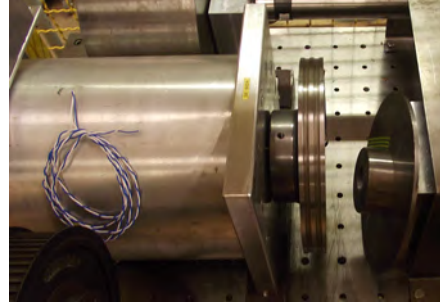


Figure 5.13: The *iPMSM* with the largest external flywheel ($m = 10kg$). The smallest flywheel, ($m = 2.5kg$), is also shown in the picture



The larger the inertia of external flying wheel, the lower the acceleration become when the same torque is applied (see equation 5.11 and figure 5.14).

$$T = (J_{rotor} + J_{ext,k}) \cdot \left(\frac{d\omega_{mech}}{dt} \right)_k \quad (5.11)$$

or:

$$T = (J_{rotor} + J_{ext,k}) \cdot \frac{2\pi}{n_{pole\ pairs}} \left(\frac{df_{elec}}{dt} \right)_k$$

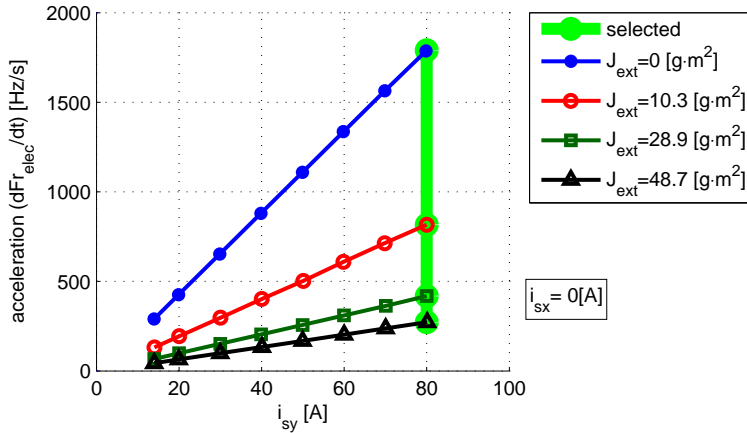


Figure 5.14: Acceleration as function of applied current for different values of added external inertia

From all the current points, one of them, for example $\vec{i}_s = [0 \ 80]$ is selected. The Relation between the acceleration and the added external inertia $J_{ext,k}$ for the selected current current point, i.e. the same applied torque, is an hyperbola. Extrapolating this hyperbola to the left, there is an hypothetic singularity point J_{ext}^* in the negative axis for J_{ext} where the acceleration would become infinity

(figure 5.15). The distance from this singularity point to 0 is the value of the inertia of the rotor J_{rotor} . i.e. the inertia that already existed before adding any external inertia.

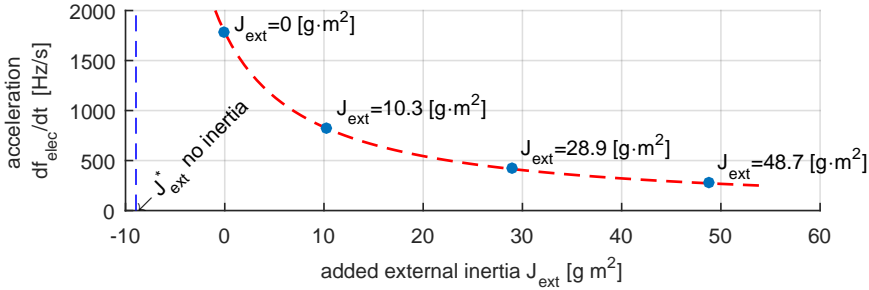


Figure 5.15: Acceleration as function of added external inertia for the current point $\vec{i}_s = [0 \ 80] [A]$

The location of this singularity point J_{ext}^* could be calculated by fitting the the data to a hyperbola but the calculations become easier and statistic more stable if we look at the inverse acceleration where there is a linear relation between it and the added inertia (see figure 5.16).

The inverse of the acceleration can be understood as the time it takes to accelerate from 0 to a certain speed and it is proportional to the total inertia J_{tot} . The location of this point with no inertia is found by extrapolating linearly the data to $inv(df/dt) = 0$ i.e. at which point of J_{ext}^* it would take 0 seconds to accelerate to any speed, i.e. $J_{tot}^* = J_{rotor} + J_{ext}^* = 0$; then the rotor inertia is:

$$J_{rotor} = -J_{ext}^* \quad (5.12)$$

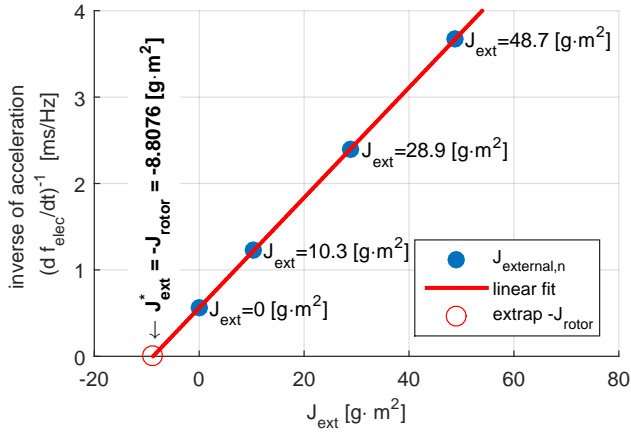


Figure 5.16: Calculation of the inertia of the rotor J_{rotor} using the linear relation that exists between the inertia and the inverse of the acceleration at a constant torque T^* . Here $T^* = T([0\ 80][A])$

The values used for the calculation of the inertia of the rotor are displayed in (table 5.5).

Table 5.5: Values used for the calculation of the rotor inertia

| | | | | | |
|-------------------------|---------------|--------|--------|--------|---------------------|
| k | 0 | 1 | 2 | 3 | |
| mass | | 2.5 | 5 | 10 | [kg] |
| J_{ext} | 0 | 10.261 | 28.918 | 48.741 | [g m ²] |
| df/dt | 1790.9 | 816.5 | 417.9 | 272.3 | [Hz/s] |
| $(df/dt)^{-1}$ | 0.5584 | 1.2248 | 2.3926 | 3.6719 | [ms/Hz] |
| $\Rightarrow J_{rotor}$ | 8.8076 | | | | [g m ²] |
| $T([0\ 80][A])$ | 24.72 | 24.45 | 24.77 | 24.65 | [Nm] |

With the inertia of the rotor J_{rotor} known, the accelerations shown in (figure 5.14) can be translated to mechanical torque T , (table 5.5 last row). As expected a certain current produces the same torque independent of the inertia. The torque for other current values are displayed in (figure 5.17).

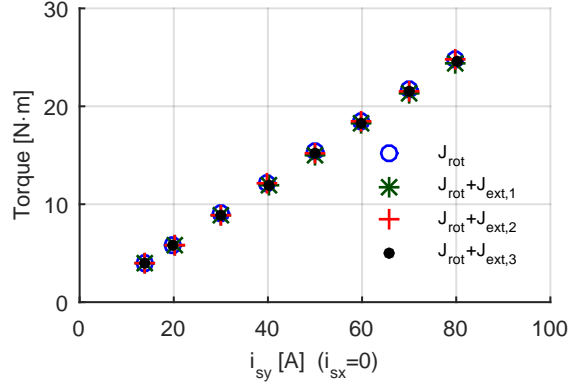


Figure 5.17: Torque as function of applied current for different values of inertia

This method of calculating the location of the virtual zero or virtual origin, in this case when the inertia is zero, is used by the author in his master thesis [45] for a different application but with similar problematic.

5.2.e Separation of the driving torque and the friction torque

The driving torque $T_{driving}$, produced by the EM , is separated from the drag torque $T_{friction}$, caused by friction and viscous losses, by the fact that they act in the same direction during braking and in opposite directions during acceleration (eq. 5.13).

$$\begin{aligned}
 \sum T_{acc} &= T_{driving} - T_{friction} = J \cdot \left(\frac{d\omega}{dt} \right)_{accelerating} \\
 \sum T_{braking} &= T_{driving} + T_{friction} = J \cdot \left(\frac{d\omega}{dt} \right)_{braking}
 \end{aligned}
 \tag{5.13}$$

In (figure 5.18) a deceleration-acceleration sequence from -300 [Hz] to 300 [Hz] with a constant current $\vec{i}_s^{mean} = [0 \ 5][A]$ is shown. The effect of the friction that makes the deceleration or braking stronger than the acceleration is here clearly observed thanks to the low current value.

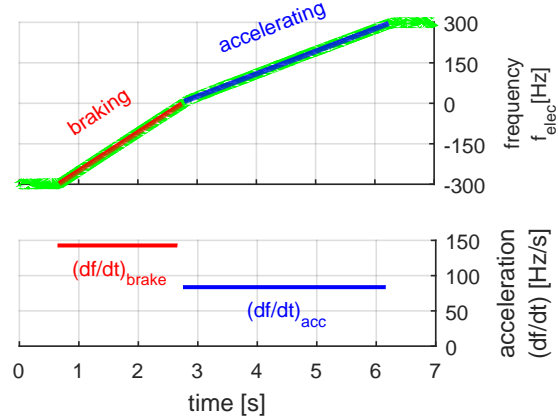


Figure 5.18: Effect of the friction observed in a deceleration-acceleration sequence.

The driving and friction torque can be mathematically expressed using their contributions to the total acceleration, i.e. the driving acceleration the the friction acceleration

$$T_{driving} = J \frac{2\pi}{n_{pole\ pairs}} \left(\frac{df_{elec}}{dt} \right)_{driving}^{fit} \quad (5.14)$$

$$T_{friction} = J \frac{2\pi}{n_{pole\ pairs}} \left(\frac{df_{elec}}{dt} \right)_{friction}^{fit} \quad (5.15)$$

The accelerations corresponding to the driving torque and to the friction are then calculated from (eq. 5.13):

$$2 \left(\frac{df_{elec}}{dt} \right)_{driving}^{fit} = \left(\frac{df_{elec}}{dt} \right)_{brake}^{fit} + \left(\frac{df_{elec}}{dt} \right)_{acc}^{fit} \quad (5.16)$$

$$2 \left(\frac{df_{elec}}{dt} \right)_{friction}^{fit} = \left(\frac{df_{elec}}{dt} \right)_{brake}^{fit} - \left(\frac{df_{elec}}{dt} \right)_{acc}^{fit}$$

The driving acceleration $\left(\frac{df_{elec}}{dt} \right)_{driving}^{fit}$ that could be produced by the *EM*, if no friction were present, is the average of the accelerations measured during braking and acceleration. The friction acceleration $\left(\frac{df_{elec}}{dt} \right)_{friction}^{fit}$ is half the difference between both measured accelerations.

The values used for the calculation of the friction are presented in (table 5.6)

Table 5.6: Values used for the calculation of T_{fric}

| | | | |
|------------------------------------|---|-------------|-----------------------|
| \vec{i}_s^{set} | = | [0 5] | [A] |
| $J = J_{rotor}$ | = | 8.8 | [g · m ²] |
| $n_{pole\ pairs}$ | = | 4 | [1] |
| $(d f_{elec}/dt)_{brake}^{fit}$ | = | 142.7 | [Hz/s] |
| $(d f_{elec}/dt)_{acc}^{fit}$ | = | 83.7 | [Hz/s] |
| $(d f_{elec}/dt)_{friction}^{fit}$ | = | 29.5 | [Hz/s] |
| $T_{driving}$ | = | 1.56 | [Nm] |
| $T_{friction}$ | = | 0.41 | [Nm] |

During the sequence the rotor electric angular position θ_{elec} is measured using the resolver mounted on the *Electric Machine (EM)* (see figure 3.45) and logged. The demodulation is done in the *FPGA*. The speed and the acceleration are calculated as the derivatives of this position θ and are therefore very sensitive to noise and to the influence of the *cogging* of the *EM*.

The data corresponding to the linear deceleration from $-300[Hz]$ to $-5[Hz]$ that corresponds to the braking is separated from the rest and analyzed for it self. In a similar way the data from $5[Hz]$ to $300[Hz]$.

The acceleration $(d f_{elec}/dt)^{fit}$ is calculated using a 2^{nd} degree polynomial fitting of large arrays of data containing θ and *time*. The acceleration is calculated off-line in the post processing of the data. The speed needed for the control is calculated in real time in the *Field Programmable Gate Array (FPGA)* using the first time derivative of θ_{elec} and an Infinite Impulse Response (IIR) filter which takes low resources from the *FPGA*. An interesting alternative method to calculate the speed from the resolver signal is described in [46], the speed can be measured also using a *tachometer* or a *encoder* [47].

The data corresponding to the speed zero crossing is avoided, at zero speed not only there is a discontinuity in the acceleration value but also the effect of *cogging* are very strong, specially at low current values.

When the whole sequence is divided into smaller sections to analyze the friction at different speeds, expecting that the losses should be higher at high speeds, no confirmation from the data is obtained. The effect of speed in the losses is very low for this *EM* (see figure 5.19).

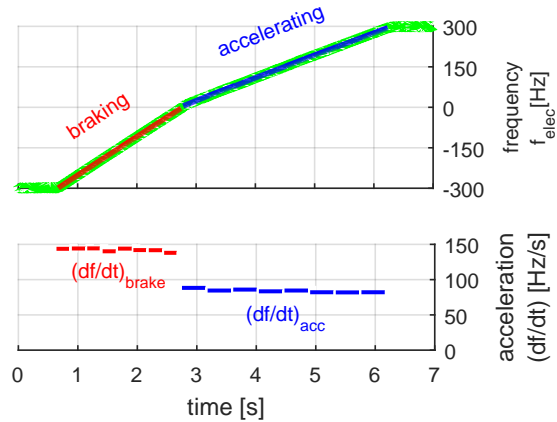


Figure 5.19: Acceleration (df/dt) at different speeds. No clear correlation is observed between the friction and the speed within braking or acceleration period.

5.2.f The friction torque as the offset of the torque-current line

The data of the Torque vs Current for different inertias shown in (figure 5.17) is fitted to a polynomial to be able to make an extrapolation to zero Current. Real measurements at low current are difficult because of the Cogging. In this case a 1st degree polynomial is used, i.e. the dots are fitted to a straight line, considering that the effects of magnetic saturation are not noticeable for these current values for this *EM*.

As we can see in (figure 5.20) the extrapolation does not hit the origin, but the line has an offset to the right, i.e. a certain current is needed to overcome the friction. This is equivalent to consider that the line has a negative offset in the torque which is the friction torque.

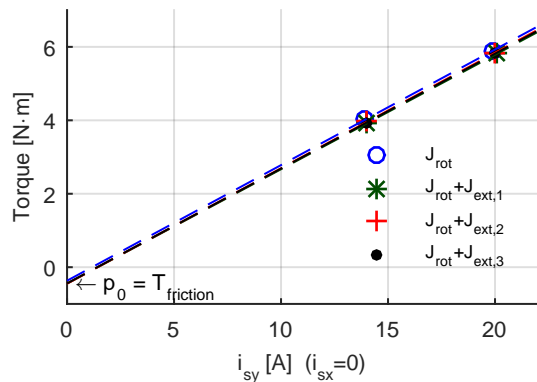


Figure 5.20: Extrapolation of the torque vs. current toward zero to calculate the friction

The parameters of the polynom used here:

$$T = p_1 i_{sy} + p_0$$

are displayed in (table 5.7), where the friction torque is the parameter p_0 . For cases $k_{inertia} = 1, 2, 3$ there is a good match with the value obtained with previous method (table 5.6).

Table 5.7: Friction as extrapolation of torque vs current toward zero

| $k_{inertia}$ | 0 | 1 | 2 | 3 | |
|----------------------|---------|---------|---------|---------|--------|
| p_1 | 0.3148 | 0.3116 | 0.3144 | 0.3128 | [Nm/A] |
| $T_{friction} = p_0$ | -0.3675 | -0.4475 | -0.4484 | -0.4407 | [Nm] |

5.2.g Measurement of the pulsed phase voltage and calculation of the voltage vector \vec{u}_s

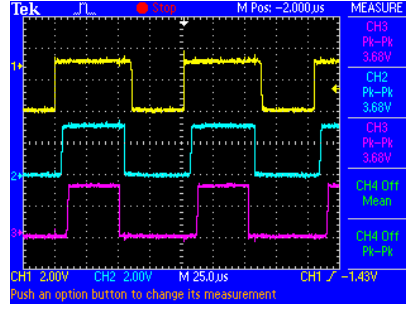
The *DC-link voltage* u_{dc} which is a smooth signal is measured as a conventional analog signal via a voltage transducer (LEM-module) that scales it down to a level between $\pm 10V$. This is feed to an *Analog Input* module of the *cRIO* that samples every $\Delta t_{AI} = 10\mu s$.

Measuring the pulsed voltage on the 3-phase side of the frequency converter can not be done in the same way. The update time of the *Analog Input* module is too long compared to the switching time $\Delta t_{sw} = 102,4\mu s$. It would give an uncertainty of ca. 20 % which were very low precision.

The method proposed and used by the author of this thesis during the development of the *Dynamic Measurement* method is to measure the amplitude and the width of the pulses independently. The amplitude of the pulse is approximated to u_{dc} and the pulse width is measured with higher time resolution using the digital input of the *cRIO* which has an update time $\Delta t_{sDI} = 50ns$. The uncertainty is reduced to ca 0.1 % and the effect of the *blanking time* is automatically accounted for.

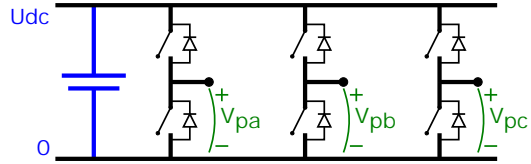
In (figure 5.21) can we see the nature of the pulsed phase voltage.

Figure 5.21: Pulse Width Modulation. The 3 phase pulsed voltages v_{pa} , v_{pb} , v_{pc} , (50x attenuation)



Every phase potential is measured from the output of the frequency converter to the negative side of the *DC-link voltage* 5.22.

Figure 5.22: Measurement point of the instantaneous pulsed voltages



The pulsed phase potentials v_{pa} , v_{pb} , v_{pc} are in principle square waves with an amplitude u_{dc} which is some hundreds of volts. These signals with large amplitude are scaled down using differential probes to a range between 0 and 5 V to be able to be feed into the fast DI modul of the *cRIO*.

A part of the program in the *FPGA* counts how long time, Δt_{high} , the pulsed voltage is high under every switching period Δt_{sw} .

With this information the quasi instantaneous voltage potentials for each phase v_a , v_b , v_c are calculated according (eq 5.17). With quasi instantaneous it is meant the average voltage within one switch period.

The voltage difference between the *dc-link-voltage* and the amplitude of the pulse on the actual phase, i.e. voltage drop in the *Power Electronics Converter (PEC)* is not considered in this thesis. It can be up to ca. 0.7 V and depends on the direction and magnitude of the current. Compared to the ca. 300 V *dc-link-voltage* it is neglected in this thesis, but it should be included in the calculations, if higher accuracy is required, as well as other remaining non ideal converter characteristics.

$$v_a \approx U_{dc} \frac{\Delta t_{high,a}}{\Delta t_{sw}} \quad (5.17)$$

and in a similar way for phases *b* and *c*.

A similar method to measure the switched voltage is described in [48] where a capacitor is used to integrate the phase voltage during every switching period.

In (figure 5.23) we can see for example the phase potential v_a which is an oscillation curve with amplitude and frequency proportional to the electric frequency of the *EM*.

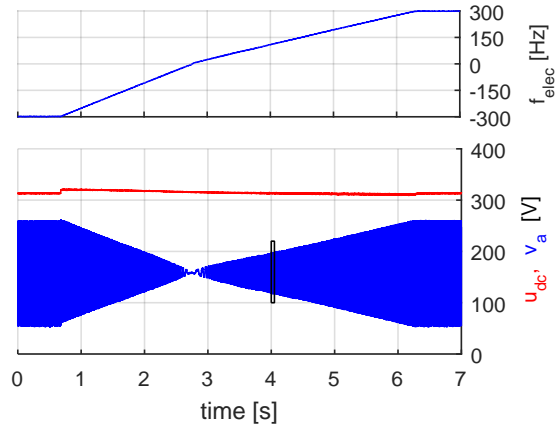


Figure 5.23: DC-link voltage u_{dc} and phase potential v_a during the sequence

The region marked with a black rectangle in (figure 5.23) is displayed in (figure 5.24) with the 3 voltage potentials. The characteristic curve for symmetric modulation is clearly seen.

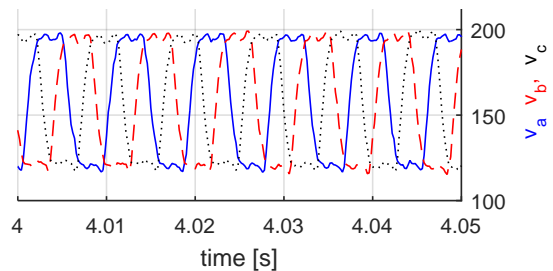


Figure 5.24: Close up showing the 3 phase voltages

For these measurements, the voltage drop in the *IGBT* $\delta U_{IGBT} \approx 0.7$ [V] have not been considered in the calculations in the *FPGA* to simplify the implementation.

When the voltage potentials are determined, the voltage vectors in the stator and rotor coordinate systems are calculated using the *Park Power Invariant Transformation* [5] (figure 5.25).:

$$v_0 = \frac{1}{3} (v_a + v_b + v_c) \quad (5.18)$$

$$\begin{bmatrix} u_\alpha \\ u_\beta \end{bmatrix} = \sqrt{\frac{3}{2}} \begin{bmatrix} v_a - v_0 \\ \sqrt{\frac{1}{3}} (v_b - v_c) \end{bmatrix} \quad (5.19)$$

$$\begin{bmatrix} u_{sx} \\ u_{sy} \end{bmatrix} = \begin{bmatrix} \cos \theta & -\sin \theta \\ \sin \theta & \cos \theta \end{bmatrix} \begin{bmatrix} u_\alpha \\ u_\beta \end{bmatrix} \quad (5.20)$$

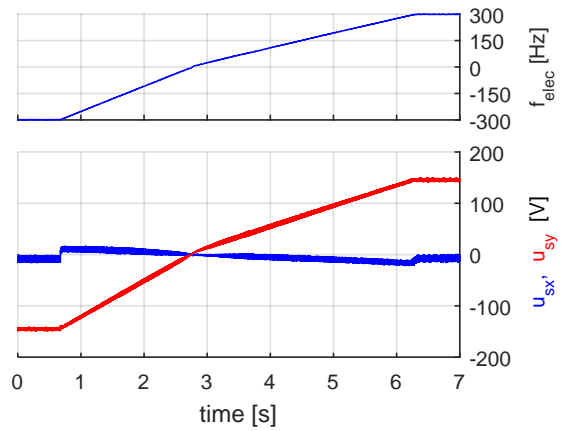


Figure 5.25: Voltage vector \vec{u}_s in the rotor coordinate system xy during the brake-acceleration sequence

Often, for pure motor control, it is not necessary to measure the output voltage to run the *EM* but this output voltage is required for characterizing the *EM*, to determine the *flux linkage* $\vec{\psi}$ or to calculate the consumed electric power P_{el} or the electric torque T_{el} .

5.2.h Cogging

When the *EM* is running, a series of oscillations in the voltage, current and torque are present. And the most preponderant is the oscillation that repeats 6 times per electric turn.

In this project there is not any deep attempt to suppress the oscillations in the current and voltage caused by the cogging but an attempt to measure the effects of these oscillations without the need of a brake bench or a torque sensor

in accordance to the *Dynamic Measurement Technique*, specially to quantify the *cogging torque*.

As mentioned in (subsection 3.6.a) the variation of the flux linkage depending on the rotor position $\vec{\psi}(\theta) \neq const.$ caused by the irregularity of the stator in the tangential direction, i.e. alternation of copper slots and iron teeth, induces an oscillation in the voltage which in its turn causes an oscillation in the current and in the torque.

$$\begin{aligned} \vec{u}_{cogg} &= \frac{d\vec{\psi}(\theta)}{dt} = \frac{d\vec{\psi}(\theta)}{d\theta} \cdot \frac{d\theta}{dt} \\ &= \frac{d\vec{\psi}(\theta)}{d\theta} \cdot \omega_{elec} \end{aligned} \quad (5.21)$$

At the same time the *cogging torque* is caused by the higher reluctance on the iron teeth compared to the reluctance on the copper slots forcing the rotor to stay at the positions where the magnets are closer to the iron teeth.

Another cause of oscillations specially in the voltage is the presence of blanking time which creates a difference between the reference phase voltage and the actual applied voltage depending on the sign of the phase current. It creates a non smooth jump in the phase voltage every time the phase current, which basically is a sinus with some harmonics, crosses the zero level. In the three phase *Electric Machine* it also creates 6 oscillation per electric turn.

Other causes can be for example mechanical irregularities in the construction of the EM or differences between the phases.

The behaviour of the oscillations in the current when running the deceleration-acceleration sequence shown in (figure 5.19) using *PI-control* can be observed in (figure 5.26) and a close up in (figure 5.27).

Figure 5.26: Oscillations of the current during brake-acceleration sequence with PI-current control

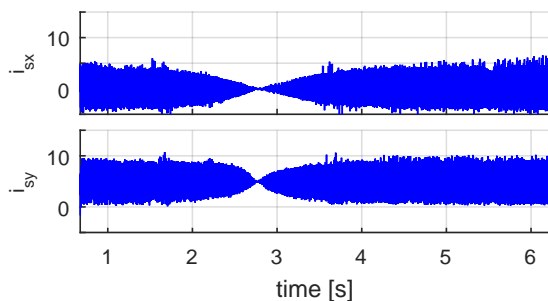
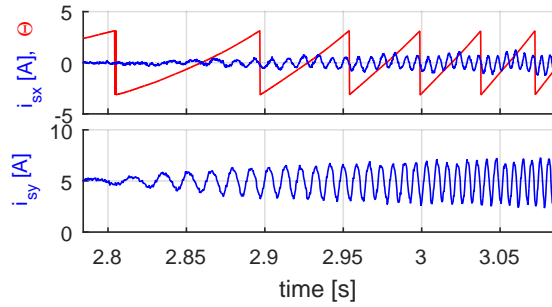


Figure 5.27: Oscillations of the current, close up



At low speeds, the amplitude of the oscillations in the current is proportional to the magnitude of the speed, while at higher speeds this amplitude remains constant. According to (eq. 5.21) the induced cogging voltage increases with speed, generating oscillations in the current. The *PI-current-controller* tries to cancel this oscillation creating an oscillation in the reference voltage. At higher speeds the period time is so short that the amplitude of the current oscillations no longer continues to increase.

$$i = L \int u(t) dt$$

In (figure 5.28 and 5.29) it is possible to observe that these oscillations are phase locked to the rotor electric angular position θ and that the predominant harmonic is the one that repeats 6 times per turn.

Figure 5.28: The current vs the electric rotor position θ

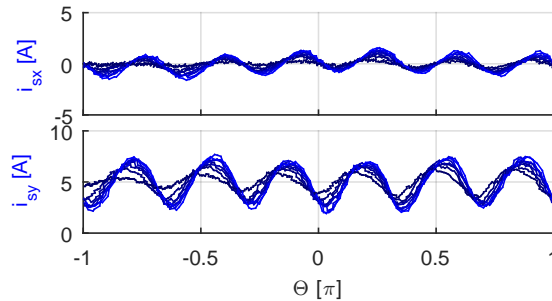
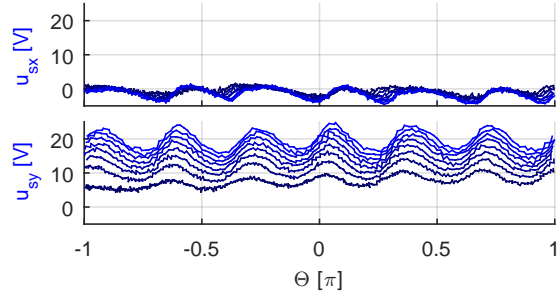


Figure 5.29: The voltage vs the electric rotor position θ



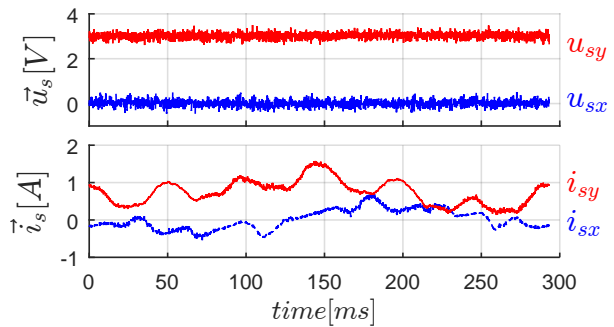
When running the *EM* using a *PI current control* the oscillations in the voltage, current and speed affect each other in a complex way. In order to make more precise observations it is appropriate to keep one of them constant.

5.2.i Calculation of the cogging from the oscillations

The approach of quantifying the cogging torque consist on analyzing the oscillations in the rotor motion produced by it.

Here it is important to eliminate other factors that could create oscillations specially any low frequency ripple on the current. This is better obtained by letting the *EM* run at low speed in *Open Loop Voltage Control*, i.e. a constant reference voltage is applied just high enough to overcome friction and the cogging torque, see (figure 5.30).

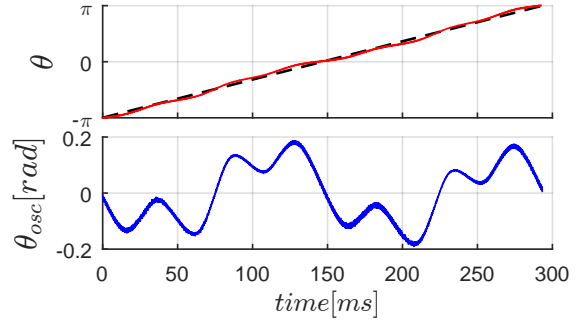
Figure 5.30: Constant voltage is applied. The oscillations in the current are reduced by keeping the speed low.



For further analysis the motion of the rotor is decomposed into 2 motions: the motion at the average electric angular speed $\omega_{el,mean}$ and the oscillations $\theta_{osc}(t)$, see (eq. 5.22) and (figure 5.31).

$$\theta(t) = \omega_{el,mean} \cdot t + \theta_{osc}(t) \quad (5.22)$$

Figure 5.31: Electric angular position θ at low speed. The speed in average is constant. The oscillations only in the lower part.



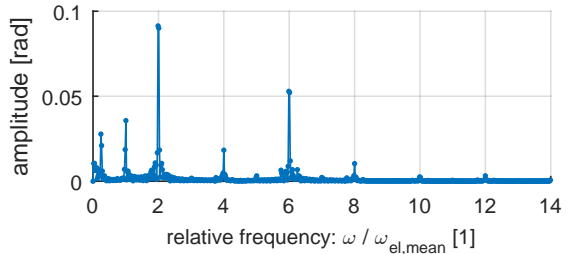
The constant electric angular speed $\omega_{el,mean}$ is obtained as the slope of the linear fitting of θ over time.

The curve containing only the oscillations, contains information about the accelerations caused by the cogging torque but also measurement noise. In order to remove the noise to make clean calculations of the time derivatives, here it is considered most appropriate to fit the data to a sum of sinusoidal functions, i.e. as the sum of its harmonics, see (eq. 5.23) and (fig. 5.33).

$$\theta_{osc}(t) \approx \theta_{osc}^{fit}(t) = \sum_{i=0}^n a_i \sin(b_i t + c_i) \quad (5.23)$$

To improve the process of fitting the data, a spectrum analysis is done (fig. 5.32). The *Fast Fourier Transform* returns the most important frequencies, i.e. values of b_i in (eq 5.23).

Figure 5.32: Spectrum of the oscillations of θ



A number of 5 el. angular speeds b_i corresponding to [1, 2, 4, 6, and 8] times the rotation speed $\omega_{el,mean}$ are selected and the values of a_i and c_i in (eq 5.23) are obtained using the fitting tool in *Matlab* with $n = 5$. The values are presented

in (table 5.8) and the harmonics are shown in (fig. 5.33). An alternative method to calculate the harmonics on real time is described in [49].

Figure 5.33: The oscillations of θ approximated as a sum of harmonics

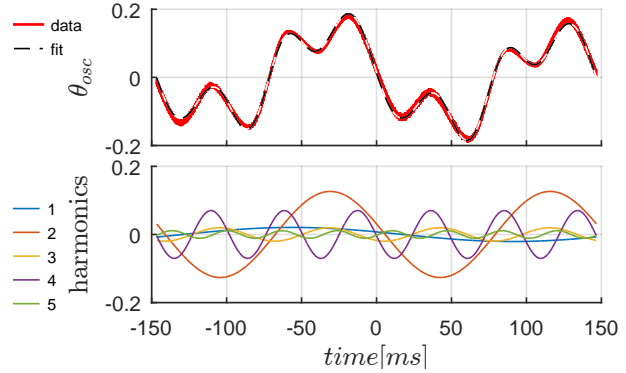


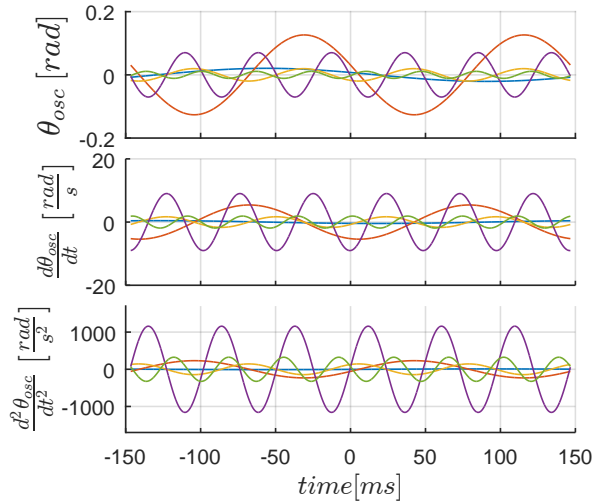
Table 5.8: Parameters of the harmonic fitting

| i | a [rad] | b [rad/s] | c [rad] | $b/\omega_{el,mean}$ | $\omega_{el,mean}$ [rad/s] |
|---|----------|-----------|---------|----------------------|----------------------------|
| 1 | 0.020690 | 21.42 | 2.769 | 1.00 | 21.417 |
| 2 | 0.126300 | 42.83 | -3.389 | 2.00 | |
| 3 | 0.019630 | 85.65 | 10.530 | 4.00 | |
| 4 | 0.070170 | 128.50 | -3.086 | 6.00 | |
| 5 | 0.011050 | 171.30 | -0.224 | 8.00 | |

The first and second time derivative of each of the harmonics are calculated analytically according to (eq. 5.24) and are displayed in (figure 5.34).

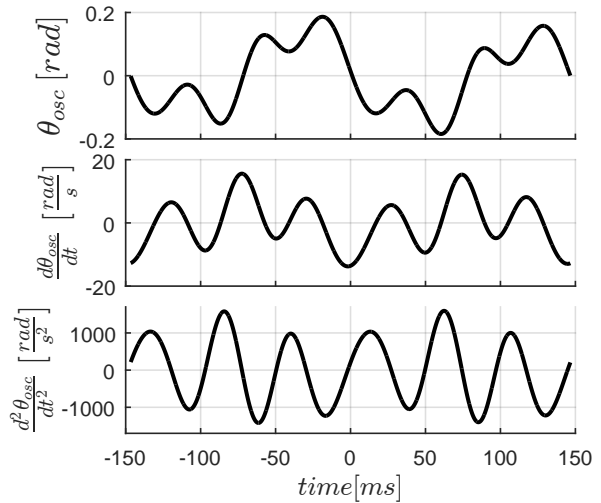
$$\begin{aligned}
 \text{electric position:} \quad \theta_{osc,i} &= a_i \sin(b_i t + c_i) \\
 \text{electric speed:} \quad \frac{d\theta_{osc,i}}{dt} &= a_i b_i \cos(b_i t + c_i) \\
 \text{electric acceleration:} \quad \frac{d^2\theta_{osc,i}}{dt^2} &= -a_i b_i^2 \sin(b_i t + c_i)
 \end{aligned} \tag{5.24}$$

Figure 5.34: The harmonics of the oscillations of the electric angular position θ_{osc} and the corresponding time derivatives: speed and acceleration



The reconstructed oscillations as a sum of the harmonics and the corresponding speed and acceleration are shown in (figure 5.34).

Figure 5.35: The reconstructed oscillations as a sum of its harmonics and the corresponding speed and acceleration



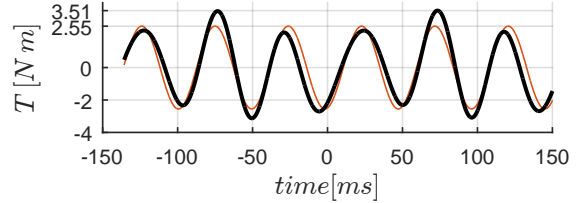
In (figure 5.34, lowest), we can see that the harmonic component that experiences larger acceleration ripple is the one that repeats 6 times per electric turn, i.e. $i = 4$ in (table 5.8). This harmonic match the number of torque ripples according to the design of the studied *EM*.

The torque ripple or cogging is here direct proportional to the acceleration ripple and is calculated according (eq. 5.25) and shown in (figure 5.36). The value of

the rotor inertia: $J_{rotor} = 8.8076[g \cdot m^2]$ has been calculated previously, see (figure 5.16).

$$T_{cogging} = J \frac{1}{n_{pole\ pairs}} \frac{d^2 \theta_{osc}}{dt^2} \quad (5.25)$$

Figure 5.36: The cogging torque and the contribution of the strongest harmonic.



5.2.j Calculation of the cogging torque from the current needed to start the electric machine

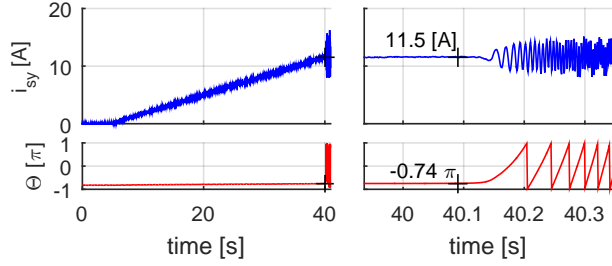
One very important effect of the cogging torque is that a quite large current is necessary to start the *EM* from standstill, i.e. to overcome the cogging torque besides of the static friction, even if the *EM* is unloaded.

$$T_{start} = T_{friction} + T_{cogging} \quad (5.26)$$

Once the *EM* is running the kinetic energy helps to overcome the cogging torque and current is only needed to overcome the kinetic friction. In the case of this *EM* with the rotor that has the largest cogging, the cogging torque is of a much larger magnitude than both kinds of friction. Even if often the static friction is slightly larger than the kinetic one, this difference is not further investigated in this thesis. In this measurement the rotor with *symmetric* magnet placement and the *hot-side-out* is mounted (see section 3.6.a).

The current necessary to start the *EM* is determined by slowly and smoothly increasing the y-component of the current $i_{sy,set}$ with $i_{sx,set} := 0$, until the *EM* starts to spin and immediately reducing the current back to zero.

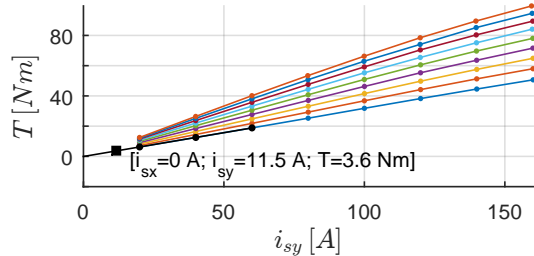
Figure 5.37: Current necessary to overcome the cogging torque



An appropriate way to proceed with this measurement within a controlled speed range, is to keep the control system in *speed-control-mode*, setting a moderate high speed reference, f.ex. the nominal speed, setting a large proportional term Kp and deactivating the integral term, i.e. $Ki = 0$ in the *PI-current-controller* and limiting the allowed current. Then slowly increasing the range of allowed current.

The torque T_{start} that corresponds to the current i_{start} is calculated using the torque-current-map values (presented in fig 5.3), (see fig. 5.38)

Figure 5.38: Necessary torque to start



The cogging Torque $T_{cogg,start}$ is calculated according to (eq. 5.26) subtracting the friction torque from T_{start} . The friction value used here is the one presented in (table 5.6).

$$T_{cogg,start} = T_{start} - T_{friction} = 3.20 \text{ Nm} - 0.41 \text{ Nm} = 2.79 \text{ Nm}$$

5.2.k Comparison between the results of both methods to measure the cogging torque

In (fig. 5.38) we can see the results of both methods in the same graph. There is a good match in the magnitude of the calculated cogging torque from both

methods and also that the the angular position θ_{start} , i.e. where the rotor get stuck at start, match a negative maximum in the oscillations of the rotor, i.e. where the cogging is slowing down at most the motion of the rotor. The values are displayed in the graph.

Figure 5.39: Comparison between the start torque and the cogging torque

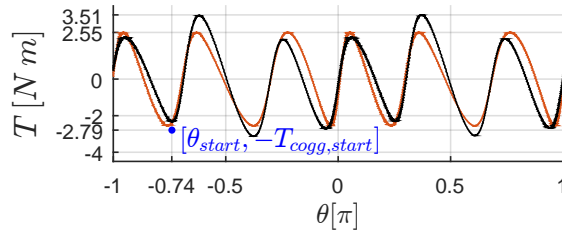


Table 5.9: Values for the cogging torque

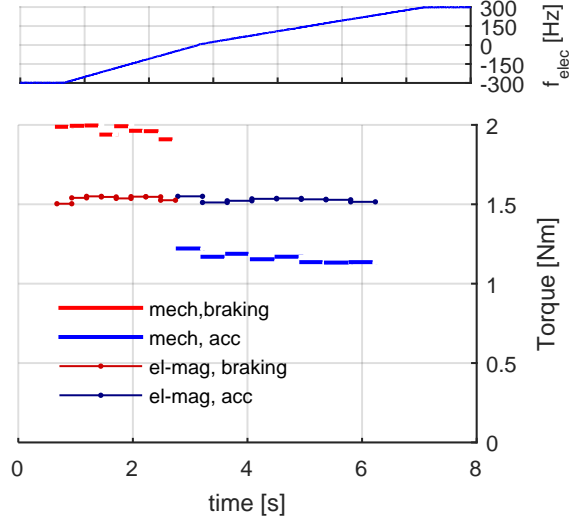
| | | | | |
|------------------------|---|------|------|---|
| $T_{cogging,osc tot}$ | = | 3.51 | Nm | sum of harmonics |
| $T_{cogging,osc harm}$ | = | 2.55 | Nm | 1 harmonic: $6 \times \omega_{el,mean}$ |
| $T_{cogging,start}$ | = | 2.79 | Nm | from standstill |

5.3 Validation

5.3.a The mechanic and the electromagnetic and torque

In (figure 5.40) we can see a comparison between the mechanic torque T_{mech} and the electromagnetic torque T_{el-mag} during the braking acceleration sequence with low current.

Figure 5.40: Mechanic and Electromagnetic torque.



The mechanic torque T_{mech} is calculated from the measurements of the electric angular position θ and the estimation of the inertia J .

$$T_{mech} = J \cdot \frac{2\pi}{n_{pole\ pairs}} \left(\frac{d f_{elec}}{dt} \right) \quad (5.27)$$

Then mechanic torque is affected by the friction as previously shown in (figure 5.19) and the *Driving Torque* can be estimated as the average of the mechanical torque during deceleration and the one during acceleration. The driving torque could be understood as the torque if there were no friction.

$$T_{mech,driving} = \frac{T_{mech,brake} + T_{mech,acc}}{2} \quad (5.28)$$

On the other hand the electromagnetic torque T_{el-mag} , created by the interaction of the magnetic flux linkage and the current in the *EM*, is calculated from the current and the voltage values besides the speed which is derivated from the position θ . This Electromagnetic torque is not affected by the friction.

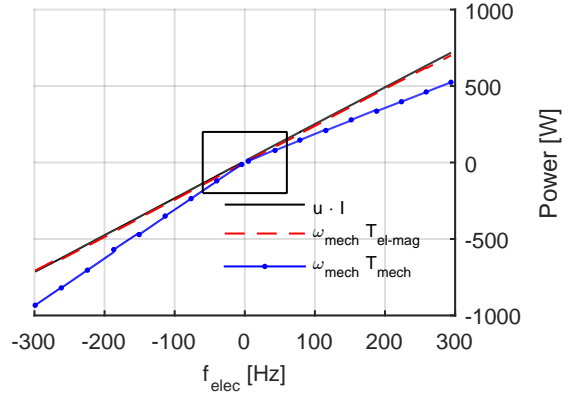
$$T_{el-mag} = n_{pole\ pairs} \cdot \begin{bmatrix} \psi_{sx} \\ \psi_{sy} \end{bmatrix} \times \begin{bmatrix} i_{sx} \\ i_{sy} \end{bmatrix} \quad (5.29)$$

As we can see, there is a good match between the mechanical driving torque $T_{driving}$ and the electro magnetic torque T_{el-mag} , i.e. T_{el-mag} matches the average

of $T_{mech,brake}$ and $T_{mech,acc}$ which indicates a good consistency and accuracy of the Dynamic Measurement technique.

5.3.b Electric, electromagnetic and mechanical power

Figure 5.41: Electric, electromagnetic and mechanical power



In (figure 5.41) we can see the comparison between the three different kind of power: the *Active Electric Power* supplied from the *Inverter* to the *EM*:

$$P_{elec} = \vec{u} \cdot \vec{i} = u_{sx} i_{sx} + u_{sy} i_{sy}$$

The *Electromagnetic Power* in the *Stator*:

$$P_{el-mag} = \omega_{mech} \cdot T_{el-mag}$$

and the *Mechanical Power*

$$P_{mech} = \omega_{mech} \cdot T_{mech}$$

For the calculation of the electric power here the first degree Taylor approximations of the voltage vs time during deceleration resp. acceleration are used instead of the instantaneous value of the voltage. In a similar way the averages of the current are used. Multiplying the raw data of the voltage by the raw data of the current gives too much noise. i.e:

$$P_{elec} := \vec{u}_{fit} \cdot \vec{i}_{mean}$$

As expected during the accelerating part of the sequence where the power flow is from the *Inverter* to the *Stator* to the *Rotor* with losses in between:

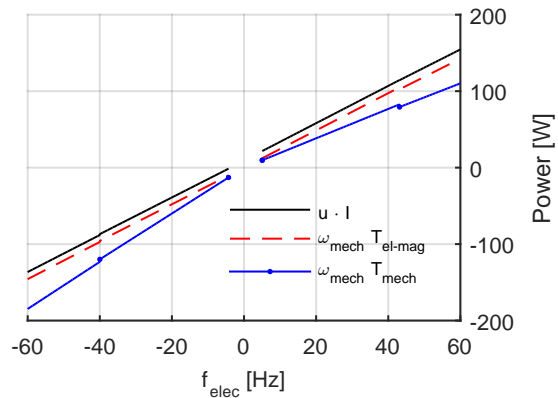
$$|P_{elec}| > |P_{el-mag}| > |P_{mech}|$$

And in the deceleration or braking part of the sequence where the Electric Machine is working as a generator, the source of energy is the kinetic one in the rotor, the power flow is going in the opposite direction with losses in between:

$$|P_{elec}| < |P_{el-mag}| < |P_{mech}|$$

(Figure 5.42) shows a close up where the difference between the three kinds of power is more visible.

Figure 5.42: close up of the Electric, Electromagnetic and Mechanical power



The difference between electric power and the electromagnetic power is mainly caused by the resistive losses in the electric conductors.

In the measurements of this *EM*, as in the comparison of the torques, no clear dependency of the losses as a function of speed are visible.

The logical results of the comparison between the three kinds of power is a confirmation of the the accuracy of the voltage and current measurements and of the calculations used in this method.

5.3.c Comparison and validation of the dynamic measurement vs. finite element analysis

The results obtained using the *Dynamic Measurement Method* are compared with the data obtained from the *Finite Element Analysis*. Both components of the flux linkage ψ_{sx} and ψ_{sy} as well as the torque T are compared.

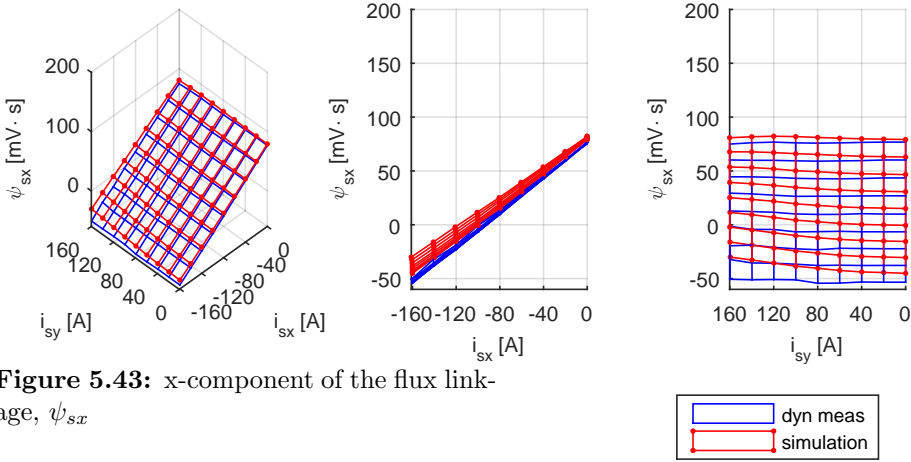


Figure 5.43: x-component of the flux linkage, ψ_{sx}

Comparing the x-component of the flux linkage in (fig 5.43) we can see that:

- Both surfaces have the same slope, specially for low i_{sy} , which is a good match in the relation of how the magnetic field is affected by the current.
- The surface corresponding to the the *FEA* lies higher than the one from the measurement. This means in general a weaker interaction of the magnet with the winding in the stator. Either the magnets are stronger in the model then in reality or there is more flux leakage in reality than in the model.

The first option is not likely considering that the model is created using accurate data from the magnets. The other option is more likely, specially because of the high sensibility in the model to the size of the free space in the magnet pockets. Around the magnets small variations within fractions of a millimeter in the geometry have large effect in the amount of *flux leakage* (fig C.5).

- In general ψ_{sx} should depend mostly of i_{sx} and not be affected by i_{sy} when the iron core is not saturated. In the *FEA* there is curvature in the lines ψ_{sx} vs i_{sy} which corresponds to *cross saturation* of the iron core in the simulations which is not present in reality.

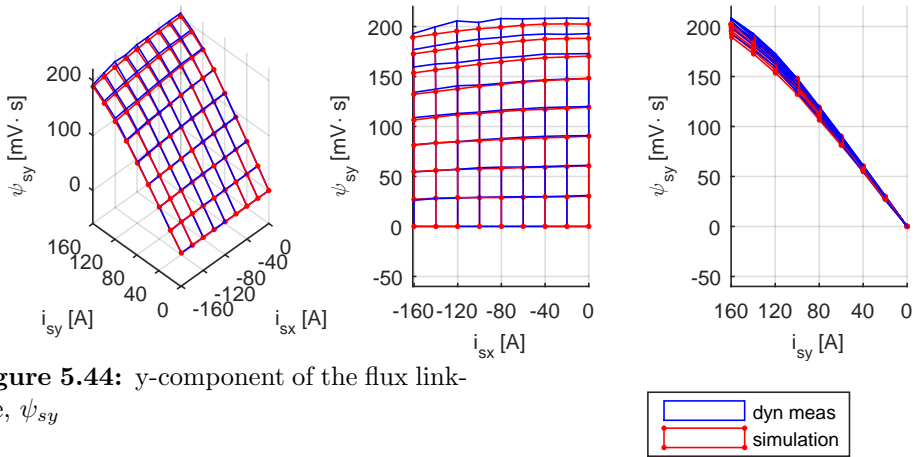


Figure 5.44: y-component of the flux linkage, ψ_{sy}

In (figure 5.44) we can see the values of ψ_{sy} from both methods.

- There is a good match between them specially for low currents.
- The slope of the surface corresponding to the simulation begins to flatten faster, i.e. for lower values of i_{sy} . This implicates that the steel plates in the real motor do not saturate as easily as in the simulation model.
- For high currents the surface corresponding to the Dynamic Test is less smooth which can be caused by less data because of shorter acceleration interval at high currents.

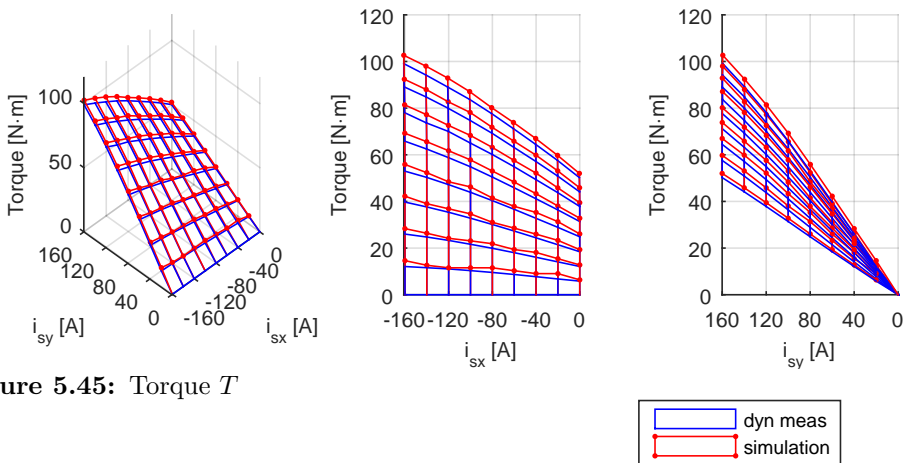


Figure 5.45: Torque T

There is a good match in the shape of the both torque surfaces (figure 5.45). The torque surface from the numerical simulation lies overall higher, which is a consequence of the higher ψ_{sx} for the *FEA* mentioned above. To the torque values obtained from the acceleration the friction has been added to make a more appropriate comparison to the results from the numeric simulations.

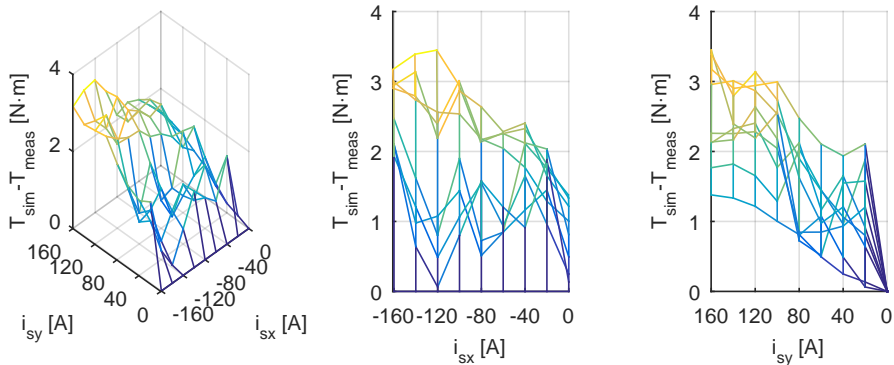


Figure 5.46: Difference between the measured and simulated torque $T_{sim} - T_{meas}$

In (figure 5.46) the difference between the torque calculated with both methods is displayed. An overall systematic error of $2[Nm]$ and a more random error of $\pm 1[Nm]$ are observed. These are low error values considering that torques up to $100[Nm]$ have been measured.

5.3.d Comparison between static and dynamic measurements

The *EM* named "*Evolution*" which is the one designed and presented in this thesis has not been mapped using the conventional static mapping method on a brake bench. Another electric machine designed by PhD Student Rasmus Anderson in the project *ExSam* [12] has been mapped using both methods, the *Dynamic Test Method* and the static method in a *Brake Bench*.

In (fig. 5.47) we can see the *torque maps* of the electric machine *ExSam-3Ph*.

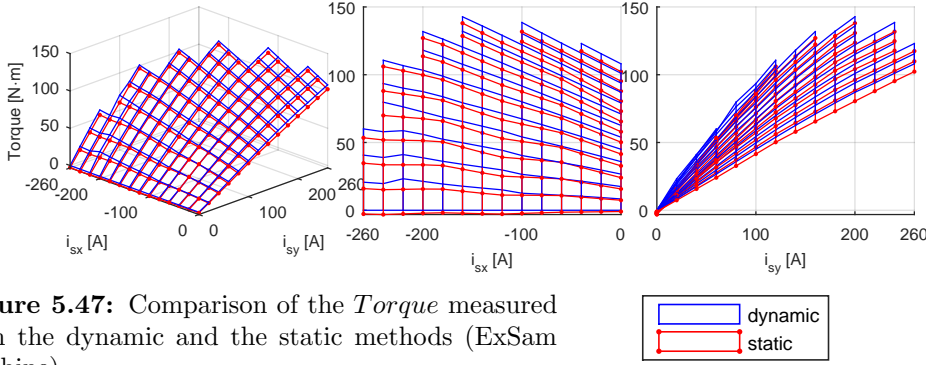


Figure 5.47: Comparison of the *Torque* measured with the dynamic and the static methods (ExSam machine)

The currents in these figure are the reference currents. The actual measured current has been measured but this data is not available by the time of writing this thesis. A variation of some Amps is expected to exist between the measured and the reference currents.

In (fig. 5.48) we can see the difference between both torque maps, which for most of the points is less than $6 [Nm]$. The largest measured torque is ca $140 [Nm]$. For some few points with large demagnetization current i_{sx} the difference is up to ca $10 [Nm]$.

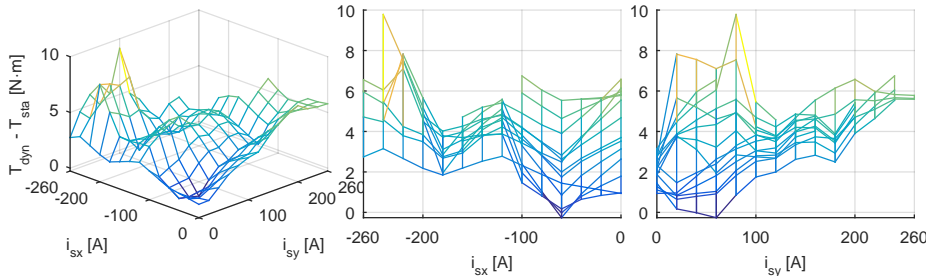


Figure 5.48: Difference of the *Torque* measured with the dynamic and the static methods (ExSam machine)

The project *ExSam* consists on developing a parallel hybrid drive train for a heavy vehicle, specifically a hybrid buss. Therefore the applied currents are larger as well as the obtained torque. Here currents up to a magnitude of $|\vec{u}_{s,xy}| = 260 [A]$ are applied and a larger flywheel is needed.

Chapter 6

Torque and speed control and machine properties

In the previous chapter the *EM* has been accelerated keeping the current point constant. Here it is desired to accelerate the *EM* from 0 to top speed of 15000 *rpm* ($f_{el}^{top} = 1000[Hz]$) letting the control system to pick up the most appropriate current points during the acceleration.

In order to be able to run above the nominal speed of 3000 *rpm* a *Field Weakening Control* system is implemented. The one here is based on the FWC described by (Jonas Ottosson in [28], ch. 7).

The method consist in first creating *Look Up Tables* that contain the optimal current point $[i_{sx} \ i_{sy}]$ for a given expected torque T and for the actual available flux $|\vec{\psi}|$, this is explained in more detail in the following sections. The *LUTs* do not need to be calculated in real time, for this thesis they have been calculated using *Matlab* from the torque and flux maps from the *EM*.

The maps are fed then in the real time control system that runs the *EM*, which calculates the flux from the actual speed ω_{el} and the actual available dc-link voltage u_{dc} and then makes a 2D interpolations from the data in the *LUTs* to obtain the values for the needed current. This is done in the *FPGA* at high iteration rate at every 102.4 [us].

Later an acceleration sequence using this *Field Weakening Control* system is shown.

6.1 Calculation of the look-up-tables for field weakening

6.1.a The iso-torque lines

In (fig. 6.1) we can see the *Torque Map* as contour or iso-torque lines, i.e. any point on each line produces the same torque. At low speeds the most natural choice is to pick up the point that lies closest to the origin, i.e. the one that requires less current and so produces the lowest resistive losses. At higher speeds the flux is also considered.

In (fig. 6.1) the nominal current vector \vec{i}_0 is also plotted, which is the current point that delivers the specified nominal torque with lowest resistive losses. \vec{i}_0 plays an important roll in the creation of torque speed diagrams (table 6.1)

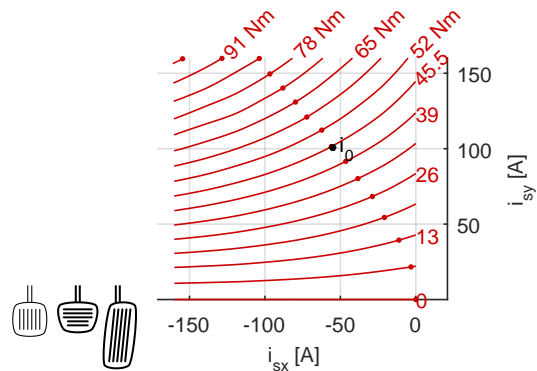
Table 6.1: Nominal current vector

| | | | |
|-----------------|----------|----------|-----------------------------|
| T_{nom} : | 45 | Nm | specification (table 3.1) |
| \vec{i}_0 : | [-54.753 | 100.917] | A optimal $\vec{i}(45Nm)$ |
| $ \vec{i}_0 $: | 114.814 | A | |

The torque map is symmetric along the i_{sx} -axis. If a negative torque is required for example for braking or for accelerating in the negative direction only the sign of i_{sy} need to be changed.

As an analogy to vehicles with combustion engines, the capability of selecting torque would correspond to the gas pedal; and of course the brake and reverse for negative torques.

Figure 6.1: Torque lines [Nm], optimal points and the nominal current point \vec{i}_0 . Selecting torque level is similar to applying different pressure on the gas pedal on a conventional car; as well as the brake and reverse.



6.1.b The flux linkage $|\vec{\psi}|$

With increasing speed the required voltage $|u_{sx} \ u_{sy}|$ will increase. Specially the last term in (eq. 5.5) which is the induced voltage $|\vec{e}|$:

$$\vec{e} = \omega_{el} \begin{bmatrix} 0 & -1 \\ 1 & 0 \end{bmatrix} \vec{\psi} = \omega_{el} \begin{bmatrix} -\psi_{sy} \\ \psi_{sx} \end{bmatrix}$$

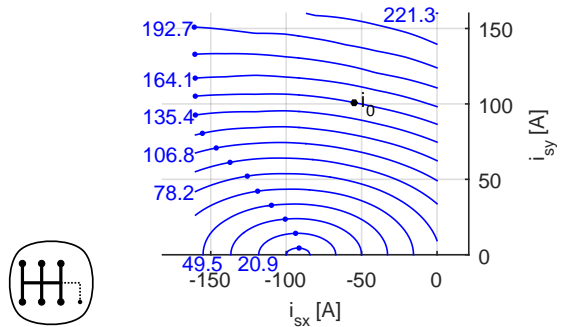
Considering that the induced voltage depends also on the flux and as explained in (section 3.3.h), to be able to increase speed while keeping the voltage down, current points with lower flux need to be chosen.

In figure (fig. 6.2) we can see contour ellipses with different magnitudes of the flux linkage $|\psi|$. These ellipses are concentric around the demagnetization point. For a given dc-link-voltage u_{dc} , every ellipse corresponds to a certain speed. The larger ellipses correspond to lower speeds and the smaller ones to high speeds.

This possibility of selecting regions with lower flux to be able to reach higher speed can be consider similar to the function of a gear box in a vehicle with combustion engine.

Figure 6.2: Flux $|\psi|$ ellipses [mVs]. Max torque at the dots.

Selecting them is similar to using the gearbox on a conventional car. Smallest ellipse allows higher speeds but at lower torque.



6.1.c The required *dc-link voltage* u_{dc}

The required *dc-link voltage* is calculated as in (section 3.3.d). First the nominal induced voltage $|\vec{e}_0|$ according (eq. 3.9) or (eq. 6.1) is calculated, there $\omega_{0,elec}$ corresponds to the specified nominal speed and $|\vec{\psi}_0|$ is the flux at the nominal current point \vec{i}_0 .

$$|\vec{e}_0| = \omega_{0,elec} \cdot |\vec{\psi}_0| \quad (6.1)$$

The required dc-link voltage to handle the induced voltage, when *Symmetric PWM modulation* is used, is according (eq. 3.10 or eq. 6.2):

$$U_{dc,min,e} = \sqrt{2} |\vec{e}_0| \quad (6.2)$$

Of course, the recommended minimal *dc-link voltage* should have a safety marginal to handle resistive and inductive voltage drop as well as other voltage variations as f.ex. the ones caused by the cogging.

$$U_{dc,min,rec} = (1 + k_{safe}) \sqrt{2} |\vec{e}_0| \quad (6.3)$$

The values are presented in (table 6.2)

Table 6.2: Induced and required dc-link voltage

| | | | |
|---------------------|-------------------|--------------|--|
| $\omega_{0,elec}$: | 1333.33 | <i>rad/s</i> | (table 3.3) |
| $f_{0,elec}$: | 212.207 | <i>Hz</i> | |
| \vec{i}_0 : | [-54.753 100.917] | <i>A</i> | (table 6.1) |
| $\vec{\psi}_0$: | [30.846 146.629] | <i>mV s</i> | interpolation of $\vec{\psi}$ at \vec{i}_0 |
| $ \vec{\psi}_0 $: | 149.839 | <i>mV s</i> | |
| $ \vec{e}_0 $: | 199.785 | <i>V</i> | (eq. 3.9) |
| $u_{dc,min,e}$: | 282.538 | <i>V</i> | (eq. 3.10) |
| k_{safe} : | 10 | <i>%</i> | |
| $u_{dc,min,rec}$: | 311 | <i>V</i> | (eq. 6.3) |

Every flux line correspond to a certain speed for a given dc-link voltage. The corresponding speeds for the dc-link voltage in (table 6.2) are presented in (table 6.3).

NOTE: While the relations between the torque and flux maps to the current points are very strong for a given *EM*, the speed and then the power depend on a external factor which is the dc-link voltage, i.e. the nominal speed and the nominal power could be for ex. doubled by just doubling the *dc-link voltage*. Of course consideration should be taken to the isolation in the windings. Even if the nominal speed is increased, the top speed may remain unchanged due to mechanical and control limitations. The torque and flux maps are not totally unchangeable but are, for instance, temperature dependent.

Table 6.3: f_{el} and speed for different $|\vec{\psi}|$

| | | | | | | | | |
|-----------------|----------|-------------|-------------|-------------|-------------|--------------|-------------|-------------|
| | ψ_1 | ψ_2 | ψ_3 | ψ_4 | ψ_5 | ψ_6 | ψ_7 | ψ_8 |
| $ \psi [mV s]$ | 221.3 | 207.0 | 192.7 | 178.4 | 164.1 | 149.8 | 135.4 | 121.1 |
| $f_{el} [Hz]$ | 144 | 154 | 165 | 178 | 194 | 212 | 235 | 263 |
| $[rpm]$ | 2155 | 2304 | 2475 | 2674 | 2907 | 3185 | 3522 | 3938 |
| | ψ_9 | ψ_{10} | ψ_{11} | ψ_{12} | ψ_{13} | ψ_{14} | ψ_{15} | ψ_{16} |
| $ \psi [mV s]$ | 106.8 | 92.5 | 78.2 | 63.8 | 49.5 | 35.2 | 20.9 | 6.6 |
| $f_{el} [Hz]$ | 298 | 344 | 407 | 498 | 642 | 903 | 1523 | 4849 |
| $[rpm]$ | 4466 | 5158 | 6103 | 7472 | 9632 | 13551 | 22846 | 72740 |

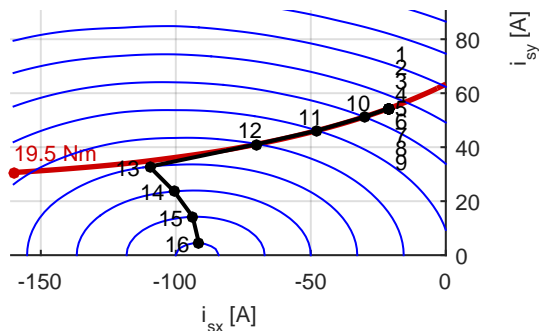
6.1.d Selection of appropriate current points

The outcome is to create two tables, one for i_{sx} and one for i_{sy} as a function of torque and flux values. In this case two $16T \times 16|\vec{\psi}|$ tables are created. The table size of $16 \times 16 = 256$, which is quite low is chosen considering the limited memory of the *FPGA*. The tables contain the optimal current point for all combinations of torque and flux within the measured range.

A set of 16 torque levels are selected from $0[Nm]$ to the highest torque level in the torque map, here it is $97.5[Nm]$, as well as a set of flux levels, from $221.3[mV s]$ to $6.6[mV s]$.

The process is explained in the following lines using the values in (fig. 6.3) as an example.

Figure 6.3: Selection of optimal current points at for ex. the 4:th torque line



One torque level is selected at a time. For ex. in (fig. 6.3) the 4:th torque line for $T = 19.5[Nm]$ is shown.

The second step is to select a flux ellipse. Only the section of the actual torque

line that lies inside the area delimited by the ellipse is considered.

The point on this section that lies closest to the origin is selected, i.e the one with lowest current magnitude $|\vec{i}|$ and therefore also lowest resistive losses.

- **Torque for less current:** For large flux values, points 1 to 9 in (fig. 6.3) the optimal point is the same, it is the point of the torque line that lies closest to the origin at all.
- **Sustained Torque:** In the cases of points 10, 11 and 12, the ellipses have become so small, that the selected current are touching the actual ellipse border and must be moved to the left. Here the Torque is still kept but the resistive losses begin to increase caused by the larger magnitude of the current. i.e. points 10, 11 and 12 deliver the same torque as points 1 to 9 but with reduced efficiency, on the other hand at points 10, 11 and 12 it is possible to reach higher speeds.
- **Torque drop att high speeds:** In case of points 13 to 16, the ellipses are so small that the torque line is totally outside the them. Here the selected points are the points on the respective ellipse curve that delivers highest torque. For these points not only efficiency is sacrificed to reach higher speed but also torque.

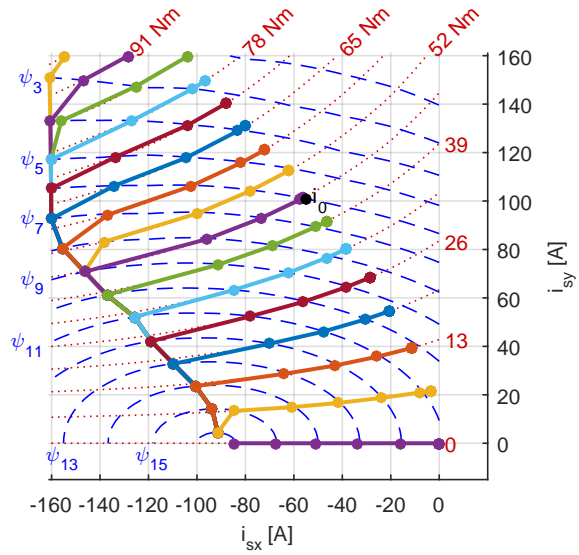
In this way for every desired torque level a path on the $i_{s,xy}$ -plane is selected.

The process is repeated for all selected torque levels.

In (fig. 6.4) we can see all selected optimal current points on the $(i_{sx} \ i_{sy})$ -plane for all combinations of selected torque and flux. The paths corresponding to different desired torque levels are drawn with different colors.

All the values are presented in (tables B.10 and B.11).

Figure 6.4: Complete Look up table

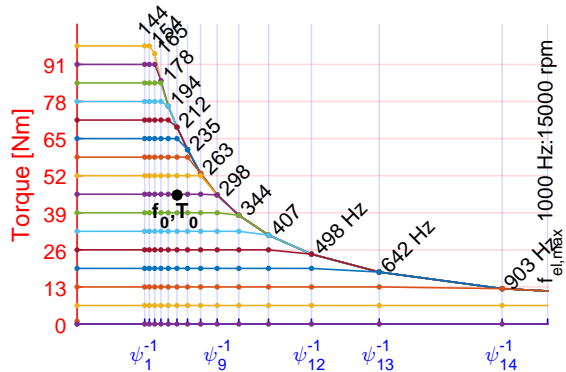


Considering that every point in (fig. 6.4) corresponds to a combination of torque and flux, and that every flux corresponds to certain speed for a given dc-link voltage. These points, and so the paths, are redrawn in a torque speed diagram in (fig. 6.5). There we can see the obtained torque for every desired torque level depending on speed.

Figure 6.5: Highest possible torque for different flux ψ values. Example speeds according to (table 6.3)

$$f_{el,0} = 212 [Hz] : 3183 [rpm]$$

$$T_{nom} = 45 [Nm]$$



In (fig. 6.6) we can see the current values of the i_{sx} and i_{sy} in the LUTs as a function of torque and flux.

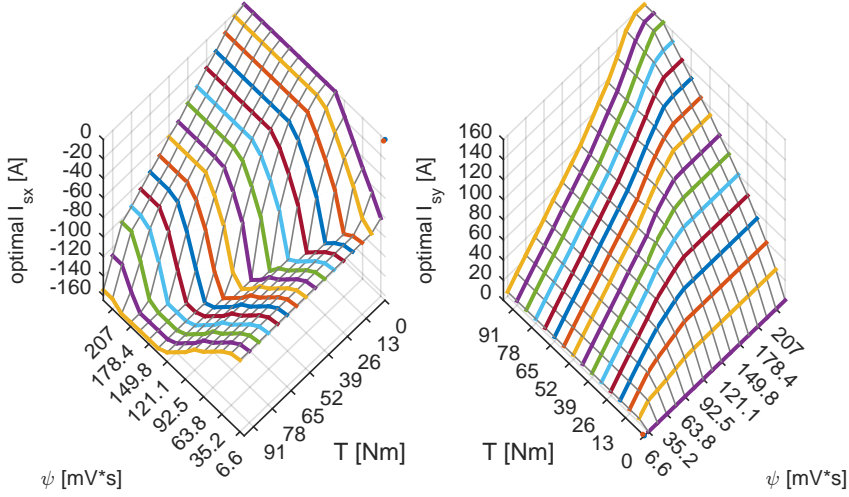


Figure 6.6: Optimal current for all combinations of torque and flux

6.1.e Implementation of look-up-tables in the control system

The *Look Up tables (LUTs)* are saved in a text file containing $16+16+256+256$ values in a single long array and uploaded to the FPGA at start of the tests.

- 16 flux values in $[V s]$, in descendant order $[2.21 \cdot 10^{-1} \dots 6.65 \cdot 10^{-3}]$
- 16 torque values in $[Nm]$, in ascendant order $[0 \dots 91]$
- 16×16 values for i_{sx} , with ψ iterating faster than T
- 16×16 values for i_{sy} , with ψ iterating faster than T

The *Field Programmable Gate Array (FPGA)* has very limited memory and flexibility. Therefore only a 16×16 resolution is used for input the data.

The flux is calculated in the *FPGA* from the instantaneous value of the *dc-link-voltage* and speed with a safety marginal. The torque is the output of the speed controller running also on the *FPGA*.

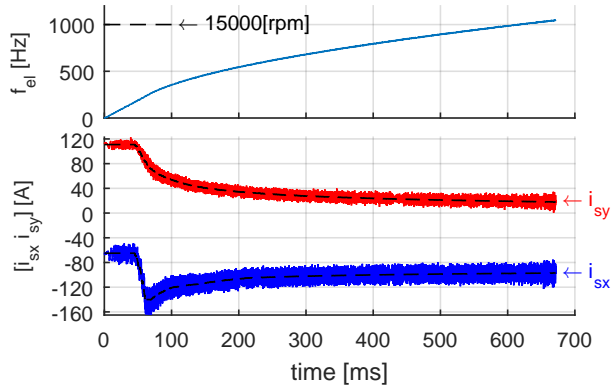
The flux and the torque have much higher resolution than those 16 different values. To compensate for that a 2D-linear interpolation is performed in the *FPGA* to determine the exact required current vector $[i_{sx} \ i_{sy}]$.

This process is repeated for every switching period, in this case every $\Delta t_{sw} = 102.4[s]$

6.1.f Acceleration using the look-up-tables for field weakening

In (fig. 6.7) we can see a real acceleration using the *LUTs* for *Field Weakening* where we can see the speed and the applied current over time. The acceleration goes from 0 to over the top speed $f_{el,top} = 1000 [Hz]$ which corresponds to $15000 [rpm]$.

Figure 6.7: Acceleration using the Look Up tables

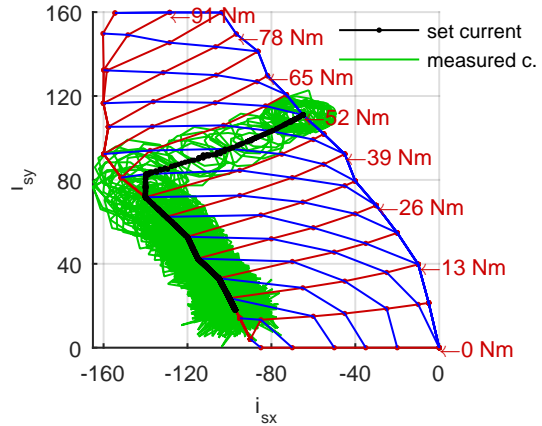


In (fig. 6.8) the currents for the same acceleration are shown in the $i_{s,xy}$ -plane.

The Look Up Tables used in this acceleration (fig. 6.8) are slightly older than the new LUTs in (fig. 6.4) but both are made from the same torque and flux maps. The new one has upgraded methods for interpolation and finding optimal points and the table becomes smoother.

As we can see, the sequence starts with a strong acceleration with constant current at the selected torque, followed by a strong demagnetization, and finally the currents go towards the *Demagnetization Point* with reduced torque.

Figure 6.8: Automatically selected current points during acceleration using *LUTs*



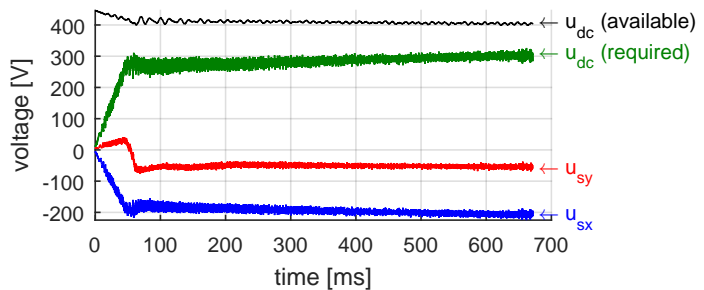
In (fig. 6.9) we can see the voltage values during the acceleration: the components of $\vec{u}_{s,xy}$, the calculated required dc-link voltage for this voltage

$$u_{dc,required} = \sqrt{2} |\vec{u}_{s,xy}|$$

and the actual available measured dc-link voltage $u_{dc,available}$. For this acceleration the control system is set to limit the required dc link voltage around 300 V even if the available dc link voltage is above 400 V, to keep a good marginal during the experiment.

As we can see, at the beginning, the voltage increases linearly with speed but then the *Field Weakening* prevents the voltage from continue increasing.

Figure 6.9: voltage under acceleration



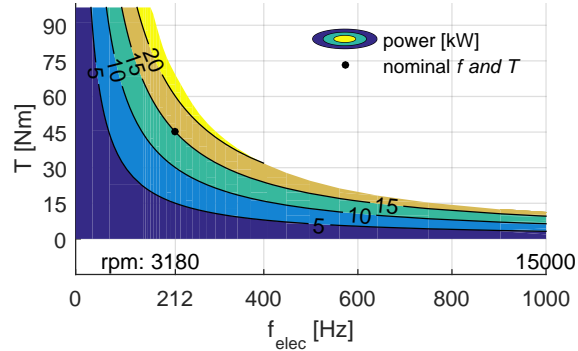
6.2 Properties of the electric machine: power, losses, efficiency

In (figure 6.10) we can see the mechanical power for the *EM*, running in *motor mode*, for different combinations of Torque and Speed, basically

$$P_{mech} = T_{feasible} \cdot \omega_{mech}$$

As seen in (figure 6.5) the reference torque can not be sustained for higher speeds, this drop in the torque implies a limit in the maximal possible power. In (figure 6.10) we can also see the maximal feasible power that the *EM* can deliver for the dc-link voltage in (table 6.2).

Figure 6.10: Mecanical Power produced by the *EM*



The nominal power, torque and speed and the corresponding dc-link voltage are presented in (table 6.4)

Table 6.4: Nominal values for the Prototype

| | | | |
|----------------|---------|------------|---------------------------|
| P_{nom} | 15 | <i>kW</i> | specification (table 3.1) |
| T_{nom} | 45 | <i>Nm</i> | specification (table 3.1) |
| $speed_0$ | 3180 | <i>rpm</i> | (table 3.1) |
| $f_{0,elec}$ | 212.207 | <i>Hz</i> | (table 3.3) |
| $u_{dc,min,e}$ | 282.538 | <i>V</i> | (table 6.2) |

The power losses are calculated from the resistance and the friction which are considered the largest causes of power loss. The losses created by the magnetic hysteresis or iron losses P_{fe} (see table 3.13) could not be clearly measured (see fig. 5.19) and no further investigation of other kind of losses is done in this thesis.

In general measuring the losses is not simple task, often certain kinds of losses are very small compared to the nominal power, the accuracy is often affected by the calibration of the measurement instruments and more long term methods as for ex. calorimetry methods use to be recommended.

But the losses registered using the *dynamic test method*, which should cover the largest sources of loss, are calculated as:

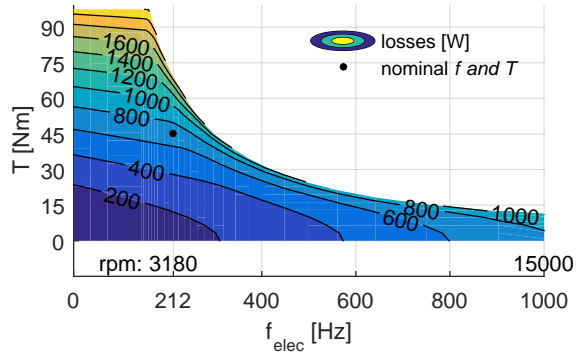
$$P_{loss} = R \cdot |\vec{i}_{s,xy}|^2 + T_{friction} \cdot \omega_{mech}$$

Table 6.5: Values uses for the loss calculation

| | | | |
|------------------|------|-----------|-------------|
| R : | 42.6 | $m\Omega$ | (table 5.3) |
| $T_{friction}$: | 0.41 | Nm | (table 5.6) |

and presented in (figure 6.11)

Figure 6.11: Friction and resistive losses

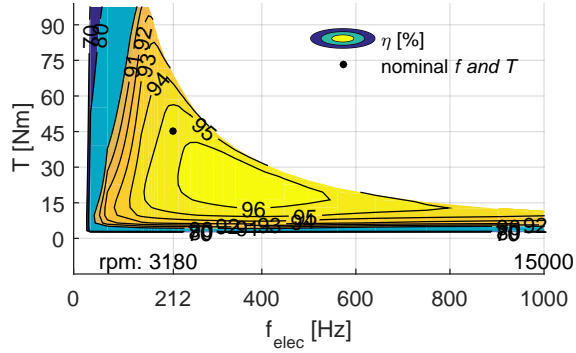


Then the efficiency η of the *EM* in motor mode is calculated as:

$$\eta = \frac{P_{mech}}{P_{mech} + P_{loss}}$$

and displayed in (figure 6.12)

Figure 6.12:
Efficiency η



The efficiency at the nominal working conditions is 95% and is 96% for a slightly higher speed, this efficiency level is typical for *inserted Permanent Magnet Synchronous Machines (iPMSMs)* and could be increased by increasing the dc-link-voltage and running at higher speeds.

6.2.a The resistance, inductances, and the magnet flux linkage Ψ_m

The resistance R_s of the EM is calculated from dynamic measurements by analyzing the relation between the voltage and the current.

The Inductances L_{sx} , L_{sy} are calculated from the slope of the flux over the current at the origin. For other current values it is better to use the very value of flux for control or characterization of the EM than calculating the inductances.

The flux linkage ψ_m is calculated as the x-component of the flux at $i_{sx} = 0$, $i_{sy} = 0$ i.e the flux linkage generated only by the magnets.

These values are presented in (Table 6.6)

Table 6.6: Resistance, inductances and flux linkage of the EM

| | | | | |
|----------|---|--------|------------------|-----------------------------|
| R_s | = | 42.6 | [$m\Omega$] | at 22 °C, (table 5.3) |
| L_{sx} | = | 0.8314 | [mH] | at $i_{sx} = 0, i_{sy} = 0$ |
| L_{sy} | = | 1.5081 | [mH] | at $i_{sx} = 0, i_{sy} = 0$ |
| Ψ_m | = | 76.784 | [$mV \cdot s$] | at 22 °C |

6.3 Gear shift synchronization

As mentioned before, one of the main tasks of the customized *Electric Machine (EM)* is to synchronize the *gearbox input shaft* during gearshift in a fraction of a second (see eq. 2.1).

$$\Delta t_{sync,max} = 100[ms]$$

In a previous study [18] calculation of the synchronization time has been done using theoretic nominal values of the torque and power of the *EM*. Here the synchronization time is studied using actual measured data from the *EM* and considering the extended power capability of the *iPMSM*.

The gearbox used for tests and as reference is a "Xtrac '416' Front Wheel Drive Touring Car gearbox" which is a sequential manual gearbox. The gear ratios are displayed in (table 6.7)

Table 6.7: Gear ratios of the sequential gearbox

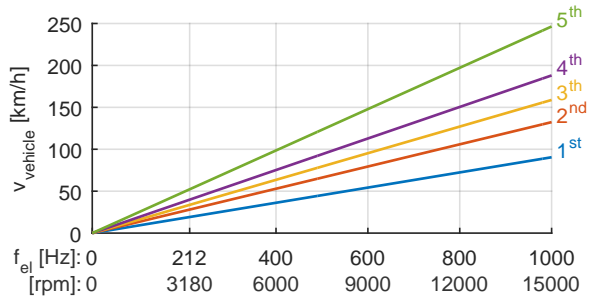
| gear | 1 st | 2 nd | 3 th | 4 th | 5 th | 6 th |
|---|-----------------|-----------------|-----------------|-----------------|-----------------|-----------------|
| $k_{gear,i} = \frac{\omega_{in}}{\omega_{out}}$ | 9.875 | 6.750 | 5.625 | 4.750 | 3.625 | 4.125 |

Table 6.8: *iPMSM*-wheel transmission data

| | | |
|---------------------------|-------|-------|
| ω_{EM}/ω_{in} | 2 | |
| r_{wheel} | 0.316 | [mm] |
| P_{nom} | 15 | [kW] |
| T_{nom} | 45 | [N m] |
| $f_{el,nom}$ | 212 | [Hz] |

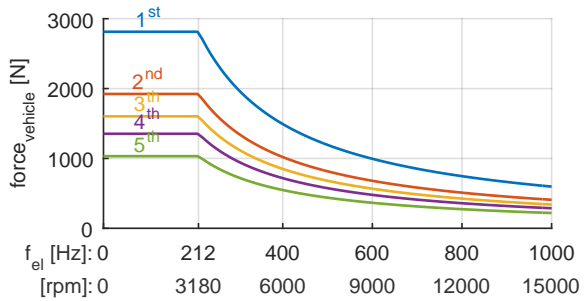
Considering the gear ratios and the speed ratio between the *iPMSM* and the input shaft, and assuming a typical car wheel radius, the relation between the vehicle linear speed and the angular speed of the *iPMSM* is calculated (figure 6.13). The wheel radius is taken from a wheel with dimensions (205/55R16) used in for ex. a small car (Volvo V40).

Figure 6.13: vehicle linear speed vs. the angular speed of the *EM* for different gears



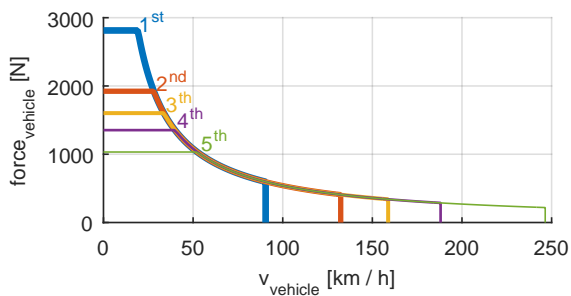
The corresponding linear force that the *EM* can deliver to the wheels under nominal conditions, at different angular speeds of the *iPMSM*, and for different gear ratios is displayed in (figure 6.14). Friction is not considered.

Figure 6.14: linear force on the wheels delivered by the *EM* at different angular speeds for different gears



The linear force on the wheels that can be delivered by the *iPMSM* vs. the vehicle speed if displayed in (figure 6.15). This shows the force-speed characteristic when driving for example in pure electric in city traffic, which is actual up to for.ex 50 km/h . For higher speeds where more power is needed the *Internal Combustion Engine (ICE)* need to be main power source. But the *iPMSM* can still contribute with the nominal power and be used for regenerative braking.

Figure 6.15: force on the wheels delivered by the *EM* vs the vehicle linear speed



As we can see in (figure 6.15), at very low speed only the first gear is to be used, but as the speed increases, other gears will also deliver the same force and power to the car, with overlapping speed regions.

The speed at which the gear shift will happen depend on the driving mode, if it is pure electric drive, or to get the best efficiency of the *ICE*, or to minimize the gearshift synchronization time. these points will be studied in the following lines.

6.3.a Calculation of the synchronization time

During gearshift the speed of the vehicle can be assumed to be constant because of the short duration of the gear shift with respect to the vehicle dynamics [50]. Consequently the angular speed of the output shaft is considered to remain also constant. On the other hand the angular speed of the input shaft, and then the frequency of the *EM* need to adapt to the new gear ratio. For ex. when gear shifting from from 1st gear to 2nd gear, the electric frequency of the *iPMSM* need to go down from

$$f_{el,1}$$

to

$$f_{el,2} = \left(\frac{k_{gear,2}}{k_{gear,1}} \right) \cdot f_{el,1} \quad (6.4)$$

with the values in (table 6.7)

$$f_{el,2} = \frac{6.750}{9.875} \cdot f_{el,1} = 0.6835 f_{el,1}$$

The time required for the *iPMSM* to go from one frequency to other is calculated by solving the differential equation

$$T = J \frac{d\omega_{mech}}{dt} \quad (6.5)$$

Here the torque T is constant at low speeds up to f_{nom} and then decreasing with increasing f_{el} at the *Constant Power Speed Range (CPSR)*. For the inertia J here it is considered only the inertia of the rotor. The reflected inertia of the input shaft and the belt transmission are not considered at the beginning

because of the different values it can have and that the synchronization time is going to be affected linearly with the effect of the reflected inertia.

At constant torque T^* the solution of the differential equation (eq. 6.5) is:

$$\int_{t_1}^{t_2} dt = \frac{J}{T^*} \int_{\omega_{mech,1}}^{\omega_{mech,2}} d\omega_{mech}$$

$$\Delta t_{sync} = \frac{J}{T^*} (\omega_{mech,2} - \omega_{mech,1})$$

with (eq. 6.4)

$$\Delta t_{sync} = \frac{J}{T^*} \left(\frac{k_{gear,2}}{k_{gear,1}} - 1 \right) \omega_{mech,1}$$

i.e. at constant torque, the synchronization time Δt_{sync} is proportional to the rotor speed ω_{mech} .

$$\implies \Delta t_{sync} = const \cdot \omega_{mech,1} \quad (\text{at constant torque})$$

At constant power, for ex at nominal power

$$P_{nom} = \omega_{mech} \cdot T$$

(eq. 6.5) becomes

$$T = \frac{P_{nom}}{\omega_{mech}} = J \frac{d\omega_{mech}}{dt}$$

and its solution is

$$\int_{t_1}^{t_2} dt = \frac{J}{P_{nom}} \int_{\omega_{mech,1}}^{\omega_{mech,2}} \omega_{mech} d\omega_{mech}$$

$$\Delta t_{sync} = \frac{J}{2 P_{nom}} (\omega_{mech,2}^2 - \omega_{mech,1}^2)$$

$$\Delta t_{sync} = \frac{J}{2 P_{nom}} \left(\left(\frac{k_{gear,2}}{k_{gear,1}} \right)^2 - 1 \right) \omega_{mech,1}^2$$

i.e, Δt_{sync} is proportional to the square of rotor angular speed.

For the more general cases, when the torque is given as a function of the speed, $T = T(\omega_{mech})$, as for example, when the torque speed characteristics are obtained from *Finite Element Analysis (FEA)* or measurements, the differential equation

$$T(\omega_{mech}) = J \frac{d\omega_{mech}}{dt}$$

is solved by numerically integrating

$$\int_{t_1}^{t_2} dt = J \cdot \int_{\omega_{mech,1}}^{\omega_{mech,2}} \frac{1}{T(\omega_{mech})} d\omega_{mech}$$

with (eq. 6.4)

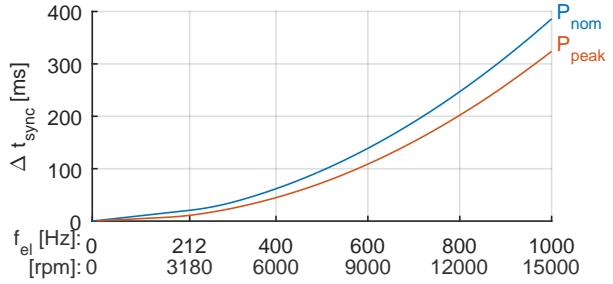
$$\Delta t_{sync} = J \cdot \int_{\omega_{mech,1}}^{\left(\frac{k_{gear,2}}{k_{gear,1}}\right)\omega_{mech,1}} \frac{1}{T(\omega_{mech})} d\omega_{mech} \quad (6.6)$$

In (figure 6.16) we can see the calculated synchronization time when shifting from gear 1 to gear 2, in two cases, one using nominal torque and nominal power and the other using the highest available peak power (see figure 6.5).

During gear shift from 1^{st} gear to 2^{nd} gear the *iPMSM* decelerates from $f_{el,1}$ to $0.6835 f_{el,1}$. For that the torque is applied with negative sign. For gear shift from 2^{nd} gear to 1^{st} gear the *iPMSM* is accelerated instead and the time is in principle the same, when neglecting the contribution of the friction.

Nominal torque and nominal power is the highest limit for long term continuous operation to avoid overheating of the *EM*. Overrated peak power P_{peak} can be used under very short time intervals, like here during fractions of a second, only to synchronize gears. This is a good example of the advantages of the overrating capabilities of the *iPMSM*.

Figure 6.16: Synchronization time vs. f_{el} at 1^{st} gear
 $1^{st} \text{ gear} \leftrightarrow 2^{nd} \text{ gear}$
 $f_{el,1} \leftrightarrow 0.6835 f_{el,1}$



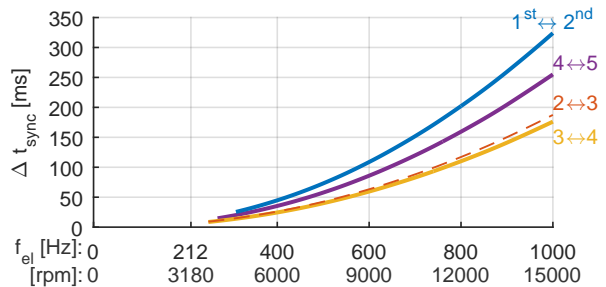
When shifting gears between $1^{st} \text{ gear} \leftrightarrow 2^{nd} \text{ gear}$ using peak power as in (6.16), the required synchronization time according to the specifications in (eq. 6.7) of

$$\text{maximal allowed } \Delta t_{sync} = 100 [ms] \quad (6.7)$$

is reached for speeds up to $f_{el} = 580 [Hz]$ or $speed_{EM} = 8700 [rpm]$. This speed of the *iPMSM* corresponds to an angular speed of the *ICE* $speed_{ICE} = 4350 [rpm]$, which lies above the optimal speed of the *ICE* for optimal fuel efficiency. I.e. under normal driving conditions the gear shift between $1^{st} \text{ gear} \leftrightarrow 2^{nd} \text{ gear}$ will happen at lower speeds.

In (6.17) we can see the synchronization time for gear shifting between other gears, using peak power. Due to the lower difference in gear ratio between the other higher gears the synchronization time is much lower and the time limit of $100 [ms]$ can be achieved for even higher speeds. In this figure curves are not drawn for very low speed, the reason for that is explained in the following lines.

Figure 6.17: Synchronization time vs f_{el} at the lower gear of each pair.
 $P = P_{peak}$



6.3.b Speed limits for gearshifting

Shifting gears at too high speeds will not only extend the synchronization time but when shifting gears down, considering that the *iPMSM* and the *ICE* go to a higher speed, the highest speed at which the synchronization process can be started should be accounted in order to avoid running the *iPMSM* and the *ICE* over their top speed.

In (figure 6.18) we can see the speed of the *iPMSM* as a function of the vehicle speed for different gears. The polygons mark the speeds at which it is allowed to shift gears between two consecutive ones.

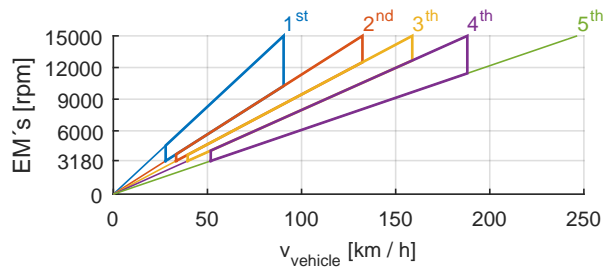
There is also a lower limit at which *up gear shifting* is recommended. The speed of the *iPMSM* after synchronization should be higher than the nominal speed to be able to continue deliver the nominal power from the *iPMSM* (see figure 6.15). This is relevant specially if the nominal power will still be required after *up gear shifting*, for example if the vehicle is running on pure electric mode. In (figure 6.19) we can also see that the the lowest speed for recommended gear shift have a synchronization time below the limit of

$$\Delta t_{sync, max} = 100 [ms]$$

.

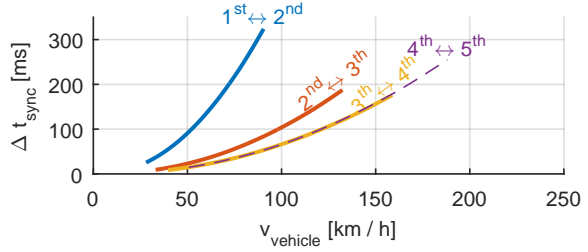
If for ex. after gear shifting the *ICE* will be the main power source instead of the *EM*, it is less relevant that the *EM* has reached the *Constant Power speed Range*. This lower speed limit is also marked in (figure 6.18).

Figure 6.18: Allowed speed range for gear shifting



The synchronization time as a function of the vehicle speed is shown in (figure 6.19). The curves are only drawn in the region where gearshift is recommended.

Figure 6.19: Synchronization time vs vehicle speed. P_{peak}



6.3.c Suggested methods to improve the synchronization time

The synchronization time can be reduce by:

- using a sequential gear box with geometric distributed gear ratios, i.e $k_{gear,2} = k_{gear,1}^2$, $k_{gear,3} = k_{gear,1}^3$, etc. There it would take the same time to gear shift between 1st gear ↔ 2nd gear as between 2nd gear ↔ 3th gear and so on.
- increasing the number of gears to 7 or 8 gears instead of the 5 ones used here. (the 6th gear is not used here)
- increasing the *dc-link-voltage*, which would increase the speed for any torque level, increasing in this way the nominal and peak power. In this case consideration should be taken to the isolation of the windings. During the experimentation with the *iPMSM* the dc-link-voltage has been increased to 450V. For higher voltages consideration should also be taken to the *Electromagnetic Interference* created by the *PWM* switching in the *Power Electronics Converter (PEC)*. During test with ca 750 V dc-link, interference in the measurements signals were observed with not well shielded *EMs*

But with the equipment used in this thesis the peak power of the *iPMSM* and the low inertia of the rotor are good enough to synchronize the input shaft during gear shift within the specified time limit, under normal driving conditions of a vehicle. This is one of the main characteristics of this customized *iPMSM* together with the speed, torque and power capabilities needed for a hybrid vehicle.

Chapter 7

Conclusions and suggestions for future work

7.1 Conclusions

This thesis work spans over a wide range, from gearbox control in hybrid vehicles, electric machine design, control system development and dynamic testing of *EMs*. The results of all these steps are then integrated with each other into a robust and well tested technical contribution to electric hybrid vehicles technology:

- It is possible to design a *iPMSM* for an *electric hybrid vehicle* using tools that are accessible by students as *FEMM*, *RF-Design* and *Matlab*
- The prototype of the *iPMSM* match very well the previous numerical simulations and fulfill the torque specifications for powering the vehicle and starting the *ICE*
- The *Dynamic Test Method* can be used to obtain the necessarily electromagnetic properties of the *iPMSM* with good precision and improved accuracy without the need of a *Brake Bench*
- It is possible to implement *Field Weakening* motor control on the *iPMSM* to reach speeds many times the nominal speed, up to 15000 [rpm]. The field weakening look up tables are created from torque and flux maps obtained using the *Dynamic Test Method*
- The *iPMSM* has good enough dynamics, i.e. can change speed fast enough

to synchronize gears under the specified time interval under normal conditions of vehicle drive.

7.2 Suggestions for Future Work

- Mapping the *iPMSM* using the other three rotors. Only the *symmetric, hot-side out* has been mapped (sections 3.6.a and 3.6.b).
- Perform thermal test on the prototype of the *iPMSM* to determine the nominal current and heat generation caused by *Cu-losses* and *Fe-losses*. Thermal tests without *Brake Bench* have been realized on other *iPMSM* using the the control system developed for this thesis. [7] and ([51] pg. 87).
- Mapping the *iPMSM* at different temperatures.
- Acceleration sequences of the *large 'vehicle' flywheels* through all gears in the gearbox using the new customized *iPMSM*. Some gear shift sequence tests were realized with the new *iPMSM* at *Division of Industrial Electrical Engineering and Automation (IEA)*'s lab and later more similar sequence tests were performed within the project *ExSam* with another *iPMSM* specified for a heavy vehicle at *Sibbhultsverken* [52], [53] and [12].
- Expand the *Dynamic Test Method* to other kinds of *EMs*, as *EMSM* and *Induction Machines*
- Expand the *Dynamic Test Method* to higher levels of power, torque and speed. The levels reached until now are ca. 150 [Nm], 15000 [rpm] and 20[kW].
- Further develop the *AFE* and integrate it to the *Dynamic Test Method*.
- Create a real time models of *EMs* on the the *FPGA* to be able to run a control and measurement sequence on a simulated *EM* before a real one is connected
- Further investigate the effect of speed on the the properties of the *EMs*. The *iPMSM* studied in this work has very low *eddy current losses* or *Fe-losses* that its effects are nor clear noticeable in the measurements.

Appendix A

Experimental setup

1.1 The equipment

The majority of experimental work has been done at the laboratory installations (see figure A.1) at the division *Division of Industrial Electrical Engineering and Automation (IEA)* at Lund University.



Figure A.1: The experimental setup with the *parallel drive bench*, the *control unit* and the *PC*

The experimental set up consists of:

- laboratory installations with ca 20kW, 400V DC supply
- The *inserted Permanent Magnet Synchronous Machine (iPMSM)* to be tested

- The *parallel drive bench* where the *iPMSM* is mounted
- motor control unit
- *PC*
- software for control and measurements of electric machines

The laboratory with enough space for running several project at the same time has access to a number of *DC power supplies* from rotating mechanical converters in the basement. The one used in this project can supply up to 20kW, 400V DC-power.

The *iPMSM* is mounted on the *parallel drive bench* used to simulate the drive train of a parallel hybrid vehicle, (see figure A.2 and A.3). This bench contains:

- the new *Electric Machine (EM)* which is a *iPMSM*
- the transmission belt
- a gearbox
- robot to control the a gearbox
- large flywheels to simulate the inertia of a vehicle

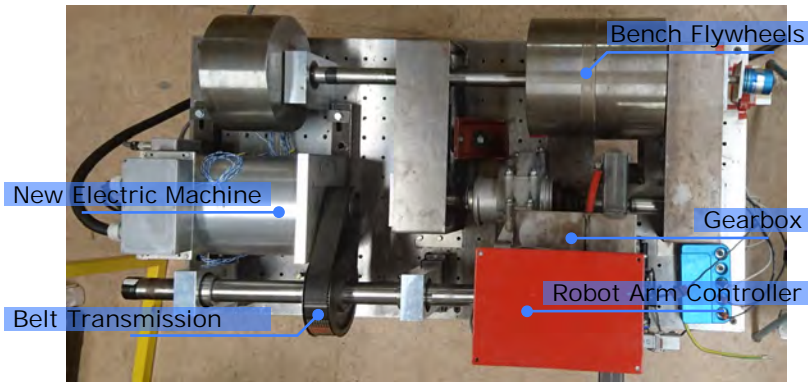


Figure A.2: Top view of the *parallel drive bench* with the *iPMSM* and other components



Figure A.3: The *parallel drive bench* with the *iPMSM*

The *parallel drive bench* has been used in previous projects as for.ex. [17] to test the dynamics of the whole drive train. But to be able to map only the *iPMSM* using the *Dynamic Test Method*, a simple test bench can be used, just to hold the *EM* in place. A safety cage is installed around the bench, to prevent parts flying out, in case something brake inside and also to prevent persons coming too close to moving parts and external objects accidentally coming into the bench.

In (figure A.4) we can see the *iPMSM* inside the cage on the bench, here the *iPMSM*, with a small flyweel on it, is not connected to the rest of the drive train.

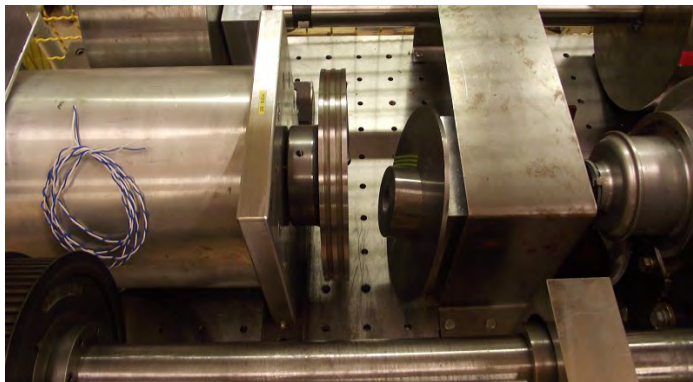


Figure A.4: Electric machine on the bench

1.2 The hardware

The control unit consists of:

- An embedded control unit, **CompactRIO** from *National Instruments* (figure A.5). It has an *Field Programmable Gate Array (FPGA)* used for the very time-critical calculations for current and speed control and a *Real Time (RT)* microprocessor for streaming measurement data to the *PC* and handling slower processes as the user interface. The *CompactRIO* contains also Digital and Analog modules to get and send the signals from and to the *Interface cards*. The *CompactRIO* is connected to the *PC* via ethernet
- **The Interface cards** are a set of *Printed Circuit Boards (PCB)* used to adapt signals between the sensors and the *Power Electronics Converter* to the *CompactRIO* (figure A.5)
- The **Power Electronics Converter** (figure A.6), contains the *IGBTs* that are used to control the amount of current to the *EM* by opening and closing the connection between the capacitor and the phases of the *EM* according to the *PWM* signals calculated in the *FPGA*. A simplified sketch of its functionality is shown in (figure 5.22).

Figure A.5: The control unit

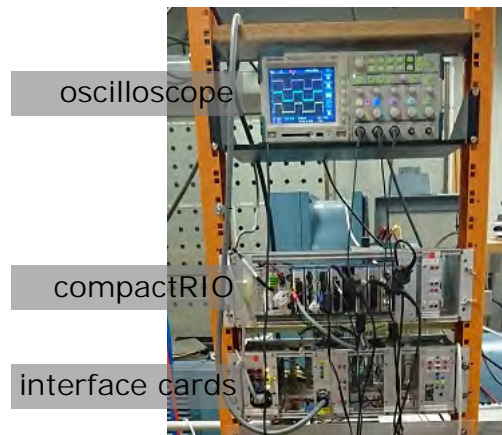
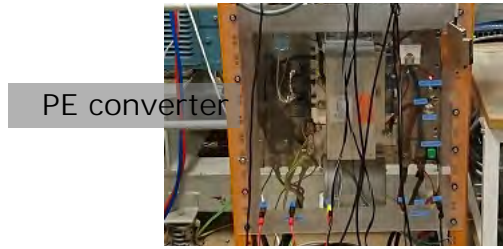


Figure A.6: The Power Electronics Converter



In (figure A.7) we can see an updated portable version of the *control unit*, that was delivered to *SP Technical Research Institute of Sweden* to test *iPMSMs* with the *Dynamic Test Method* in their facilities in Borås, Sweden.

Figure A.7: Portable control unit, with the *Interface cards* and the *CompactRIO*



and in (figure A.8) we can see the *Power Electronics Converter (PEC)* in the lower part the *Control Unit* as well as the interface cards and the *CompactRIO* on the upper part.

Figure A.8: Portable control unit, with the *PEC* shown in the lower part



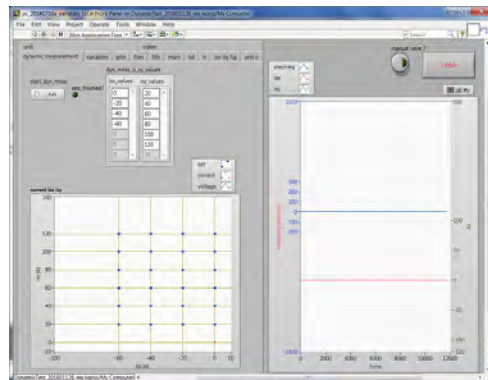
The *PC* is used as an interface with the user, to start and stop measurement sequences, input parameters, see values and graphs during and after operation. The *PC* is also used to save the large amounts of measurements data and for the post processing of it. As said before the *PC* is connected to the CompactRIO via ethernet.

1.3 The software

The Software for the control and measurement system running on the *FPGA* and the *Real Time* microprocessor in the *CompactRIO* and the *PC* interface has been written in *Labview* (figure A.9).

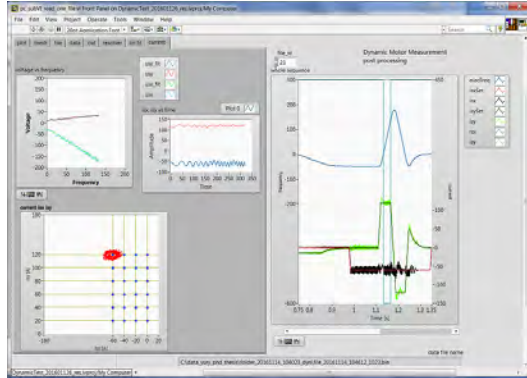
The post processing is programmed both in *Labview* and in *Matlab*.

Figure A.9: The *PC* interface of the Labview program



In (figure A.10) we can see the front panel of the labview file for post processing, showing the voltage, current and speed for a certain working point during the *Dynamic Test Method*.

Figure A.10: The front panel of the post processing file in Labview



Research Engineer Getachew Darge at *IEA* is responsible for the hardware design and implementation of the control units. The software in labview for the FPGA, RT in and the PC interface is developed by the author of this thesis Yury Loayza as well as the main idea of performing *Dynamic Test Method* the way it is described in this thesis.

Previously the control system used at the division *IEA* was implemented in *DSpace*, and the code was written in C-language and is described in [54]. The main structure of the algorithms for motor control in the Labview version are based on the version written for *DSpace*. The methods used for post processing the data with the torque and flux maps as well as the ones for motor design are based on the work of the advisors to this thesis, Avo Reinap and Mats Alaküla.

Appendix B

Data

2.1 Data from finite element analysis

Symmetric, hot-side-out rotor:

Table B.1: Nominal and peak current, and flux at i_0

| | T | x | y | magnitude | |
|---------------|---------|----------|---------|-----------|----------|
| i_0 | 45 [Nm] | -51.320 | 97.310 | 110.014 | [A] |
| i_{peak} | 90 [Nm] | -109.910 | 160.310 | 194.370 | [A] |
| $\psi_s(i_0)$ | 45 [Nm] | 41.155 | 141.301 | 147.173 | [mV · s] |

Table B.2: flux linkage in x

| | ψ_{sx} [mV · s] | | | | i_{sy} [A] |
|--------------|----------------------|--------|--------|--------|--------------|
| | -14.193 | 17.278 | 47.804 | 76.895 | 225 |
| | -16.905 | 15.879 | 47.973 | 78.705 | 200 |
| | -20.167 | 13.795 | 47.587 | 80.382 | 175 |
| | -23.872 | 10.960 | 46.462 | 81.552 | 150 |
| | -27.736 | 7.629 | 44.525 | 82.359 | 125 |
| | -31.405 | 4.361 | 42.314 | 81.899 | 100 |
| | -36.459 | 0.500 | 39.430 | 80.028 | 50 |
| | -37.926 | -0.526 | 38.517 | 79.181 | 0 |
| | -36.455 | 0.503 | 39.435 | 80.035 | -50 |
| i_{sx} [A] | -150 | -100 | -50 | 0 | |

Table B.3: Flux linkage in y

| ψ_{sy} [mV · s] | | | | i_{sy} [A] |
|----------------------|---------|---------|---------|--------------|
| 229.644 | 233.223 | 233.952 | 231.531 | 225 |
| 217.675 | 222.463 | 224.297 | 222.650 | 200 |
| 202.650 | 208.732 | 212.021 | 211.328 | 175 |
| 183.817 | 190.914 | 195.871 | 196.383 | 150 |
| 160.718 | 168.032 | 173.866 | 175.939 | 125 |
| 133.798 | 140.263 | 145.261 | 148.306 | 100 |
| 69.465 | 72.094 | 74.093 | 75.833 | 50 |
| 0.032 | 0.033 | 0.077 | 0.004 | 0 |
| -69.441 | -72.078 | -74.081 | -75.826 | -50 |
| i_{sx} [A] | -150 | -100 | -50 | 0 |

2.2 Data from the dynamic test method

Machine data for the configuration using the rotor with symmetric placed magnets and the *hot-side* out. Dynamic measurement performed using an external 5 Kg flywheel with $J_{ext} = 28.9[g \text{ m}^2]$

Table B.4: Current i_{sx} [A]

| | | | | | | | | |
|-------|---------------|--------|--------|--------|---------|---------|---------|---------|
| -0.01 | -20.01 | -40.02 | -60.02 | -80.01 | -100.02 | -120.02 | -140.03 | -160.02 |
| -0.01 | -20.01 | -40.02 | -60.02 | -80.01 | -100.02 | -120.02 | -140.03 | -160.02 |
| 0.00 | -20.00 | -40.02 | -60.02 | -80.02 | -100.03 | -120.04 | -140.06 | -160.07 |
| 0.01 | -19.99 | -40.03 | -60.01 | -80.03 | -100.03 | -120.05 | -140.05 | -160.08 |
| -0.03 | -19.99 | -39.99 | -60.04 | -80.03 | -100.04 | -120.13 | -140.07 | -160.10 |
| -0.01 | -20.04 | -40.03 | -60.03 | -80.08 | -100.10 | -120.12 | -140.14 | -160.19 |
| -0.04 | -20.10 | -40.05 | -60.16 | -80.10 | -100.17 | -120.25 | -140.34 | -160.32 |
| -0.18 | -20.19 | -40.14 | -60.26 | -80.40 | -100.38 | -120.45 | -140.63 | -160.60 |
| -0.36 | -20.33 | -40.37 | -60.71 | -80.66 | -100.81 | -120.89 | -140.84 | -161.12 |

Table B.5: Current i_{sy} [A]

| | | | | | | | | |
|--------|---------------|--------|--------|--------|--------|--------|--------|--------|
| 0.00 | 0.00 | 0.00 | 0.00 | 0.00 | 0.00 | 0.00 | 0.00 | 0.00 |
| 19.99 | 19.99 | 19.99 | 19.98 | 19.98 | 19.99 | 19.98 | 19.99 | 19.98 |
| 39.99 | 39.99 | 39.99 | 39.99 | 39.99 | 39.99 | 39.97 | 39.96 | 39.96 |
| 60.00 | 59.99 | 59.99 | 60.00 | 59.97 | 59.98 | 59.97 | 59.97 | 59.97 |
| 79.99 | 80.02 | 80.01 | 80.03 | 79.99 | 79.98 | 79.98 | 79.94 | 79.86 |
| 100.00 | 100.00 | 100.03 | 100.02 | 99.97 | 100.00 | 99.97 | 99.84 | 99.92 |
| 120.01 | 120.00 | 120.02 | 119.98 | 119.99 | 119.90 | 119.91 | 119.84 | 119.87 |
| 140.01 | 139.99 | 140.00 | 139.96 | 139.89 | 139.90 | 139.81 | 139.79 | 139.69 |
| 160.08 | 160.03 | 160.04 | 159.99 | 159.96 | 159.77 | 159.94 | 159.73 | 159.50 |

Table B.6: Electric acceleration df/dt [$H z/s$]

| | | | | | | | | |
|-------|--------------|--------|--------|--------|--------|--------|--------|--------|
| 0.0 | 0.0 | 0.0 | 0.0 | 0.0 | 0.0 | 0.0 | 0.0 | 0.0 |
| 98.5 | 114.1 | 130.5 | 146.6 | 161.2 | 174.5 | 186.8 | 195.5 | 204.1 |
| 204.4 | 237.6 | 271.2 | 304.4 | 336.1 | 365.1 | 393.1 | 417.7 | 438.9 |
| 311.1 | 361.8 | 411.9 | 460.9 | 508.5 | 554.0 | 596.9 | 635.4 | 670.7 |
| 419.5 | 487.4 | 552.9 | 618.3 | 681.2 | 741.4 | 797.0 | 849.2 | 894.4 |
| 529.9 | 613.8 | 694.4 | 774.1 | 851.9 | 926.2 | 992.2 | 1054.5 | 1111.5 |
| 638.8 | 738.7 | 832.9 | 926.7 | 1015.0 | 1097.8 | 1181.9 | 1243.5 | 1317.7 |
| 745.1 | 858.7 | 964.4 | 1066.5 | 1169.2 | 1261.6 | 1349.5 | 1431.3 | 1503.9 |
| 847.9 | 972.0 | 1088.3 | 1201.8 | 1311.1 | 1413.5 | 1503.1 | 1590.3 | 1672.7 |

Table B.7: Mechanic torque T [$N m$], with $J = J_{rot} + J_{5kg} = (8.8 + 28.9)$ [$g m^2$]

| | | | | | | | | |
|------|------|------|------|------|------|------|------|------|
| 0.0 | 0.0 | 0.0 | 0.0 | 0.0 | 0.0 | 0.0 | 0.0 | 0.0 |
| 5.8 | 6.8 | 7.7 | 8.7 | 9.6 | 10.3 | 11.1 | 11.6 | 12.1 |
| 12.1 | 14.1 | 16.1 | 18.0 | 19.9 | 21.6 | 23.3 | 24.7 | 26.0 |
| 18.4 | 21.4 | 24.4 | 27.3 | 30.1 | 32.8 | 35.4 | 37.6 | 39.7 |
| 24.8 | 28.9 | 32.7 | 36.6 | 40.3 | 43.9 | 47.2 | 50.3 | 53.0 |
| 31.4 | 36.4 | 41.1 | 45.9 | 50.5 | 54.9 | 58.8 | 62.5 | 65.8 |
| 37.8 | 43.8 | 49.3 | 54.9 | 60.1 | 65.0 | 70.0 | 73.7 | 78.0 |
| 44.1 | 50.9 | 57.1 | 63.2 | 69.3 | 74.7 | 79.9 | 84.8 | 89.1 |
| 50.2 | 57.6 | 64.5 | 71.2 | 77.7 | 83.7 | 89.0 | 94.2 | 99.1 |

Table B.8: x-component of the flux linkage vector ψ_{sx} [$mV \cdot s$]

| | | | | | | | | |
|------|-------------|------|------|------|------|-------|-------|-------|
| 76.8 | 60.2 | 43.5 | 26.9 | 9.9 | -6.6 | -22.3 | -37.8 | -53.4 |
| 76.8 | 60.2 | 43.5 | 26.9 | 9.9 | -6.6 | -22.3 | -37.8 | -53.4 |
| 76.5 | 59.6 | 42.9 | 26.8 | 10.3 | -6.5 | -22.1 | -37.9 | -53.2 |
| 76.1 | 59.3 | 42.7 | 26.5 | 9.6 | -6.1 | -21.9 | -37.6 | -54.2 |
| 75.8 | 59.1 | 42.8 | 26.5 | 9.6 | -6.4 | -23.2 | -37.8 | -54.3 |
| 76.1 | 59.4 | 43.1 | 26.4 | 10.0 | -6.6 | -22.3 | -36.7 | -51.2 |
| 76.8 | 59.8 | 44.1 | 27.5 | 11.6 | -4.4 | -21.0 | -35.7 | -50.9 |
| 76.2 | 59.9 | 44.5 | 28.7 | 12.3 | -4.3 | -18.9 | -35.5 | -51.1 |
| 74.9 | 60.2 | 44.6 | 29.4 | 12.8 | -1.4 | -19.6 | -32.3 | -50.7 |

Table B.9: y-component flux linkage vector ψ_{sy} [$mV \cdot s$]

| | | | | | | | | |
|-------|--------------|-------|-------|-------|-------|-------|-------|-------|
| 0.0 | 0.0 | 0.0 | 0.0 | 0.0 | 0.0 | 0.0 | 0.0 | 0.0 |
| 31.0 | 30.3 | 29.8 | 29.8 | 29.5 | 29.2 | 28.3 | 27.9 | 26.2 |
| 61.1 | 60.6 | 60.0 | 59.4 | 59.4 | 58.7 | 57.1 | 55.8 | 54.5 |
| 90.8 | 90.6 | 90.1 | 89.2 | 87.9 | 86.7 | 84.8 | 83.5 | 81.8 |
| 120.0 | 119.5 | 118.9 | 117.7 | 116.3 | 114.4 | 113.0 | 111.0 | 108.8 |
| 147.9 | 147.4 | 146.6 | 145.1 | 143.2 | 141.5 | 140.7 | 137.4 | 134.1 |
| 172.9 | 172.6 | 172.5 | 170.3 | 168.7 | 166.7 | 163.8 | 162.5 | 159.5 |
| 192.9 | 192.2 | 192.5 | 191.4 | 189.2 | 187.3 | 184.4 | 180.8 | 176.9 |
| 208.3 | 208.4 | 208.1 | 207.7 | 207.9 | 204.1 | 205.6 | 199.5 | 192.8 |

2.3 Field Weakening look-up-tables

Table B.10: Field weakening Look up table: i_{sx} [A] for $|\psi|$ [mV s] and T [Nm]

| | | | | | | | | | |
|------------------|------------|--------|--------|--------|--------|--------|--------|--------|--------|
| | $ \psi $: | 221.3 | 207.0 | 192.7 | 178.4 | 164.1 | 149.8 | 135.4 | 121.1 |
| $\downarrow T$ 0 | i_{sx} : | -0.0 | -0.0 | -0.0 | -0.0 | -0.0 | -0.0 | -0.0 | -0.0 |
| 6.5 | | -3.2 | -3.2 | -3.2 | -3.2 | -3.2 | -3.2 | -3.2 | -3.2 |
| 13.0 | | -11.2 | -11.2 | -11.2 | -11.2 | -11.2 | -11.2 | -11.2 | -11.2 |
| 19.5 | | -20.8 | -20.8 | -20.8 | -20.8 | -20.8 | -20.8 | -20.8 | -20.8 |
| 26.0 | | -28.8 | -28.8 | -28.8 | -28.8 | -28.8 | -28.8 | -28.8 | -28.8 |
| 32.5 | | -38.4 | -38.4 | -38.4 | -38.4 | -38.4 | -38.4 | -38.4 | -46.4 |
| 39.0 | | -46.4 | -46.4 | -46.4 | -46.4 | -46.4 | -46.4 | -51.2 | -68.8 |
| 45.5 | | -56.0 | -56.0 | -56.0 | -56.0 | -56.0 | -57.6 | -73.7 | -96.1 |
| 52.0 | | -62.4 | -62.4 | -62.4 | -62.4 | -62.4 | -77.8 | -99.6 | -138.4 |
| 58.5 | | -72.3 | -72.3 | -72.3 | -72.3 | -81.8 | -102.5 | -136.8 | -155.5 |
| 65.0 | | -79.8 | -79.8 | -79.8 | -83.3 | -104.5 | -134.1 | -160.2 | -155.5 |
| 71.5 | | -88.1 | -88.1 | -88.1 | -103.9 | -133.6 | -160.2 | -160.2 | -155.5 |
| 78.0 | | -96.7 | -96.7 | -102.2 | -127.3 | -160.3 | -160.2 | -160.2 | -155.5 |
| 84.5 | | -103.7 | -103.7 | -125.2 | -155.9 | -160.3 | -160.2 | -160.2 | -155.5 |
| 91.0 | | -128.5 | -128.5 | -146.9 | -160.5 | -160.3 | -160.2 | -160.2 | -155.5 |
| 97.5 | | -154.6 | -154.6 | -160.9 | -160.5 | -160.3 | -160.2 | -160.2 | -155.5 |
| | $ \psi $: | 106.8 | 92.5 | 78.2 | 63.8 | 49.5 | 35.2 | 20.9 | 6.6 |
| $\downarrow T$ 0 | i_{sx} : | -0.0 | -0.0 | -0.0 | -16.0 | -33.6 | -51.2 | -67.2 | -84.8 |
| 6.5 | | -3.2 | -3.2 | -8.0 | -24.0 | -41.6 | -60.8 | -84.8 | -91.4 |
| 13.0 | | -11.2 | -11.2 | -25.6 | -43.2 | -64.0 | -100.6 | -93.7 | -91.4 |
| 19.5 | | -20.8 | -30.4 | -48.0 | -70.4 | -109.7 | -100.6 | -93.7 | -91.4 |
| 26.0 | | -38.4 | -56.0 | -78.4 | -118.9 | -109.7 | -100.6 | -93.7 | -91.4 |
| 32.5 | | -62.4 | -84.8 | -125.8 | -118.9 | -109.7 | -100.6 | -93.7 | -91.4 |
| 39.0 | | -91.2 | -137.2 | -125.8 | -118.9 | -109.7 | -100.6 | -93.7 | -91.4 |
| 45.5 | | -146.4 | -137.2 | -125.8 | -118.9 | -109.7 | -100.6 | -93.7 | -91.4 |
| 52.0 | | -146.4 | -137.2 | -125.8 | -118.9 | -109.7 | -100.6 | -93.7 | -91.4 |
| 58.5 | | -146.4 | -137.2 | -125.8 | -118.9 | -109.7 | -100.6 | -93.7 | -91.4 |
| 65.0 | | -146.4 | -137.2 | -125.8 | -118.9 | -109.7 | -100.6 | -93.7 | -91.4 |
| 71.5 | | -146.4 | -137.2 | -125.8 | -118.9 | -109.7 | -100.6 | -93.7 | -91.4 |
| 78.0 | | -146.4 | -137.2 | -125.8 | -118.9 | -109.7 | -100.6 | -93.7 | -91.4 |
| 84.5 | | -146.4 | -137.2 | -125.8 | -118.9 | -109.7 | -100.6 | -93.7 | -91.4 |
| 91.0 | | -146.4 | -137.2 | -125.8 | -118.9 | -109.7 | -100.6 | -93.7 | -91.4 |
| 97.5 | | -146.4 | -137.2 | -125.8 | -118.9 | -109.7 | -100.6 | -93.7 | -91.4 |

Table B.11: Field weakening Look up table: $i_{sy} [A]$ for $|\psi| [mV s]$ and $T [Nm]$

| | $ \psi :$ | 221.3 | 207.0 | 192.7 | 178.4 | 164.1 | 149.8 | 135.4 | 121.1 |
|------------------|------------|-------|-------|-------|-------|-------|-------|-------|-------|
| $\downarrow T$ 0 | $i_{sy} :$ | 0.0 | 0.0 | 0.0 | 0.0 | 0.0 | 0.0 | 0.0 | 0.0 |
| 6.5 | | 21.6 | 21.6 | 21.6 | 21.6 | 21.6 | 21.6 | 21.6 | 21.6 |
| 13.0 | | 39.4 | 39.4 | 39.4 | 39.4 | 39.4 | 39.4 | 39.4 | 39.4 |
| 19.5 | | 54.5 | 54.5 | 54.5 | 54.5 | 54.5 | 54.5 | 54.5 | 54.5 |
| 26.0 | | 68.3 | 68.3 | 68.3 | 68.3 | 68.3 | 68.3 | 68.3 | 68.3 |
| 32.5 | | 80.2 | 80.2 | 80.2 | 80.2 | 80.2 | 80.2 | 80.2 | 76.6 |
| 39.0 | | 91.6 | 91.6 | 91.6 | 91.6 | 91.6 | 91.6 | 89.2 | 81.5 |
| 45.5 | | 101.4 | 101.4 | 101.4 | 101.4 | 101.4 | 100.5 | 92.9 | 84.2 |
| 52.0 | | 112.3 | 112.3 | 112.3 | 112.3 | 112.3 | 104.3 | 95.0 | 83.1 |
| 58.5 | | 121.0 | 121.0 | 121.0 | 121.0 | 115.7 | 106.2 | 94.3 | 80.5 |
| 65.0 | | 130.9 | 130.9 | 130.9 | 128.8 | 117.8 | 106.3 | 92.6 | 80.5 |
| 71.5 | | 140.2 | 140.2 | 140.2 | 131.3 | 118.2 | 105.1 | 92.6 | 80.5 |
| 78.0 | | 149.6 | 149.6 | 146.1 | 132.9 | 117.1 | 105.1 | 92.6 | 80.5 |
| 84.5 | | 159.8 | 159.8 | 147.3 | 133.1 | 117.1 | 105.1 | 92.6 | 80.5 |
| 91.0 | | 159.9 | 159.9 | 149.9 | 132.9 | 117.1 | 105.1 | 92.6 | 80.5 |
| 97.5 | | 159.6 | 159.6 | 150.9 | 132.9 | 117.1 | 105.1 | 92.6 | 80.5 |

| | $ \psi :$ | 106.8 | 92.5 | 78.2 | 63.8 | 49.5 | 35.2 | 20.9 | 6.6 |
|------------------|------------|-------|------|------|------|------|------|------|-----|
| $\downarrow T$ 0 | $i_{sy} :$ | 0.0 | 0.0 | 0.0 | 0.0 | 0.0 | 0.0 | 0.0 | 0.0 |
| 6.5 | | 21.6 | 21.6 | 20.9 | 18.7 | 16.6 | 14.9 | 13.3 | 4.5 |
| 13.0 | | 39.4 | 39.4 | 35.7 | 32.0 | 28.7 | 23.6 | 14.2 | 4.5 |
| 19.5 | | 54.5 | 51.2 | 46.1 | 41.0 | 32.8 | 23.6 | 14.2 | 4.5 |
| 26.0 | | 64.4 | 58.4 | 52.3 | 42.1 | 32.8 | 23.6 | 14.2 | 4.5 |
| 32.5 | | 70.3 | 63.3 | 52.1 | 42.1 | 32.8 | 23.6 | 14.2 | 4.5 |
| 39.0 | | 73.7 | 61.2 | 52.1 | 42.1 | 32.8 | 23.6 | 14.2 | 4.5 |
| 45.5 | | 70.8 | 61.2 | 52.1 | 42.1 | 32.8 | 23.6 | 14.2 | 4.5 |
| 52.0 | | 70.8 | 61.2 | 52.1 | 42.1 | 32.8 | 23.6 | 14.2 | 4.5 |
| 58.5 | | 70.8 | 61.2 | 52.1 | 42.1 | 32.8 | 23.6 | 14.2 | 4.5 |
| 65.0 | | 70.8 | 61.2 | 52.1 | 42.1 | 32.8 | 23.6 | 14.2 | 4.5 |
| 71.5 | | 70.8 | 61.2 | 52.1 | 42.1 | 32.8 | 23.6 | 14.2 | 4.5 |
| 78.0 | | 70.8 | 61.2 | 52.1 | 42.1 | 32.8 | 23.6 | 14.2 | 4.5 |
| 84.5 | | 70.8 | 61.2 | 52.1 | 42.1 | 32.8 | 23.6 | 14.2 | 4.5 |
| 91.0 | | 70.8 | 61.2 | 52.1 | 42.1 | 32.8 | 23.6 | 14.2 | 4.5 |
| 97.5 | | 70.8 | 61.2 | 52.1 | 42.1 | 32.8 | 23.6 | 14.2 | 4.5 |

2.4 Curve fitting of the oscillations to determine the cogging torque

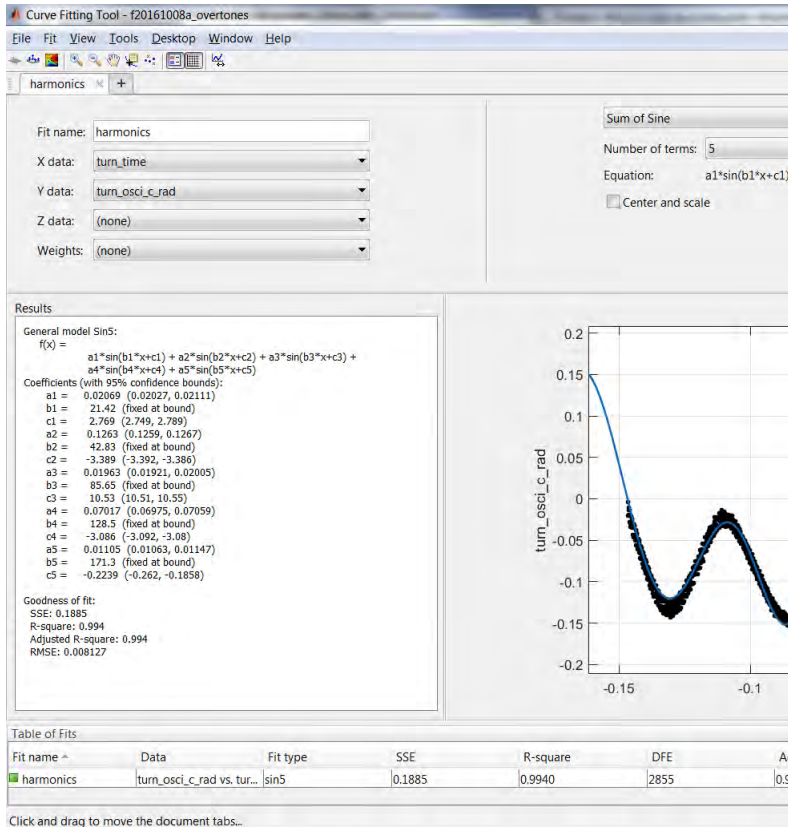


Figure B.1: harmonics fitting (left)

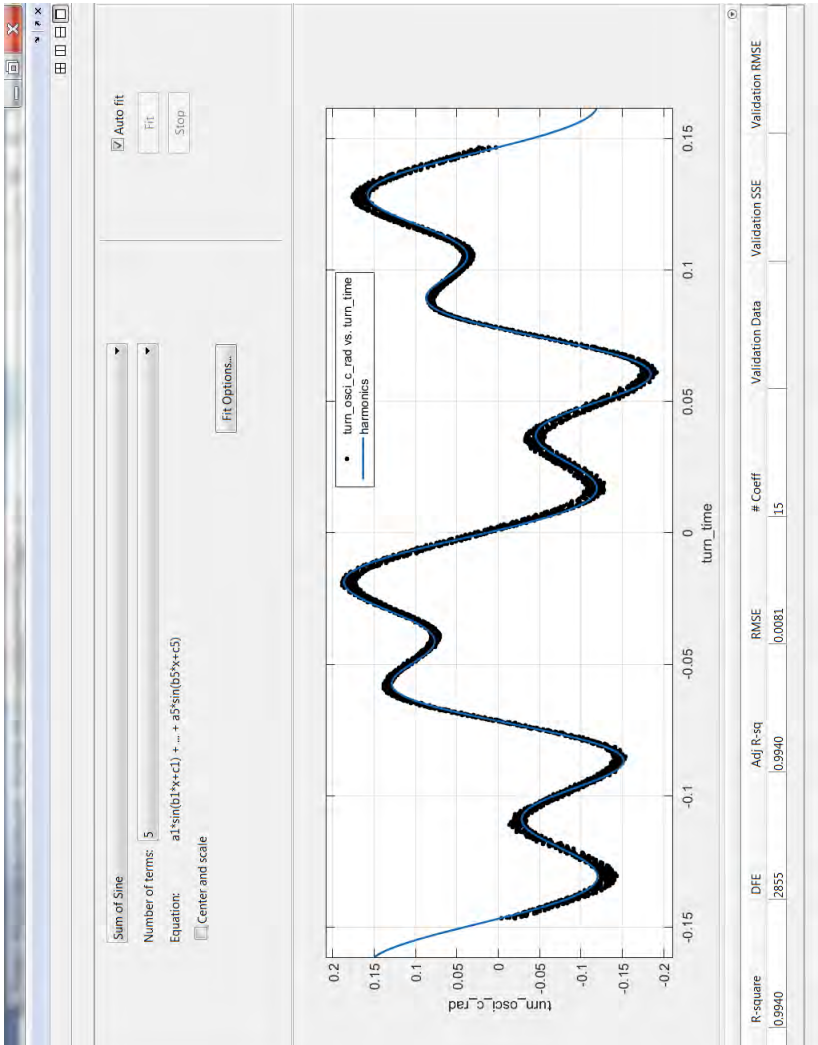


Figure B.2: harmonics fitting (right)

Appendix C

Drawings of the electric machine

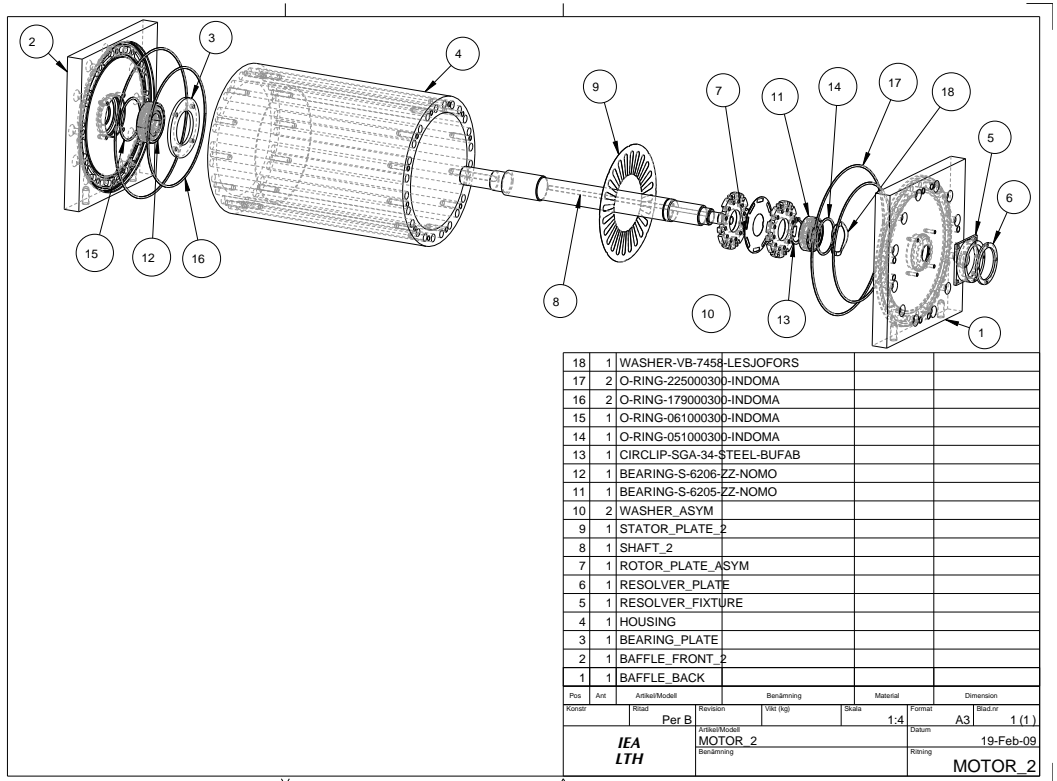


Figure C.1: Components of the *iPMSM*

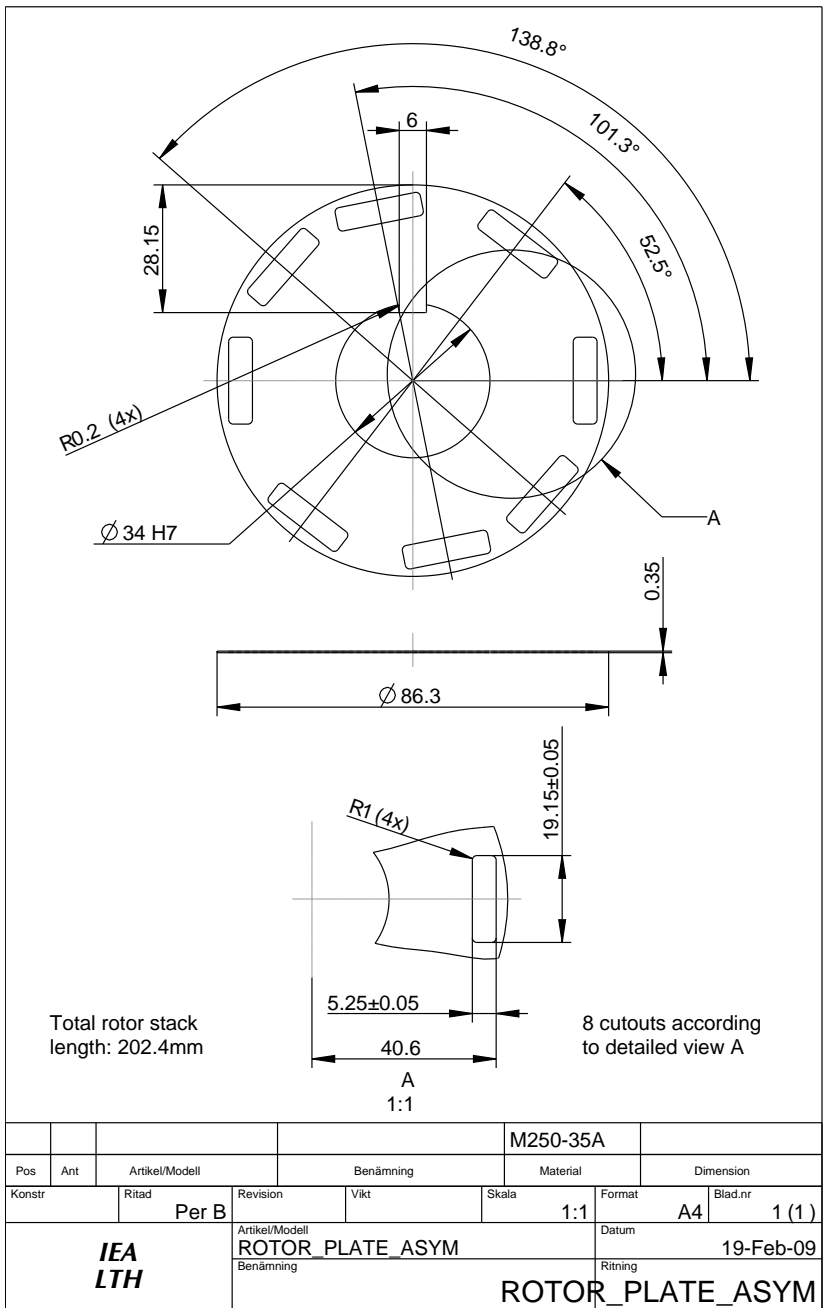
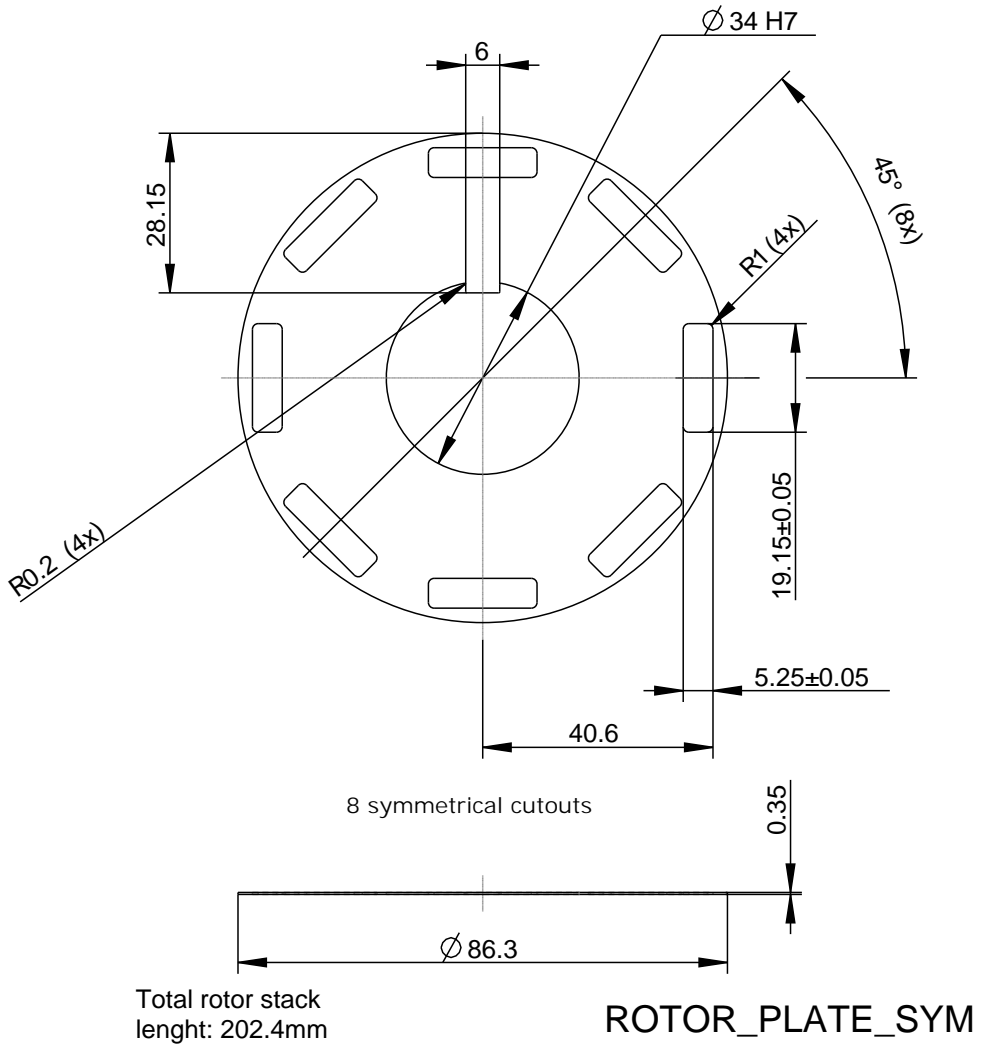


Figure C.3: The asymmetric rotor



| | | | | | | M250-35A | | |
|--------|-----|-----------------|-----------|------|----------|-----------|---------|--|
| Pos | Ant | Artikel/Modell | Benämning | | Material | Dimension | | |
| Konstr | | Ritad | Revision | Vikt | Skala | Format | Blad.nr | |
| | | Per B | | | 1:1 | A4 | 1 (1) | |
| IEA | | Artikel/Modell | | | | Datum | | |
| LTH | | ROTOR_PLATE_SYM | | | | 19-Feb-09 | | |
| | | Benämning | | | | Ritning | | |

Figure C.4: The symmetric rotor

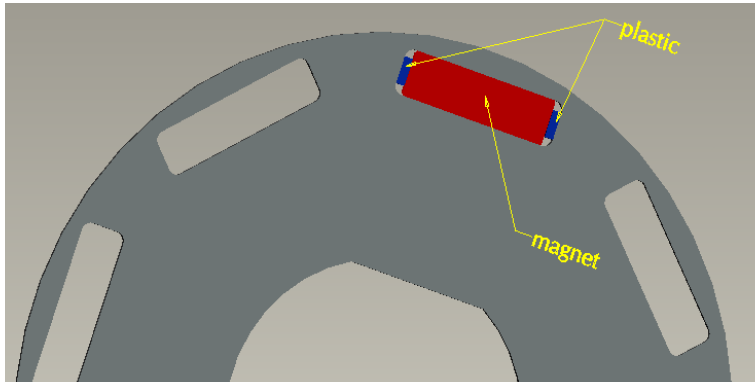


Figure C.5: Plastic pieces on the side of the magnets to fix them in place. The extra space on the side of the magnets is to avoid magnetic short cut between the *nord* and *south* side of the magnet

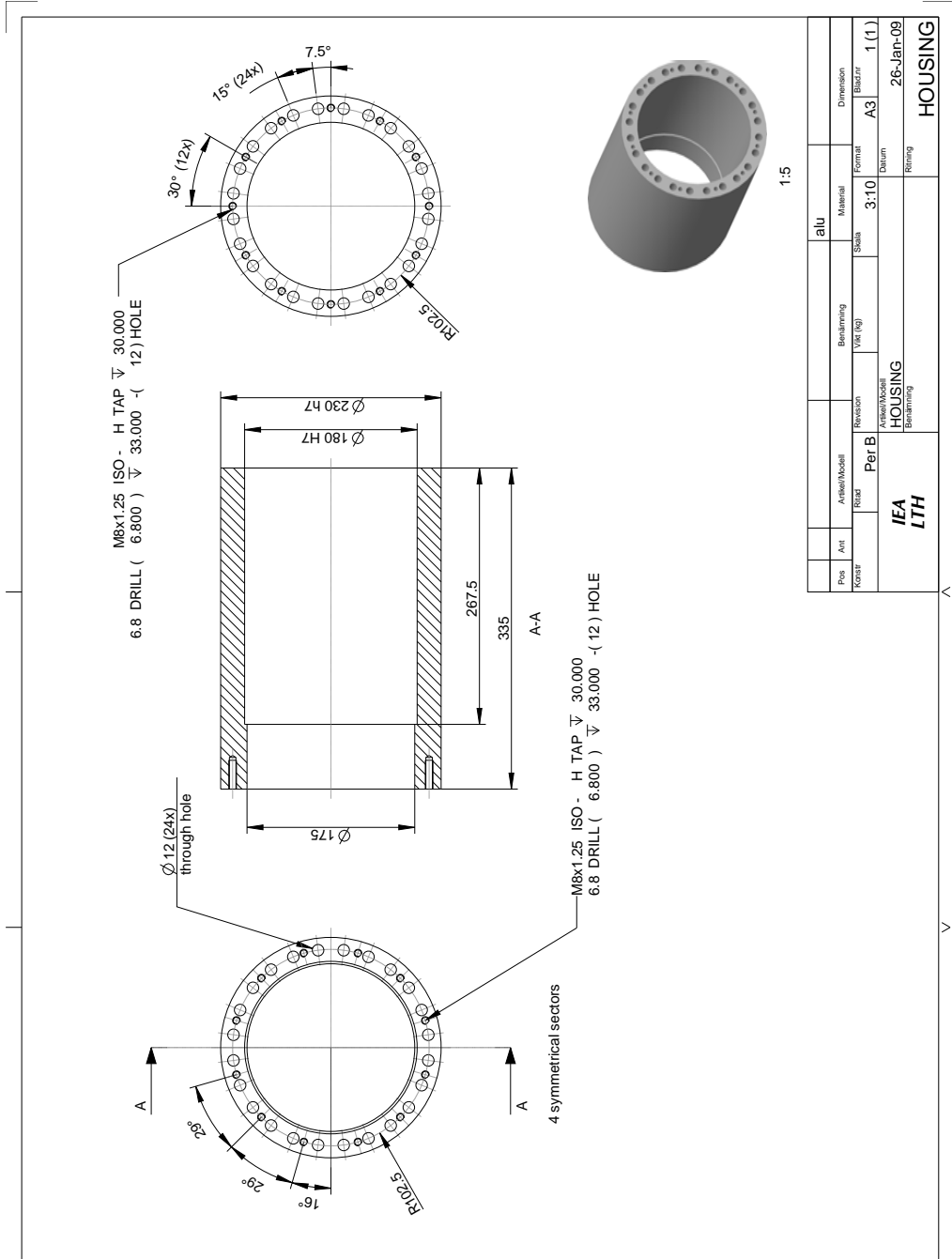


Figure C.6: Mantle of the housing, with cooling channels

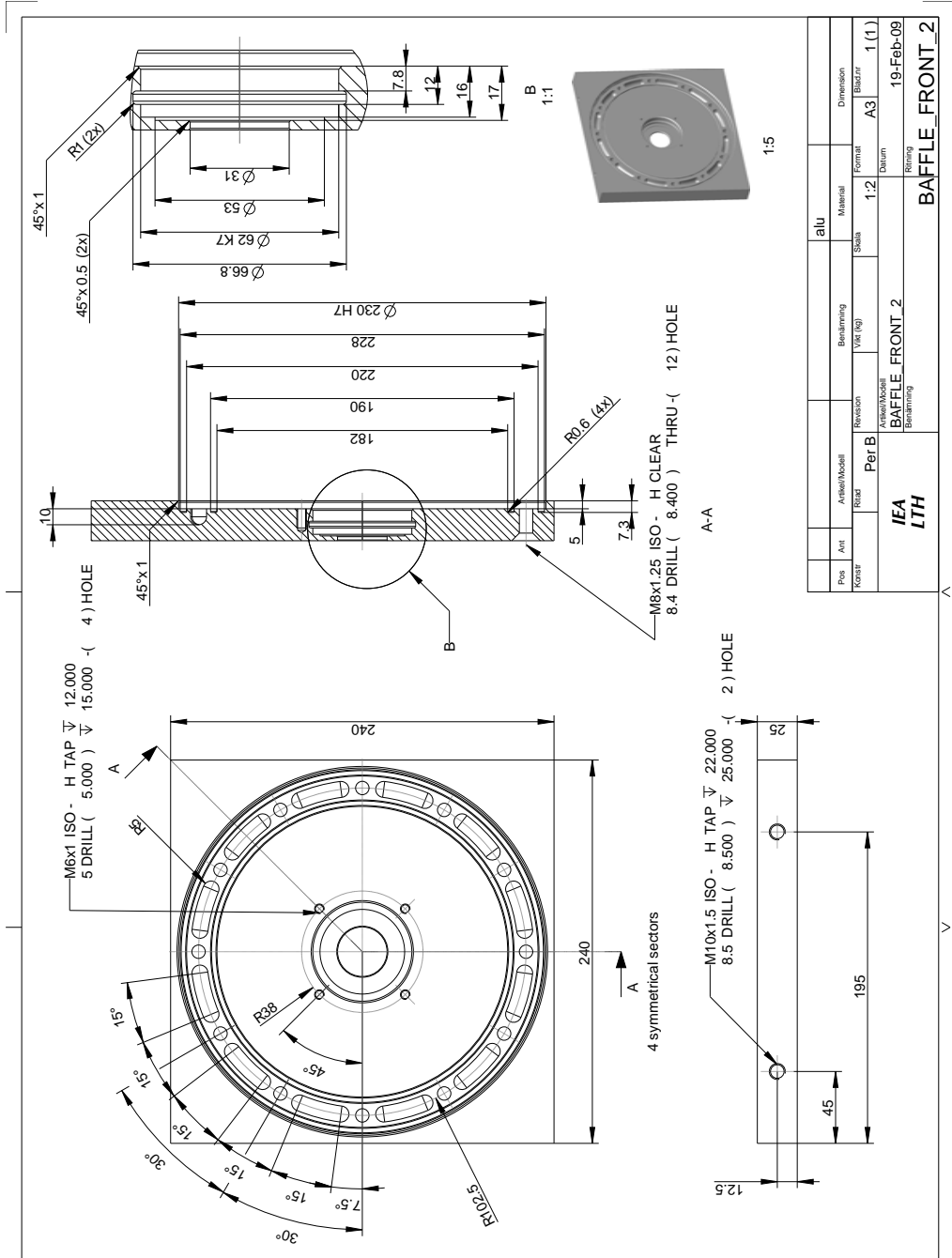


Figure C.7: The front baffle

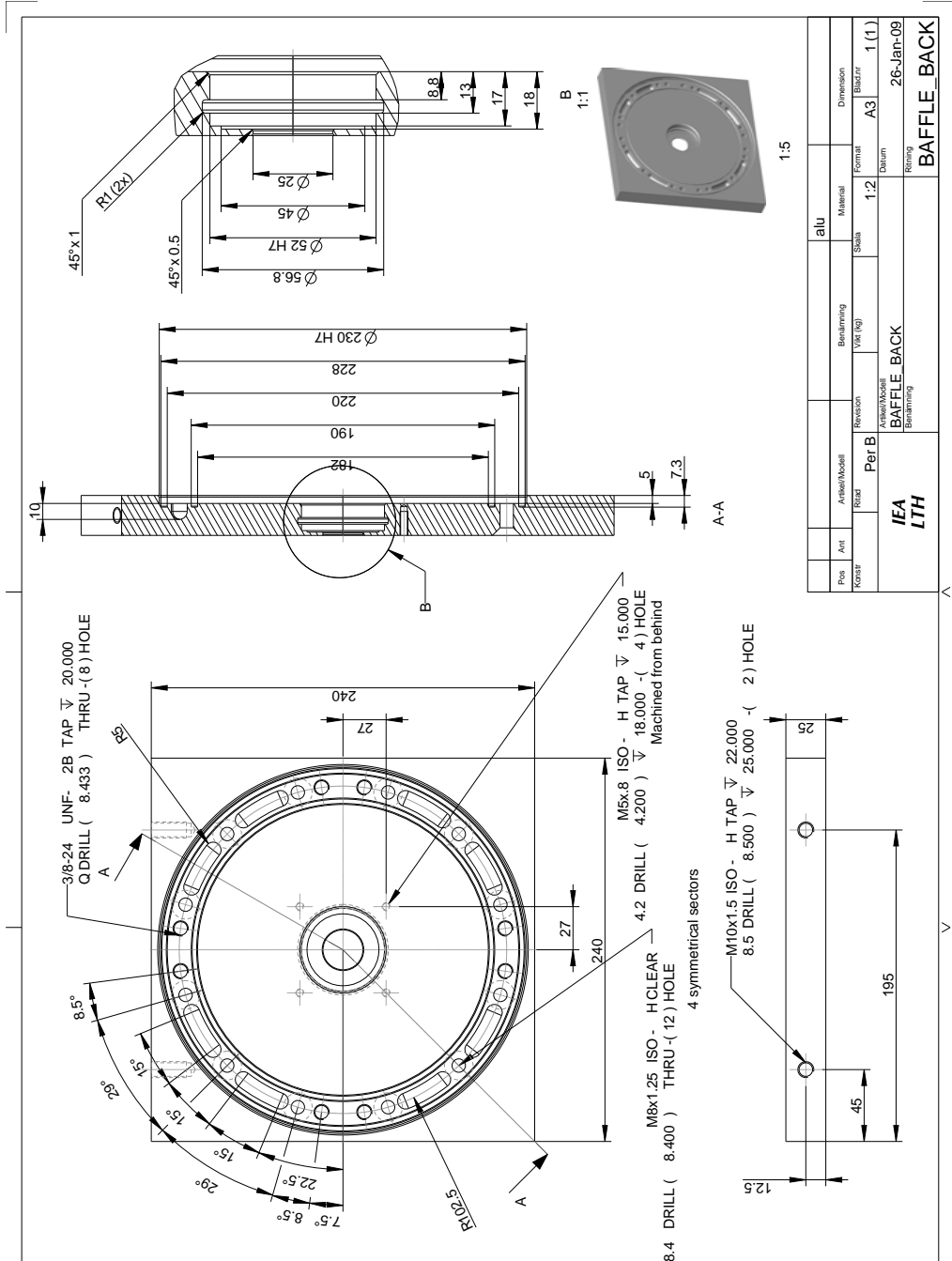


Figure C.8: The rear baffle

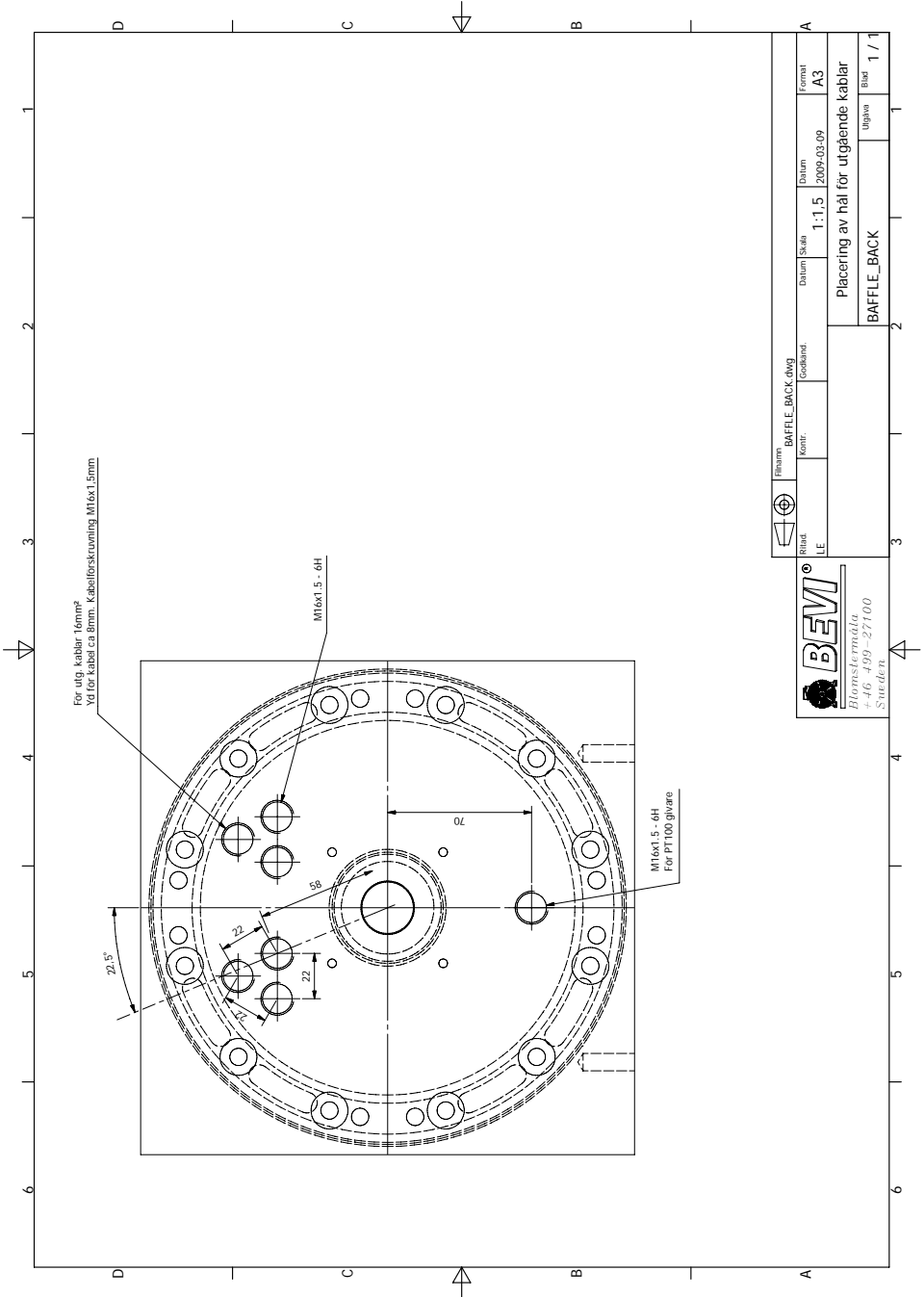


Figure C.9: The rear baffle, with holes for power and sensor cables

Appendix D

Data sheets



Figure D.1: Data sheet for the laminated steel plates used in the iron core, source 'Surahammar'

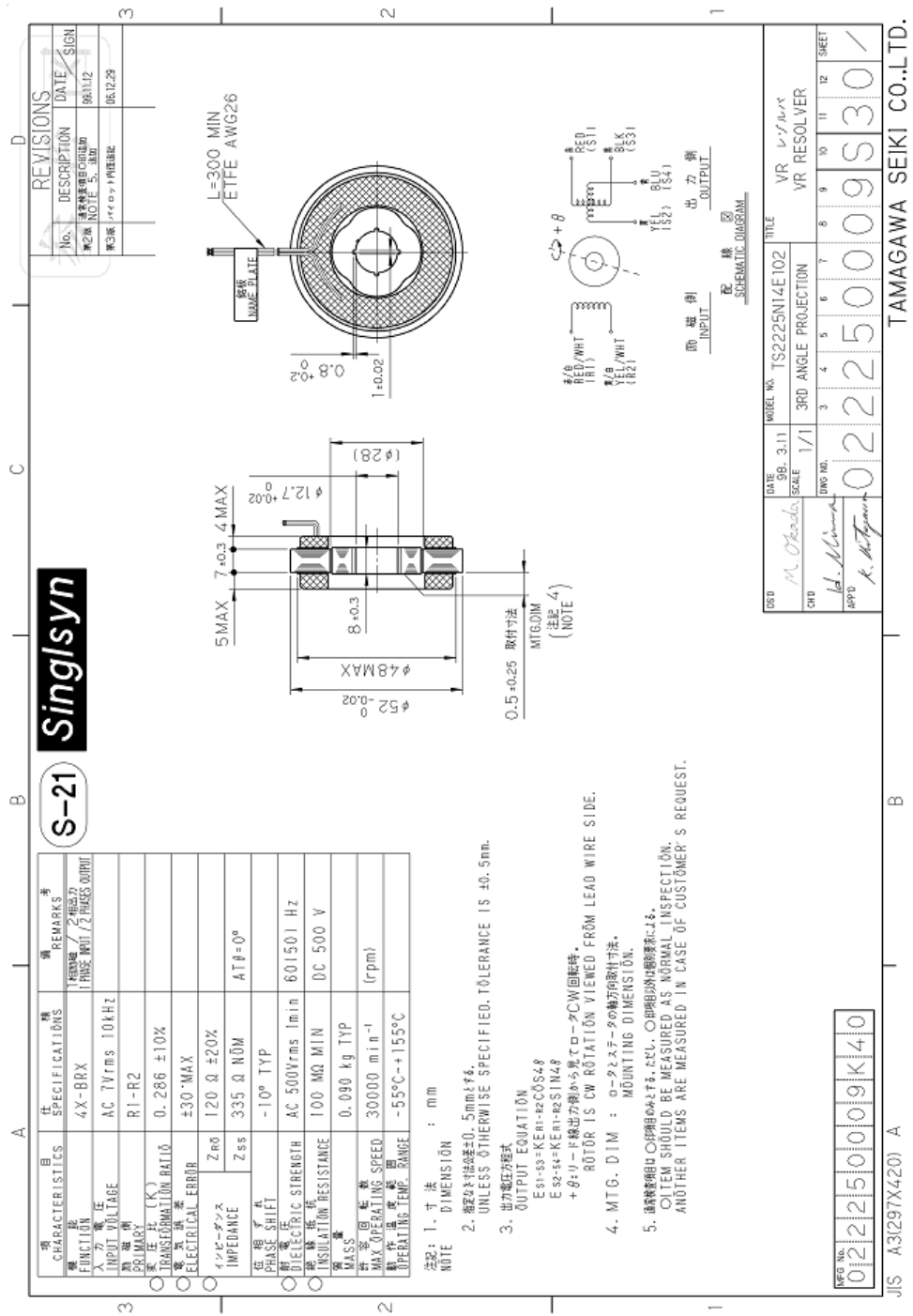


Figure D.2: Specifications of the resolver

List of Figures

| | | |
|-----|---|-------|
| 1 | Topology of the hybrid drive train | xviii |
| 2 | Numerical simulation for the electric motor design | xviii |
| 3 | Manufacturing of the electric motor | xix |
| 4 | A state of the art control and measurement system is developed for this dynamic electric motor | xix |
| 5 | The Dynamic Test Method reduces the need of expensive equipment and make the measurement more precise | xx |
| 6 | The required information from the electric motor is obtained. For example, the torque map is displayed as a function of the direction and intensity of the magnetic fields created inside the motor . . . | xx |
| 7 | Other example of required data is the torque ripple, which is calculated by decomposing the oscillations during rotation. . . . | xxi |
| 8 | The efficiency map of the motor, standard information required in the industry for optimal use and integration of the motor, is also calculated from the measurements | xxi |
| 2.1 | Topology of the hybrid drive train | 8 |
| 2.2 | The speed of the <i>output shaft</i> remains unchanged under gearshift. The <i>input shaft</i> needs to adapt to the speed corresponding to the new gear ratio. | 10 |
| 2.3 | Speed of the input shaft for different gears, and speed of the output shaft, vs. the vehicle speed | 11 |
| 2.4 | The <i>Parallel Drive Bench</i> with the new customized <i>EM</i> | 13 |
| 2.5 | Transmission between the <i>EM</i> and the <i>ICE</i> and the gearbox via a belt drive | 14 |
| 3.1 | The belt speed ratio. The required torque decreases with k_{belt} but the maximal allowed speed limits k_{belt} to 2 | 19 |
| 3.2 | Power, torque and speed specifications for the electric machine . | 20 |
| 3.3 | Flowchart of the optimization process | 22 |
| 3.4 | Model of the <i>EM</i> in <i>FEMM</i> | 23 |
| 3.5 | Temperature distribution over the <i>EM</i> [°C] | 24 |

| | | |
|------|--|----|
| 3.6 | Mesh of current points in the rotor coordinate system | 25 |
| 3.7 | Phase currents, corresponding to one current point, during rotation | 25 |
| 3.8 | Electromagnetic Finite Element Analysis to determine the Torque T and the flux-linkage $\vec{\psi}$ | 26 |
| 3.9 | FEMM output: phase current $[i_a, i_b, i_c]$, torque T and phase flux-linkage $[\psi_a, \psi_b, \psi_c]$ for one of the current vectors (blue ring) | 26 |
| 3.10 | The flux linkage as vector $[\psi_{sx}, \psi_{sy}]$ is calculated for the 4 selected current vectors. Note that ψ_{sx} depends mainly on i_{sx} and ψ_{sy} on i_{sy} | 27 |
| 3.11 | Linear interpolation of the flux linkage $[\psi_{sx}, \psi_{sy}]$ for the interior points | 28 |
| 3.12 | The Torque $T = n_{pp} \cdot \vec{\psi} \times \vec{i}$ calculated for the interior points. The nominal torque T_{nom} is found along the circle with radius I_0 | 28 |
| 3.13 | The flux linkage $\vec{\psi}_0$ for the nominal current \vec{i}_0 | 30 |
| 3.14 | The peak current I_{peak} is found by tracing the currents along the constant torque line $T = T_{peak}$ and finding the one that lies closest to the origin | 31 |
| 3.15 | Electric representation of the $iPMSM$ | 32 |
| 3.16 | The demagnetization point \vec{i}_{demag} where $ \vec{\psi}_{demag} = \mathbf{0}$. The current is moved towards this point to be able to run the EM above nominal speed | 36 |
| 3.17 | Final geometry of the EM | 40 |
| 3.18 | Electromagnetic FEA of the final geometry | 41 |
| 3.19 | The current vectors at which the flux will be calculated are transformed to phase current values for the FEA in total $30\theta \times 4i_{isx} \times 6i_{isy} = 720$ simulations | 41 |
| 3.20 | Computation of the flux $\vec{\psi}$ at $30\theta \times 4i_{isx} \times 6i_{isy} = 720$ simulations, ca. 12 hours, for one rotor | 42 |
| 3.21 | Mesh with the flux vector $[\psi_{sx}, \psi_{sy}]$ at $4i_{isx}$, $6i_{isy}$ and 30θ | 43 |
| 3.22 | Mesh with the flux vector $[\psi_{sx}, \psi_{sy}]$ at $4i_{isx}$, $6i_{isy}$ and average over θ | 43 |
| 3.23 | Torque and speed contour lines in the $[i_{isx}i_{isy}]$ -plane. The maximal reachable speeds under 4 different conditions. | 45 |
| 3.24 | Maximal possible speed as a function of torque under 4 different conditions | 46 |
| 3.25 | Maximal power as a function of speed under the 4 different conditions | 46 |
| 3.26 | Optimal current for Torque beyond T_{peak} | 48 |
| 3.27 | Flux linkage for high current values | 48 |
| 3.28 | Torque for high current values | 48 |

| | | |
|------|--|----|
| 3.29 | Rotational symmetric and asymmetric placement of the magnets. The second one produces a smoother rotation by preventing that the magnets come close to the iron teeth at the same time | 50 |
| 3.30 | In the asymmetric rotor the magnets are displaced 0,2,3 and 1 time the angle between 2 iron tooth divided by 4, i.e, $15^{\circ}_{mech}/4$ | 50 |
| 3.31 | Sketch of the hot-cold-side property of the magnets | 51 |
| 3.32 | comparison between the four rotors at the nominal torque $T_{nom} = 45Nm$. Different amounts of current are required to produce T_{nom} . The figure also shows the variation of the torque depending on the rotor angular position i.e. <i>cogging</i> | 52 |
| 3.33 | Comparison between the four rotors at the peak torque $T_{peak} = 90Nm$ showing the needed amount of current and the torque ripple. | 52 |
| 3.34 | Location of the current vectors for nominal Torque, peak Torque and demagnetization on the i_{sx}, i_{sy} plane for the four rotor types | 53 |
| 3.35 | Temperature distribution along a radial line. load: T_{nom}, ω_0 . . . | 54 |
| 3.36 | Flux density B on the EM, when I_0 is applied | 57 |
| 3.37 | Flux density along red line in (figure 3.36) (pos0 : point down right) | 57 |
| 3.38 | The housing, seen from behind | 61 |
| 3.39 | The EM from the shaft side. On the sides of the mantle we can see the cables for temperature measurement. | 61 |
| 3.40 | The EM with the power cables and water cooling connection. The resolver had not yet been mounted when the picture was taken. . | 62 |
| 3.41 | The stator inside the housing | 62 |
| 3.42 | The Stator with the winding inside the housing. | 63 |
| 3.43 | The rotor being mounted. | 63 |
| 3.44 | One rotor with its shaft and one stator plate compated to the size of a pen. | 63 |
| 3.45 | The resolver on the back side of the <i>EM</i> | 64 |
| 3.46 | The 4 pole pair resolver. | 64 |
| 4.1 | Sketch of the <i>Brake Bench</i> | 67 |
| 4.2 | Picture of a <i>Brake Bench</i> with the brake motor (grey). Here neither the tested motor nor the torque sensor are shown. Courtesy of <i>RISE</i> , previously <i>SP</i> | 68 |
| 4.3 | Set up of the Dynamic Measurement. | 69 |
| 5.1 | Sketch of the experimental setup | 76 |
| 5.2 | Constant acceleration when a constant current is applied | 76 |

| | | |
|------|---|----|
| 5.3 | Mesh of the torque T as a function of applied current vectors $[i_{sx}, i_{sy}]$ | 78 |
| 5.4 | Voltage under acceleration | 79 |
| 5.5 | Electric representation of the $iPMSM$ | 79 |
| 5.6 | ψ_{sx} , the x-component of the Flux linkage, as a function of applied current $[i_{sx}, i_{sy}]$. ψ_{sx} is mainly dependent of i_{sx} and is zero at the demagnetization point $[i_{sx,demag}, 0]$ | 81 |
| 5.7 | ψ_{sy} , the y-component of the Flux linkage, as a function of applied current $[i_{sx}, i_{sy}]$. ψ_{sy} is mainly dependent of i_{sy} | 82 |
| 5.8 | Voltage at 0 Hz , to calculate the resistance | 83 |
| 5.9 | Voltage u_{sy} , at 0 Hz vs. current i_{sy} for $i_{sx} = 0$ | 83 |
| 5.10 | Voltage u_{sx} at 0 Hz vs. current i_{sx} for $i_{sy} = 20[A]$ | 83 |
| 5.11 | Sketch of the EM without and with different external flywheels to determine the inertia of the rotor | 84 |
| 5.12 | photo of 3 different external flywheels | 84 |
| 5.13 | The $iPMSM$ with the largest external flywheel ($m = 10kg$). The smallest flywheel, ($m = 2.5kg$), is also shown in the picture . . . | 85 |
| 5.14 | Acceleration as function of applied current for different values of added external inertia | 85 |
| 5.15 | Acceleration as function of added external inertia for the current point $\vec{i}_s = [0\ 80][A]$ | 86 |
| 5.16 | Calculation of the inertia of the rotor J_{rotor} using the linear relation that exists between the inertia and the inverse of the acceleration at a constant torque T^* . Here $T^* = T([0\ 80][A])$ | 87 |
| 5.17 | Torque as function of applied current for different values of inertia | 88 |
| 5.18 | Effect of the friction observed in a deceleration-acceleration sequence. | 89 |
| 5.19 | Acceleration (df/dt) at different speeds. No clear correlation is observed between the friction and the speed within braking or acceleration period. | 91 |
| 5.20 | Extrapolation of the torque vs. current toward zero to calculate the friction | 91 |
| 5.21 | Pulse Width Modulation. The 3 phase pulsed voltages v_{pa} , v_{pb} , v_{pc} , (50x attenuation) | 93 |
| 5.22 | Measurement point of the instantaneous pulsed voltages | 93 |
| 5.23 | DC-link voltage u_{dc} and phase potential v_a during the sequence | 94 |
| 5.24 | Close up showing the 3 phase voltages | 94 |
| 5.25 | Voltage vector \vec{u}_s in the rotor coordinate system xy during the brake-acceleration sequence | 95 |
| 5.26 | Oscillations of the current during brake-acceleration sequence with PI-current control | 96 |

| | | |
|------|--|-----|
| 5.27 | Oscillations of the current, close up | 97 |
| 5.28 | The current vs the electric rotor position θ | 97 |
| 5.29 | The voltage vs the electric rotor position θ | 98 |
| 5.30 | Constant voltage is applied. The oscillations in the current are reduced by keeping the speed low. | 98 |
| 5.31 | Electric angular position θ at low speed. The speed in average is constant. The oscillations only in the lower part. | 99 |
| 5.32 | Spectrum of the oscillations of θ | 99 |
| 5.33 | The oscillations of θ approximated as a sum of harmonics | 100 |
| 5.34 | The harmonics of the oscillations of the electric angular position θ_{osc} and the corresponding time derivatives: speed and acceleration | 101 |
| 5.35 | The reconstructed oscillations as a sum of its harmonics and the corresponding speed and acceleration | 101 |
| 5.36 | The cogging torque and the contribution of the strongest harmonic. | 102 |
| 5.37 | Current necessary to overcome the cogging torque | 103 |
| 5.38 | Necessary torque to start | 103 |
| 5.39 | Comparison between the start torque and the cogging torque . . | 104 |
| 5.40 | Mechanic and Electromagnetic torque. | 105 |
| 5.41 | Electric, electromagnetic and mechanical power | 106 |
| 5.42 | close up of the Electric, Electromagnetic and Mechanical power . | 107 |
| 5.43 | x-component of the flux linkage, ψ_{sx} | 108 |
| 5.44 | y-component of the flux linkage, ψ_{sy} | 109 |
| 5.45 | Torque T | 109 |
| 5.46 | Difference between the measured and simulated torque $T_{sim} - T_{meas}$ | 110 |
| 5.47 | Comparison of the <i>Torque</i> measured with the dynamic and the static methods (ExSam machine) | 111 |
| 5.48 | Difference of the <i>Torque</i> measured with the dynamic and the static methods (ExSam machine) | 111 |
| 6.1 | Torque lines [Nm], optimal points and the nominal current point \vec{i}_0 Selecting torque level is similar to applying different pressure on the gas pedal on a conventional car; as well as the brake and reverse. | 114 |
| 6.2 | Flux $ \psi $ ellipses [mVs]. Max torque at the dots. Selecting them is similar to using the gearbox on a conventional car. Smallest ellipse allows higher speeds but at lower torque. | 115 |
| 6.3 | Selection of optimal current points at for ex. the 4:th torque line | 117 |
| 6.4 | Complete Look up table | 119 |
| 6.5 | Highest possible torque for different flux ψ values. Example speeds according to (table 6.3) $f_{el,0}=212[Hz];3183[rpm]$ $T_{nom}=45[Nm]$. | 119 |

| | | |
|------|---|-----|
| 6.6 | Optimal current for all combinations of torque and flux | 120 |
| 6.7 | Acceleration using the Look Up tables | 121 |
| 6.8 | Automatically selected current points during acceleration using Look Up tables (<i>LUTs</i>) | 122 |
| 6.9 | voltage under acceleration | 122 |
| 6.10 | Mecanical Power produced by the <i>EM</i> | 123 |
| 6.11 | Friction and resistive losses | 124 |
| 6.12 | Efficiency η | 125 |
| 6.13 | vehicle linear speed vs. the angular speed of the <i>EM</i> for different gears | 127 |
| 6.14 | linear force on the wheels delivered by the EM at different ang. speeds for different gears | 127 |
| 6.15 | force on the wheels delivered by the EM vs the vehicle linear speed | 127 |
| 6.16 | Synchronization time vs. f_{el} at 1 st gear 1 st gear \leftrightarrow 2 nd gear $f_{el,1} \leftrightarrow 0.6835 f_{el,1}$ | 131 |
| 6.17 | Synchronization time vs f_{el} at the lower gear of each pair. $P =$ P_{peak} | 131 |
| 6.18 | Allowed speed range for gear shifting | 132 |
| 6.19 | Synchronization time vs vehicle speed. P_{peak} | 133 |
| | | |
| A.1 | the laboratory | 137 |
| A.2 | Top view of the <i>parallel drive bench</i> with the <i>iPMSM</i> and other components | 138 |
| A.3 | The <i>parallel drive bench</i> with the <i>iPMSM</i> | 139 |
| A.4 | Electric machine on the bench | 139 |
| A.5 | The control unit | 140 |
| A.6 | The Power Electronics Converter | 141 |
| A.7 | Portable control unit, with the <i>Interface cards</i> and the <i>CompactRIO</i> | 141 |
| A.8 | Portable control unit, with the <i>PEC</i> shown in the lower part . . | 142 |
| A.9 | The PC interface of the Labview program | 142 |
| A.10 | The front panel of the post processing file in Labview | 143 |
| | | |
| B.1 | harmonics fitting (left) | 150 |
| B.2 | harmonics fitting (right) | 151 |
| | | |
| C.1 | Components of the <i>iPMSM</i> | 153 |
| C.2 | The stator | 154 |
| C.3 | The asymmetric rotor | 155 |
| C.4 | The symmetric rotor | 156 |

| | | |
|-----|---|-----|
| C.5 | Plastic pieces on the side of the magnets to fix them in place. The extra space on the side of the magnets is to avoid magnetic short cut between the <i>nord</i> and <i>south</i> side of the magnet | 157 |
| C.6 | Mantle of the housing, with cooling channels | 158 |
| C.7 | The front baffle | 159 |
| C.8 | The rear baffle | 160 |
| C.9 | The rear baffle, with holes for power and sensor cables | 161 |
| D.1 | Data sheet for the laminated steal plates used in the iron core, source 'Surahammar' | 163 |
| D.2 | Specifications of the resolver | 164 |

List of Tables

| | | |
|------|--|----|
| 3.1 | Speed and torque specifications of the EM | 20 |
| 3.2 | Electric frequency for different number of pole pairs, at 15000 [rpm] | 21 |
| 3.3 | Selected number of pole pairs | 21 |
| 3.4 | Nominal current vector | 29 |
| 3.5 | Nominal flux vector | 29 |
| 3.6 | The nominal induced voltage per turn | 34 |
| 3.7 | Number of winding turns | 35 |
| 3.8 | Geometric data for the slots | 55 |
| 3.9 | Resistivity | 55 |
| 3.10 | Resistance values, excluding end turns and connection cables | 55 |
| 3.11 | Values for the applied current | 56 |
| 3.12 | Resistive heat generation | 56 |
| 3.13 | Values used for the calculation of the heat generation on the iron core of the stator. (material: Sura M250-35A) | 58 |
| 3.14 | Geometric data | 58 |
| 3.15 | Mass and inertia data | 59 |
| 3.16 | Mechanic data | 59 |
| 3.17 | Top measured mechanic values | 59 |
| 3.18 | Electric data, performance and requirements | 60 |
| 3.19 | Electric data, passive properties | 60 |
| 3.20 | Thermal requirements | 60 |
| 3.21 | Dimensions of the housing | 61 |
| 4.1 | Comparison between the dynamic and the static method | 70 |
| 5.1 | Example of values used for the calculation of the torque corresponding to one of the current vectors | 77 |
| 5.2 | Example of values used for the calculation of $\vec{\psi}$ for one of the current vectors | 81 |
| 5.3 | Measured resistance using the PEC | 84 |
| 5.4 | Measured resistance, 4 wire method | 84 |

| | | |
|------|---|-----|
| 5.5 | Values used for the calculation of the rotor inertia | 87 |
| 5.6 | Values used for the calculation of T_{fric} | 90 |
| 5.7 | Friction as extrapolation of torque vs current toward zero | 92 |
| 5.8 | Parameters of the harmonic fitting | 100 |
| 5.9 | Values for the cogging torque | 104 |
| | | |
| 6.1 | Nominal current vector | 114 |
| 6.2 | Induced and required dc-link voltage | 116 |
| 6.3 | f_{el} and speed for different $ \vec{\psi} $ | 117 |
| 6.4 | Nominal values for the Prototype | 123 |
| 6.5 | Values uses for the loss calculation | 124 |
| 6.6 | Resistance, inductances and flux linkage of the EM | 125 |
| 6.7 | Gear ratios of the sequential gearbox | 126 |
| 6.8 | <i>iPMSM</i> -wheel transmission data | 126 |
| | | |
| B.1 | Nominal and peak current, and flux at i_0 | 145 |
| B.2 | flux linkage in x | 145 |
| B.3 | Flux linkage in y | 146 |
| B.4 | Current i_{sx} [A] | 146 |
| B.5 | Current i_{sy} [A] | 146 |
| B.6 | Electric acceleration df/dt [Hz/s] | 147 |
| B.7 | Mechanic torque T [Nm], with $J = J_{rot} + J_{5kg} = (8.8 + 28.9)$ [gm ²] | 147 |
| B.8 | x-component of the flux linkage vector ψ_{sx} [mV · s] | 147 |
| B.9 | y-component flux linkage vector ψ_{sy} [mV · s] | 147 |
| B.10 | Field weakening Look up table: i_{sx} [A] for $ \psi $ [mV s] and T [Nm] | 148 |
| B.11 | Field weakening Look up table: i_{sy} [A] for $ \psi $ [mV s] and T [Nm] | 149 |

4.1 Bibliography

- [1] Avo Reinap , Dan Hagstedt , Francisco Marquez , Yury Loayza , Mats Alakula. Development of a radial flux machine design environment. In *Electrical Machines, 2008. ICEM 2008. 18th International Conference on*, pages 1–4, Sept 2008, Villamoura, Portugal.
- [2] Yury Loayza , Avo Reinap and Mats Alaküla. Performance and efficiency evaluation of fpga controlled ipmsm under dynamic loading. In *8th IEEE Symposium on Diagnostics for Electrical Machines, Power Electronics Drives*, pages 550–555, Sept 2011.
- [3] Sebastian Hall and Yury Loayza. An evaluation of two direct current control methods implemented with labview on a fpga. In *2013 International Conference on Electrical Machines and Systems (ICEMS)*, pages 1455–1460, Oct 2013.
- [4] Måns Andersson , Aleksandar Stojkovic. *Dynamic Breaking - FPGA Implementation of DCC*. M.sc., Lund University - IEA, 2012.
- [5] Mats Alaküla, Per Karlsson. *Power Electronics*. book: Lund University-IEA, 2012.
- [6] Sebastian Hall, Yury Loayza, Avo Reinap, and Mats Alaküla. Consistency analysis of torque measurements performed on a pmsm using dynamic testing. In *2014 International Conference on Electrical Machines (ICEM)*, pages 1529–1535, Sept 2014.
- [7] Zhe Huang , F. J. Márquez-Fernández , Yury Loayza , Avo Reinap and Mats Alaküla. Dynamic thermal modeling and application of electrical machine in hybrid drives. In *2014 International Conference on Electrical Machines (ICEM)*, pages 2158–2164, Sept 2014.
- [8] Statistics Explained. Consumption of energy. http://ec.europa.eu/eurostat/statistics-explained/index.php/Consumption_of_energy.
- [9] U.S. Energy Information Administration. Use of energy in the U.S. http://ec.europa.eu/eurostat/statistics-explained/index.php/Consumption_of_energy.
- [10] Francisco J. Márquez-Fernández. *Electric traction machine design for an E-RWD unit*. Doctoral thesis, Lund University - IEA, 2014.

- [11] F. Márquez-Fernández, A. Reinap, and M. Alaküla. Design, optimization and construction of an electric motor for an electric rear wheel drive unit application for a hybrid passenger car. In *The XIX International Conference on Electrical Machines - ICEM 2010*, pages 1–6, Sept 2010.
- [12] Rasmus Andersson. *Electric Traction Machine Design for Heavy Hybrid Vehicles, TEIE-1074*. Licenciate thesis, Lund University: Division of IEA.
- [13] R. Andersson, A. Reinap, and M. Alaküla. Design and evaluation of electrical machine for parallel hybrid drive for heavy vehicles. In *2012 XXth International Conference on Electrical Machines*, pages 2622–2628, Sept 2012.
- [14] Karin Jonasson. *Control of Hybrid Electric Vehicles with Diesel Engines, TEIE-1046*. Doctoral thesis, 2005, Lund University: Div. IEA. iea.lth.se/publications/pubphd.html.
- [15] Finnis Leen , Orlando Sanchez. *Pre-study of an electrically synchronized sequential manual transmission*. M.sc., Department of Applied Mechanics, Chalmers University of Technology, Gothenburg, 2006.
- [16] Fredrik Boberg , Axel Gustafson. *Cost Efficient Hybrid Car - SAAB Automobile*. M.sc., Lund University - IEA, 2007.
- [17] Per Bandrup , Joakim Larsson. *Electrically Synchronised Gear-Shifting*. M.sc., Lund University: Div. IEA, 2006.
- [18] Per Byrhult , Axel Bergman. Automated shifting of a manual sequential transmission in a hybrid vehicle. M.sc., Lund University - IEA, 2009.
- [19] M. S. Rahimi Mousavi, H. Vahid Alizadeh, and B. Boulet. Estimation of synchromesh frictional torque and output torque in a clutchless automated manual transmission of a parallel hybrid electric vehicle. *IEEE Transactions on Vehicular Technology*, PP(99):1–1, 2016.
- [20] T.A. Lipo. *Introduction to AC Machine Design*. book: 4th edition, University of Wisconsin, Madison Wi.
- [21] T.J.E. Miller. *Brushless Permanent-Magnet and Reluctance Motor Drives*. book: , Oxford : Clarendon, 1989, ISBN 0-19-859369-4, 1989.
- [22] A. Vagati, G. Pellegrino, and P. Guglielmi. Comparison between spm and ipm motor drives for ev application. In *The XIX International Conference on Electrical Machines - ICEM 2010*, pages 1–6, Sept 2010.

- [23] Maddalena Cirani , Sture Eriksson and Jonas Thunberg. Innovative design for flux leakage reduction in ipm machines. In *2012 XXth International Conference on Electrical Machines*, pages 2671–2676, Sept 2012.
- [24] D. Hagstedt, F. Marquez, and M. Alakula. A comparison between pmsm, emsm and smsm in a bas application. In *2008 18th International Conference on Electrical Machines*, pages 1–5, Sept 2008.
- [25] W. L. Soong and T. J. E. Miller. Field-weakening performance of brushless synchronous ac motor drives. *IEE Proceedings - Electric Power Applications*, 141(6):331–340, Nov 1994.
- [26] N. Bianchi and S. Bolognani. Unified approach to the analysis and design of an ac motor drive for flux-weakening operations. In *Conference Record of 1998 IEEE Industry Applications Conference. Thirty-Third IAS Annual Meeting (Cat. No.98CH36242)*, volume 1, pages 95–102 vol.1, Oct 1998.
- [27] S. Bolognani, R. Petrella, A. Prearo, and L. Sgarbossa. On-line tracking of the mtpa trajectory in ipm motors via active power measurement. In *The XIX International Conference on Electrical Machines - ICEM 2010*, pages 1–7, Sept 2010.
- [28] Jonas Ottosson. Energy Management and Control of Electrical Drives in Hybrid Electrical Vehicles *TEIE-1054, Licentiate thesis, Lund University-IEA*, 2007.
- [29] K. Khan, S. Haghbin, M. Leksell, and O. Wallmark. Design and performance analysis of a permanent-magnet assisted synchronous reluctance machine for an integrated charger application. In *The XIX International Conference on Electrical Machines - ICEM 2010*, pages 1–6, Sept 2010.
- [30] P. Roshanfekar, S. Lundmark, T. Thiringer, and M. Alatalo. Torque ripple reduction methods for an interior permanent magnet synchronous generator. In *2014 16th European Conference on Power Electronics and Applications*, pages 1–7, Aug 2014.
- [31] Dan Hagstedt. *Comparison of Different Electrical Machines for Belt-driven Alternator and Starter, TEIE-1067*. PhD thesis, Lund University - IEA.
- [32] Cogent Power. data sheet, steel plate sura m250-35a. <https://cogent-power.com/cms-data/downloads/m250-35a.1.pdf>.
- [33] K. Stockman, S. Dereyne, D. Vanhooydonck, W. Symens, J. Lemmens, and W. Deprez. Iso efficiency contour measurement results for variable

- speed drives. In *The XIX International Conference on Electrical Machines - ICEM 2010*, pages 1–6, Sept 2010.
- [34] W. Deprez, J. Lemmens, D. Vanhooydonck, W. Symens, K. Stockman, S. Dereyne, and J. Driesen. Iso efficiency contours as a concept to characterize variable speed drive efficiency. In *The XIX International Conference on Electrical Machines - ICEM 2010*, pages 1–6, Sept 2010.
- [35] X. Liu, D. Liang, and X. Yang. Correction the pmsm dynamic test results based on rotor dynamics mathematical model. In *2014 Ninth International Conference on Ecological Vehicles and Renewable Energies (EVER)*, pages 1–6, March 2014.
- [36] A. Y. M. Abbas and J. E. Fletcher. The synthetic loading technique applied to the pm synchronous machine. *IEEE Transactions on Energy Conversion*, 26(1):83–92, March 2011.
- [37] B. Szabados, J. H. Dableh, R. D. Findlay, G. M. Obermeyer, and R. E. Draper. Measurement of the torque-speed characteristics of induction motors using an improved new digital approach. *IEEE Transactions on Energy Conversion*, 5(3):565–571, Sep 1990.
- [38] Ieee draft standard test procedure for polyphase induction motors and generators. *IEEE P112/D6, August 2016*, pages 1–114, Jan 2016.
- [39] F. Castelli. Dynamic test method for the speed-torque characteristic of dc motors. In *Quality Measurement: The Indispensable Bridge between Theory and Reality (No Measurements? No Science! Joint Conference - 1996: IEEE Instrumentation and Measurement Technology Conference and IMEKO Tec*, volume 1, pages 464–468 vol.1, 1996.
- [40] C. Y. Wu, M. C. Tasi, and S. H. Mao. Characteristics measurement of direct-drive brushless dc motors without using dynamometers. In *2009 International Conference on Electrical Machines and Systems*, pages 1–6, Nov 2009.
- [41] Bin Jin, Xin-Zhuo Chen, and Wei-Sun Leung. Development and applications of advanced intelligent instruments for dynamic torque-speed measurement. In *Industrial Electronics, Control and Instrumentation, 1994. IECON '94., 20th International Conference on*, volume 2, pages 894–899 vol.2, Sep 1994.
- [42] J. G. Cintron-Rivera, A. S. Babel, E. E. Montalvo-Ortiz, S. N. Foster, and E. G. Strangas. A simplified characterization method including satura-

- tion effects for permanent magnet machines. In *2012 XXth International Conference on Electrical Machines*, pages 837–843, Sept 2012.
- [43] Eloy Sánchez Catón. *Dynamic Braking: A new Approach for Testing Electrical Machines*. M.sc., Lund University - IEA, 2012, 2012.
- [44] Sebastian Hall. *Dynamic Testing of Permanent Magnet Machines, TEIE-1076*. Lic., Lund University: Div. IEA.
- [45] Yury Loayza Vargas. Characterization of the flow and dynamics of a synthetic jet. M.sc., 2006.
- [46] S. Haghbin, M. Sadeghi Kani, D. Vindel, O. Carlson, and S. Lundmark. A trigonometric velocity estimator using a resolver sensor in drive system applications. In *IECON 2012 - 38th Annual Conference on IEEE Industrial Electronics Society*, pages 2889–2894, Oct 2012.
- [47] H. Tanaka, H. Nishi, and K. Ohnishi. An approach to acceleration estimation using fpga. In *2008 IEEE International Symposium on Industrial Electronics*, pages 1959–1964, June 2008.
- [48] T. D. Batzel and M. Comanescu. Instantaneous voltage measurement in pwm voltage source inverters. In *2007 International Aegean Conference on Electrical Machines and Power Electronics*, pages 168–173, Sept 2007.
- [49] Arun G. Padke and James S. Thorp. *Computer Relaying for Power Systems*. book: ISBN 0-86380-074-2. 1993.
- [50] L. Glielmo, L. Iannelli, V. Vacca, and F. Vasca. Gearshift control for automated manual transmissions. *IEEE/ASME Transactions on Mechatronics*, 11(1):17–26, Feb 2006.
- [51] Zhe Huang. *Thermal Design of Electrical Machines - Investigation and Evaluation of Cooling Performances, TEIE-1070*. Licentiate thesis, 2013, Lund University: Div. IEA. iea.lth.se/publications/public.html.
- [52] Hammad Khan. *Dynamic Control of PMSM via Profibus Communication Between NI-CRio and Vacon Frequency Converter*. M.sc., Lund University: Dept. Physics + Div. IEA. www.lu.se/lup/publication/2861438, 2012.
- [53] Malin Reinholds , Steve Andreasson. *Dynamic gear shifting of an automated manual transmission*. M.sc., Lund University: Div. IEA. iea.lth.se/publications/pubmsc.html, 2013.

- [54] Johan Björnstedt , M.Ström. Power electronic voltage and frequency control for distributed generation system. M.sc., Lund University - IEA, <http://iea.lth.se/publications/pubmsc.html>, 2005.

| | | | |
|--|--|--|-------|
| Organization LUND UNIVERSITY Department of BME Division of Industrial Electrical Engineering and Automation (IEA) | | Document name DOCTORAL DISSERTATION | |
| | | Date of disputation 2017-10-20 | |
| Author(s) Yury Alcides LOAYZA VARGAS | | Sponsoring organization Vinnova, Innovatum, The Swedish Energy Agency, Lund University | |
| Title and subtitle Highly Dynamic Drives for Electric Hybrid Vehicles Electric Machine Design and Dynamic Test Method | | | |
| Abstract <p><i>Electric Hybrid Vehicles (EHVs)</i> play a crucial role in the development towards a more environmental friendly transportation. An alternative to solve some actual challenges with hybridization of vehicles is studied at the <i>Division of Industrial Electrical Engineering and Automation (IEA)</i> at Lund University in cooperation with the automotive industry. A key component of this drive train is a highly dynamic <i>Electric Machine (EM)</i> which will make possible to hybridize a conventional car at reduced costs while maintaining the performance and comfort of the vehicle.</p> <p>The first part of this thesis work describes the design and optimization process of this multipurpose <i>EM</i> and presents the final prototype.</p> <p>The second part of this thesis presents a convenient, fast and precise method for measuring the mechanical and electromagnetic properties of this <i>EM</i> and similar motors. This <i>Dynamic Test Method</i> is based on state of the art control and measurements system and makes possible to characterize an <i>EM</i> without the need of a <i>Brake Bench</i>.</p> <p>Finally the measured properties of the <i>EM</i> are analyzed and the results show that the <i>EM</i> has the required performace in speed, torque and dynamics for the intended <i>EHV</i> application.</p> <p>The results of the thesis reduce the need of heavy and expensive components for the <i>EHV</i> and for the measurements, by using very fast, dynamic and accurate tools instead.</p> | | | |
| Key words Electric Hybrid Vehicles, Electric Machine Design, Dynamic Testing, Dynamic loading, Synthetic Loading, FPGA, Torque Measurement, Field Weakening, iPMSM, FEMM, LabView | | | |
| Classification system and/or index terms (if any) | | | |
| Supplementary bibliographical information | | Language English | |
| ISSN and key title | | ISBN 978-91-88934-83-3 (print) 978-91-88934-82-6 (pdf) | |
| Recipient's notes | | Number of pages 210 | Price |
| | | Security classification | |

I, the undersigned, being the copyright owner of the abstract of the above-mentioned dissertation, hereby grant to all reference sources the permission to publish and disseminate the abstract of the above-mentioned dissertation.

Signature _____

Date 2017-08-29 _____



Yury Loayza, born in Cusco, Peru, has a degree of Master of Science in Mechanical Engineering from the Faculty of Engineering of Lund University (LTH) in Sweden. He carried out part of his undergraduate studies in Stuttgart, Germany and also in Boulder, Colorado, USA.

Yury Loayza carried out his PhD Studies at the at the Division of Industrial Electrical Engineering and Automation (IEA) at LTH, focusing on Electric Hybrid Vehicles.

